



PhD in Design, Manufacturing and Operations Engineering  
XXXV Cycle

Department of Enterprise Engineering

ADVANCED SIMULATION OF AN OPERATING ROOM:  
FROM THE VIRTUAL MODEL TO THE DIGITAL TWIN

GIOVANNA GARGIULO

A.Y. 2021/2022

Tutor: Prof. M. E. Biancolini

Tutor: Ing. M. Grigioni - Italian National Institute of Health

Coordinator: Prof. E. Pennestrì

Giovanna Gargiulo : *Advanced Simulation of an Operating Room: from the Virtual Model to the Digital Twin*, © March 14, 2023

---

## ABSTRACT

---

In this work is considered the possible use of Digital Twin (DT) in air quality management in an operating theatre to study airflow and prevent post-surgery infections. Infections are a relevant problem in hospitals and imply an extension of the time post-surgery, eventually a new surgery, and, in some cases, the complications that can lead to death. It is crucial to prevent this scenario, ensuring complete control of the air quality in the operating theatre and the critical areas of the building. In the last decades, Computational Fluid Dynamics (CFD) has given help to forestall these problems and make safer hospital environments. However, CFD is computationally expensive and can give the solutions relative to a unique set of parameters defined in B.Cs, given the problem.

Digital Twin offers a further step. It allows processing of a large number of fully CFD simulated scenarios to train a Reduced Order Model (ROM). Once validated, the ROM can be interrogated to retrieve the full field CFD solution for a new set of parameters in the investigated range of the design space and, eventually, enriched by new full computed CFD solutions for points outside it. CFD solutions are acquired using HPC (High Performance Computing) resources, on the other hand, the constructed ROM can produce the results in a matter of minutes, which can then be exported in a DT which can be used within a matter of seconds. The ROM is obtained from the CFD solutions using a Singular Values Decomposition (SVD), and at the end, the construction of DT uses the ROM that can also be exported as Functional Mock-up (FMU).

This study in origin was composed of a CFD part from which to build the ROM and the DT and an experimental part with the possibility of comparing the CFD and DT results with the experimental data. Currently, the experimental part is a work in progress. The thesis aims to highlight the advantage of DT that it could obtain in real-time the variables of interest associated with any change in the room conditions. Concerning that, the capacity to realize and improve the Digital Twins is considered important not only for design and maintenance but also for reactive and, in the future prescriptive environmental management, expanding its use in other sectors.

*There must be no barriers to freedom of inquiry ... There is no place for  
dogma in science. [...]*

*J. Robert Oppenheimer*

*Omnia, Lucili, aliena sunt, tempus tantum nostrum est; [...].*

*Epistula ad Lucilium I (Sen. Ep. Luc. I)*

---

## ACKNOWLEDGEMENTS

---

This work has been carried out with the support of the National Center for Innovative Technologies in Public Health, Italian National Institute of Health (ISS). Namely, I express my heartfelt gratitude to Ing. M. Grigioni. and Dr. G. D’Avenio.

I thank prof. A. Marconi de Souza da Costa for his help with the making geometry and meshing issues.

I ought to thank Ansys’s technical support for the technical recommendations.

I express my heartfelt gratitude to researchers S. Porziani for his help in HPC and C. Groth for his technical support during this work.

I thank Ing. A. Martinez for his availability and his technical suggestions.

I thank Ing. A. Lopez for his precious help.

Last but not least, I express my gratitude to those who have enabled the final phase of this work to be completed.

In closing, I thank my advisor Professor M. E. Biancolini for his guidance, support, and patience.

I would like to thank my family, my mother, my sister often in my thoughts, and my aunt, who is my supporter. A thought to my father always present in every moment.

---

## CONTENTS

---

1	Introduction	1
1.1	Nosocomial infections causes . . . . .	1
1.2	The Digital Tiwn . . . . .	2
1.3	State of the Art . . . . .	3
1.3.1	Air quality issues . . . . .	3
1.3.2	Numerical Studies . . . . .	5
1.3.3	Experimental Studies . . . . .	8
1.4	Thesis scope . . . . .	9
1.5	Methodological approach . . . . .	10
2	Ventilation and Filtration Systems	13
2.1	Ventilation Systems . . . . .	13
2.1.1	Ventilation Systems in operating theatres . . . .	14
2.2	Standards references . . . . .	19
2.2.1	UNI EN ISO 14644 . . . . .	20
2.2.2	UNI EN ISO 11425:11: Italian standards . . . . .	20
3	Theoretical background	22
3.1	Theoretical background . . . . .	22
3.1.1	CFD governing equations . . . . .	22
3.1.2	Time Discretization: Pseudo Transient Method .	24
3.1.3	Morphing concept . . . . .	25
3.1.4	Construction of the ROM . . . . .	26
3.2	Computational model and mesh . . . . .	29
3.2.1	Boundary conditions . . . . .	29
3.2.2	A method for calculating the DoE . . . . .	30
4	Case studies: methodology	31
4.1	Case studies . . . . .	31
4.1.1	Operating Theatre geometry: case study . . . .	31
4.2	Main Steps . . . . .	31
4.3	Settings . . . . .	34
4.4	First step: case#1 . . . . .	35
4.5	Second step: case 2# . . . . .	36
4.6	Simulation times and FMU and ROM models in Twin Builder . . . . .	37
4.7	Second step: case 3# . . . . .	37
4.8	Third step: case 4# . . . . .	42
4.9	Third step: case 5# . . . . .	45
5	Experimental Studies	50
5.1	The working fluids: features . . . . .	50
5.2	Test Equipment . . . . .	54

6	Results	59
6.1	Numerical Results	59
6.2	CFD Results	59
6.2.1	CFD: Case 6a# and 6b#	59
6.3	ROM Results	62
6.3.1	ROM: case 6a# and case 6b#	63
6.4	Case study: case 6c# from CFD to DT	64
6.4.1	Case Study: case 6c# ROM	69
6.5	ROM VS ROM	73
6.6	Results:case 6c# CFD VS ROM result	84
6.7	Discussion	88
6.8	Preliminary studies: a complete simulation and further considerations	90
7	Conclusions	96
7.1	Intentions and accomplishments	96
7.2	Open issues	97
	Appendix A ACH	99
	Appendix B H <sub>2</sub> O	101
	Appendix C CO <sub>2</sub>	105
	Bibliography	106

---

## ACRONYMS

---

<b>ACH</b>	Air Changes per Hour
<b>AoA</b>	Air of Age
<b>BCs</b>	Boundary Conditions
<b>BCP</b>	Bacteria-carrying particles
<b>CCD</b>	Central Composite Designs
<b>CFD</b>	Computational Fluid Dynamics
<b>CFU</b>	Colony Forming Unit
<b>DoE</b>	Design of Experiment
<b>DLAF</b>	Differential Vertical Airflow
<b>DT</b>	Digital Twins
<b>EPA</b>	Efficiency Particulate Air
<b>Eu</b>	Euler number
<b>FMU</b>	Functional Mock-up Interface
<b>GARS</b>	Genetic Aggregation Response Surface
<b>HEPA</b>	High Efficiency Particulate Air
<b>HLAF</b>	Horizontal Laminar Airflow
<b>HVAC</b>	Heating, Ventilation and Air Conditioning
<b>IIoT</b>	IIoT (Industrial Internet of Thingh)
<b>LAD</b>	Laminar Airflow Diffuser
<b>LAF</b>	(ultraclean) Laminar Airflow
<b>LOO</b>	Leave One Out
<b>MAROME</b>	Max Absolute ROM Error
<b>MAE</b>	Max Absolute Error
<b>MET</b>	Metabolic rate
<b>MLAF</b>	Mobile Laminar Airflow

<b>MOT</b>	Mixed Airflow
<b>MPPS</b>	maximum penetrating particle size
<b>MV</b>	Mixing Ventilation
<b>PBS</b>	Pressure-based Solved
<b>PIV</b>	Particle image velocimetry
<b>PMV</b>	Predicted Mean Vote
<b>PTS</b>	Pseudo-time Step
<b>RANS</b>	Reynolds Averaged Navier-Stokes
<b>RBFs</b>	Radial Basis Function
<b>Re</b>	Reynolds number
<b>RH</b>	Relative Humidity
<b>ROM</b>	Reduced Order Model
<b>ROMRE</b>	ROM Relative Error
<b>RRRMSE</b>	Reduction Relative RMS Error
<b>RRE</b>	Reduction Relative Error
<b>SSI</b>	Surgical Site Infections
<b>SVD</b>	Singular Value Decomposition
<b>TAF</b>	Temperature controlled Airflow
<b>TB</b>	Twin Builder
<b>TFDA</b>	Turbulent Flow Air Distribution
<b>TOT</b>	Turbulent Airflow
<b>UDF</b>	Unidirectional air Flow
<b>ULPA</b>	Ultra Low Penetration Air
<b>UOT</b>	Unidirectional Airflow
<b>URANS</b>	Unsteady Reynolds Averaged Navier Stokes Equations
<b>VCCC</b>	Ventilation and air-Conditioning system for Contamination Control
<b>VLAF</b>	Vertical Laminar Airflow

**SYMBOLS**

<b>a</b>	Constant Value in cubic EOS
<b>b</b>	Constant Value in cubic EOS
<b>H<sub>2</sub>O</b>	water
<b>L<sub>1</sub></b>	length scale1
<b>L<sub>2</sub></b>	length scale2
<b>m</b>	mass flow rate
<b>N<sub>2</sub></b>	nitrogen
<b>Q</b>	volumetric flow rate
<b>v</b>	velocity
<b>V</b>	Volume

**GREEK SYMBOLS**

<b>ρ</b>	Density
<b>μ</b>	cinematic viscosity
<b>ν</b>	dynamic viscosity
<b>τ</b>	pseudo time step

**SUBSCRIPTS**

<b>c</b>	Critical Value
<b>r</b>	Reduced Value

---

LIST OF FIGURES

---

Figure 1.3.1	Surgical site contamination . . . . .	4
Figure 1.3.2	Operating theatre and impact on the opening door and their effect on SSI. Reprinted from Birgand et al. [22] . . . . .	5
Figure 1.3.3	Sketch of a typical air curtain system. Reprinted from Zhai et al. [94] . . . . .	6
Figure 1.3.4	Description of the several ventilation systems: (a) VLAf, (b) HLAf, (c) DVAF, (d) TAF. Reprinted from Zhai et al. [53] . . . . .	7
Figure 1.3.5	The figure taken from [97] shows a model that represents the heat exchange in a room to which is added the contribution given by a radiator. .	8
Figure 2.1.1	Figure left is a LAF system, and figure right is a TMA system. Reprinted from Alsved et al. [7].	17
Figure 2.1.2	In figure left, a T <sub>c</sub> AF system reprinted from Alsved[7], and in figure right MLAF system reprinted from Sadrizadeh et al. [78]. . . . .	17
Figure 2.1.3	In the figure left, it is indicated (a) UDF ventilation and (b) Mixing ventilation, Reprinted from Sadeghian[75]. In figure right (a) schematic air-flow from a LAF and (b) vertically installed LAF, Reprinted from Sadrizadeh et al. [77]. . .	18
Figure 2.1.4	EPA, HEPA, ULPA filters, UNI EN 1822-1 [33]. Reprinted from Di Santis [31] . . . . .	19
Figure 3.1.1	Snapshot of temperature range values . . . . .	26
Figure 3.2.1	On the left, the trend between the minimum and maximum of the different input parameters. On the right is the trend of one of the input parameters with respect to the number of samples. . . . .	30
Figure 4.1.1	Sketch of the geometry of the operating theatre, Romano et al. [73] . . . . .	32
Figure 4.4.1	The figure on the left shows the geometry of a room with an HVAC on which the inlet and outlet of the airflow are indicated. On the right, the same geometry is represented with a mesh with predominantly hexahedral quadrangular elements case #1 . . . . .	35

Figure 4.4.2	The figure shows the velocity field on a section of the chamber and HVAC with power lines. The maximum velocity is highlighted in proximity to the exit. HVAC and ceiling case 1#	36
Figure 4.5.1	On the left is the geometry and mesh of the operating room. On the right is represented a transient simulation with particle insertion: inert with two different diameters. . . . .	36
Figure 4.6.1	Twin Builder - FMU model and ROM: results obtained by inserting the ROM or FMU model inside the TB software. The insertion of the input parameter values was highlighted with the circumference and the ellipse. . . . .	37
Figure 4.7.1	Operating room geometry discretization: mesh made up of 300k poly-hexa elements. . . . .	39
Figure 4.7.2	Left field of velocity. On the right is the velocity vector field. . . . .	39
Figure 4.7.3	On the left, temperature field with a superimposed velocity vector field. On the right, the temperature trend in 30 points is extracted along the line on the diagonal section of the chamber. . . . .	40
Figure 4.7.4	Temperature field and details according to the diagonal plane and according to an xz plane. .	40
Figure 4.7.5	Trend of the pressure field on the diagonal section of the operating room. . . . .	41
Figure 4.8.1	Operating room geometry discretization: mesh made up of more than 300k poly-hexa elements.	43
Figure 4.8.2	Left field of velocity. On the right is the velocity vector field. . . . .	43
Figure 4.8.3	On the left, temperature field with a superimposed velocity vector field. On the right, the temperature trend in 30 points is extracted along the line on the diagonal section of the chamber. . . . .	44
Figure 4.8.4	Temperature field and details according to the diagonal plane and according to an xz plane. .	44
Figure 4.8.5	Trend of the pressure field on the diagonal section of the operating room. . . . .	44
Figure 4.9.1	Operating room geometry discretization: mesh made up of about three millions poly-hexa elements. . . . .	46
Figure 4.9.2	Left field of velocity. On the right is the velocity vector field. . . . .	46

Figure 4.9.3	On the left, temperature field with a superimposed velocity vector field. On the right, the temperature trend in 30 points is extracted along the line on the diagonal section of the chamber. . . . .	47
Figure 4.9.4	Temperature field and details according to the diagonal plane and according to an xz plane. .	47
Figure 4.9.5	Trend of the pressure field on the diagonal section of the operating room. . . . .	47
Figure 4.9.6	Comparison between the temperatures obtained in case 3# and case 4#. Diagonal section of the chamber on the straight line (a) with coordinates: P1(0.573879, 1.62396, 6.42445) and P2(6.41105, 1.62396, 0.588). . . . .	48
Figure 4.9.7	Comparison between the temperatures obtained in case 3#, case 4# and case 5#. Diagonal section of the chamber on the straight line (a) with coordinates: P1(0.573879, 1.62396, 6.42445) and P2(6.41105, 1.62396, 0.588). . . . .	49
Figure 4.9.8	On the left, the RH field shows the trend for a maximum value of 50%. On the right, the trend of the temperature field in C°. . . . .	49
Figure 5.1.1	The Z compressibility factors in the gas phase are shown on the left and right. . . . .	52
Figure 5.1.2	The pressure field of air and water are shown on the left and right. . . . .	53
Figure 5.1.3	The velocity field of air and water are shown on the left and right. . . . .	53
Figure 5.1.4	The pressure field of air and water are shown on the left and right. . . . .	54
Figure 5.1.5	The velocity field of air and water are shown on the left and right. . . . .	54
Figure 5.1.6	The pressure field of air and water are shown on the left and right. . . . .	55
Figure 5.1.7	The velocity field of air and water are shown on the left and right. . . . .	55
Figure 5.2.1	The figure shows the box model . . . . .	56
Figure 5.2.2	The figure shows the scale model of the operating theatre . . . . .	56
Figure 5.2.3	The figure shows the whole scale model . . . .	56
Figure 5.2.4	In the figure is shown the mock-up made of the plexiglass material of the operating theatre. A zoom on the calming baffle is realized . . . . .	57

Figure 5.2.5	The figure shows to the left the scale model and three basil used to fill up the tank or to empty it, and to the right, the tank where is highlighted the maximum level of water call as "overfull". . . . .	57
Figure 5.2.6	In the figure to the left is shown the pressure gauge; to the right at the top is shown the electromagnetic flowmeter, and at the bottom, the flowmeter that will be linked to the scale model.	57
Figure 5.2.7	In the figure is shown the laser. . . . .	58
Figure 6.2.1	Geometry of the operating room. Reprinted from Romano et al. [73]. . . . .	60
Figure 6.2.2	Detail of the mesh of the operating room and the cylinder. . . . .	61
Figure 6.2.3	The mesh of the operating room and the human dummy inside according to the YZ plane is shown on the left and right. . . . .	62
Figure 6.2.4	Detail of the mesh of the operating room and the human dummy. . . . .	63
Figure 6.3.1	The values of the temperature field relating to two different values of the parameter of temperature are shown on the left and right: case 6a# . . . . .	64
Figure 6.3.2	The values of the temperature field relating to two different values of the parameter of position are shown on the left and right: case 6b# . . . . .	64
Figure 6.4.1	Geometry of the operating room. . . . .	65
Figure 6.4.2	Diagram of the workflow used. . . . .	66
Figure 6.4.3	Case 6c#: on the left, we observe the mesh of the operating room and the human dummy present inside it according to the YZ plane, and on the right, the mesh refinement is shown. . . . .	68
Figure 6.4.4	Case 6c#: detail of the mesh of the operating room and the human dummy. . . . .	68
Figure 6.4.5	On the top is the trend between the minimum and maximum of the different input parameters. On the bottom is the trend of one of the input parameters with respect to the number of samples. . . . .	69
Figure 6.4.6	The values of the temperature field relating to two different snapshots of the field are shown on the top and bottom. . . . .	71
Figure 6.4.7	Top and bottom, two different ROMs built with a different number of snapshots are shown. . . . .	72

Figure 6.4.8	Difference between two ROMs built with a different number of snapshots. . . . .	72
Figure 6.4.9	The two images show the temperature field obtained from the ROM as a geometric parameter varies, which determines a different position of the dummy. . . . .	73
Figure 6.5.1	Parameter values used to compare CFD and ROM results . . . . .	74
Figure 6.5.2	CFD simulations: on the top figure the result obtained through CFD of the temperature field; on the bottom the result obtained through CFD of the RH field; . . . . .	75
Figure 6.5.3	CFD-ROM comparison: on the top the result obtained through CFD of the temperature field; the bottom figure the ROM with 15 snapshots, with the same values of the parameters used, figure 6.5.1 . . . . .	75
Figure 6.5.4	CFD-ROM comparison: on the top the result obtained through CFD of the RH field; the bottom figure the ROM with 15 snapshots, with the same values of the parameters used, figure 6.5.1 . . . . .	76
Figure 6.5.5	CFD-ROM comparison: the top figure shows the result obtained through CFD of the temperature field; the bottom figure shows the ROM for 25 snapshots, with the same values of the parameters shown in figure 6.5.1 . . . . .	76
Figure 6.5.6	Temperature reduction error between two different snapshots for two ROMs constructed with 15 snapshots (top) and 25 snapshots (bottom)	78
Figure 6.5.7	Temperature ROM error between two different snapshots for two ROMs constructed with 15 snapshots (top) and 25 snapshots (bottom) . .	78
Figure 6.5.8	Temperature comparison between two different snapshots for two ROMs constructed with 15 snapshots and 25 snapshots . . . . .	79
Figure 6.5.9	Temperature reduction error between two different snapshots for two ROMs constructed with 32 snapshots (top) and 45 snapshots (bottom)	79
Figure 6.5.10	Temperature reduction error between two different snapshots for two ROMs constructed with 32 snapshots (top) and 54 snapshots (bottom)	80

Figure 6.5.11	Temperature reduction error between two different snapshots for two ROMs constructed with 32 snapshots (top) and 45 snapshots (bottom)	80
Figure 6.5.12	Temperature ROM error between two different snapshots for two ROMs constructed with 32 snapshots (top) and 54 snapshots (bottom)	81
Figure 6.5.13	Temperature comparison between two different snapshots for two ROMs constructed with 32 snapshots and 45 snapshots	82
Figure 6.5.14	The two images show on the top the CFD temperature and on the bottom the ROM temperature with 32 snapshots	82
Figure 6.5.15	The two images show on the top the CFD relative humidity and the bottom the ROM relative humidity with 32 snapshots	83
Figure 6.5.16	The two images show on the top the CFD temperature and on the bottom the ROM temperature with 45 snapshots	83
Figure 6.5.17	The two images show on the top the CFD temperature and on the bottom the ROM temperature with 54 snapshots	84
Figure 6.6.1	Different positions of the human dummy for the temperature field obtained from ROM: 0.75m (left) and 0.9m (right).	85
Figure 6.6.2	Different velocity of the human dummy for the temperature field obtained from ROM: 0.1m/s (left) and 0.5m/s (right).	85
Figure 6.6.3	Operating theatre DT: in the left part, there are the probes of the inlet values; in the right part, there is the ROM and the behavior of average temperature.	86
Figure 6.6.4	Map of features of the singular part: CFD, model, ROM	86
Figure 6.6.5	The temperature CFD field is shown on the top and the related RH field on the bottom.	87
Figure 6.6.6	The ROM related to the temperature field is shown on the top, and the ROM related to the RH field is shown on the bottom.	87
Figure 6.7.1	Model in Plexiglas of the operating theatre, scale 1:10, with two elements of medical staff.	89
Figure 6.8.1	The geometries of the operating theatre with different surgical lamps: in the left figure (a), the radius of the lamp is smaller than the one in the right figure (b).	91

Figure 6.8.2	The temperature field for two different positions and dimensions of surgical lamp: in the left figure (a), the diameter of the surgical lamp is smaller than the one in the right figure (b). . . . .	91
Figure 6.8.3	The temperature field for two different positions and dimensions of surgical lamp (in evidence): in the left figure (a), the diameter of the surgical lamp is smaller than the one in the right figure (b). . . . .	91
Figure 6.8.4	The velocity field for two different positions and dimensions of surgical lamps: in the left figure (a), the diameter of the lamp is smaller than the one in the right figure (b). . . . .	92
Figure 6.8.5	The velocity field for two different positions and dimensions of surgical lamps (in evidence): in the left figure (a), the diameter of the lamp is smaller than the one in the right figure (b). . . . .	92
Figure 6.8.6	The vector field of velocity for two different positions and dimensions of surgical lamps (in evidence): in the left figure (a), the diameter of the lamp is smaller than the one in the right figure (b). . . . .	92
Figure 6.8.7	The temperature slice and vector field of velocity for two different positions and dimensions of surgical lamps (in evidence): in the left figure (a), the diameter of the lamp is smaller than the one in the right figure (b). . . . .	93
Figure 6.8.8	The chart of temperature extract on the red line ( $y=1.35\text{m}$ ) for two different positions and dimensions of surgical lamps (in evidence): in the left figure (a), the diameter of the lamp is smaller than the one in the right figure (b). . . . .	93
Figure 6.8.9	The temperature slice and vector field of velocity, and four lines to extract the velocity, for two different positions and dimensions of surgical lamps (in evidence): in the left figure (a), the diameter of the lamp is smaller than the one in the right figure (b). . . . .	94
Figure 6.8.10	The chart of velocity extract on the red line ( $y=1.35\text{m}$ ) for two different positions and dimensions of surgical lamps (in evidence): in the left figure (a), the diameter of the lamp is smaller than the one in the right figure (b). . . . .	94

Figure 6.8.11	The chart of velocity extract on the three lines ( $z=-1.5$ yellow line, $z=-3.5$ green line, and $z=-4.5$ pink line) for two different positions and dimensions of surgical lamps (in evidence): in the left figure (a), the diameter of the lamp is smaller than the one in the right figure (b). . .	95
Figure 6.8.12	The different geometry of the ventilation system: in the left figure, the system is similar to a LAF or an air curtain; in the right figure, the system is similar to a UDF. . . . .	95
Figure 6.8.13	The different geometry of the ventilation system obtained by means RBF Morph. . . . .	95

---

LIST OF TABLES

---

Table 1	Environmental parameters in the operating theatre . . . . .	5
Table 2	Parameters in the operating theaters UNI 11425 [34]. Reprinted from Di Santis [31] . . . . .	14
Table 3	Operating theatre and impact on the opening door and their effect on SSI. Reprinted Sadrizadeh et al. [77]. <sup>a</sup> Calculated based on values given in the article, either information on number of door openings/surgeries and the duration of surgery or openings/minute. <sup>b</sup> The articles give information on the average ACH. <sup>c</sup> Non-laminar. . . . .	15
Table 4	Characteristics of operating theatre ventilation systems. Reprinted from Sadrizadeh et al. [77]	16
Table 5	Table shows the number of cases and the related step. . . . .	33
Table 6	Table shows the main values of setup for the cases: case 1#, case 2 #, case 3 #, case 4 #, case 5 #.	34
Table 7	Range of variation of the input parameters. . .	34
Table 8	Dimensions of the case1# chamber. . . . .	35
Table 9	Initial and boundary conditions in the room and for the HVAC case 1#. . . . .	35
Table 10	Dimensions of the case 2# chamber. . . . .	37
Table 11	Initial and boundary conditions for the chamber and the HVAC case 2#. . . . .	37
Table 12	Geometric dimensions of the case 3# operating room. . . . .	38
Table 13	Initial and boundary conditions for the chamber and the HVAC case 3#. . . . .	39
Table 14	Geometric dimensions of the case 4# operating room. . . . .	43
Table 15	Initial and boundary conditions for the chamber and the HVAC case 4#. . . . .	43
Table 16	Geometric dimensions of the case5# operating room. . . . .	45
Table 17	Initial and boundary conditions for the chamber and the HVAC case 5#. . . . .	46
Table 18	Comparison between water, air, and glycerine	51
Table 19	Comparison between water and air (N <sub>2</sub> ) . . . .	51

Table 20	Critical values of N <sub>2</sub> and water . . . . .	51
Table 21	Number of air changes per hour . . . . .	52
Table 22	Pressure, velocity, pseudo time step set-up . .	53
Table 23	Pressure, velocity, pseudo time step set-up . .	54
Table 24	Pressure, velocity, pseudo time step set-up . .	55
Table 25	Geometric dimensions of the case operating room: case 6a#. . . . .	60
Table 26	Initial conditions for the room and the case HVAC case 6a#. . . . .	60
Table 27	Initial conditions for the room and for the case HVAC case 6b#. . . . .	62
Table 28	Range of variation of the case input parameters case 6a#. . . . .	63
Table 29	Range of variation of the input parameters: case 6b#. . . . .	64
Table 30	Geometric dimensions of the operating room: case6b# and case6c#. . . . .	65
Table 31	Initial conditions for the room and the HVAC.	69
Table 32	Range of variation of the input parameters. . .	70
Table 33	In the table is shown the percent of the number of snapshots and the error between the CFD and ROM in cases #6b and #6c. . . . .	88
Table 34	In the table is shown the percent of several snapshots, the RRE, ROMRE, Reduction, ROM, and Interpolation errors, and the ROM error-average absolute error in cases #6b and #6c. . .	88
Table 35	Initial conditions for the room and the HVAC.	90
Table 36	Range of variation of the input parameters: simulation (a) and simulation (b). . . . .	90
Table 37	The table shows the relevant difference between simulations (a) and (b). . . . .	91
Table 38	The table shows the relevant difference between the simulations (a) and (b). . . . .	91

---

## INTRODUCTION

---

That there is a high possibility of developing infections in the hospital is well known. Infections that could be contracted in a hospital are of two main kinds:

- nosocomial infection
- Surgical Site Infections (**SSI**)

### 1.1 NOSOCOMIAL INFECTIONS CAUSES

Nosocomial infections are infections caused by the hospital environment, e.g., hospital construction, HVAC systems, medical procedures, see Gonzalez et al. [42]. The other causes could be that the infection was acquired by a patient during a hospital stay or by hospital personnel.

Berrios et al. [19], e.g., identify the main causes of the SSIs in airborne bioparticles. The majority of SSIs arise during a surgical operation, and their development depends upon the surgical technique, the type of operation, the duration, the behavior of the surgical team, as well as the patient's state of health (immune system) and antibiotic prophylaxis. Furthermore, possible factors contributing to SSI are the operating theatre cleanliness (the presence of contaminants in the operating room), the HVAC system (the number of air changes per hour, the pattern of air movement, the amount of time that air stays in the operating room, etc.), Farad et al. [38], and the sectioning of the surgical block. In this case, the SSIs can be classified into three categories, Di Santis [31]:

- superficial
- deep incisional
- organ (depending on the operations performed)

In effect, the SSIs are the main causes of complications after surgical operations and constitute up to 19.6% of all healthcare-associated infections in Europe, according to Sanchez et al. [79], and Pasquarella

et al. [64]. In the case of SSIs, the patient has a longer hospital stay, additional surgical procedures that imply additional costs, and an increase in mortality. Biscione et al. [23] define the SSI rate as one of the indicators used internationally to quantify the quality of medical services.

A further source of infections in the operating theatre is the skin scales and particles released by the human body during breathing, transpiration, and sweating. Another source of infections is the particles released from standard personnel clothing.

In this scenario, help is given from the new technologies that offer a different vision by implementing the physical reality with a digital one.

## 1.2 THE DIGITAL TIWN

Using a DT, the virtualization of a physical asset can be made and it can give in realtime prediction, optimization, monitoring, controlling, and improved decision-making by processing the data and running simulations in a short time. Rasheed et al., [72], refer to it as a computational: megamodel, device shadow, mirrored system, avatar, or synchronized virtual prototype. The authors also speak of digital siblings (copies of physical assets), which can be used to test hypothetical scenarios. They also define the eight properties of a digital twin and some examples of application areas. The eight properties of the DT are:

- Real-time remote monitoring and control
- Greater efficiency and safety
- Predictive maintenance and scheduling
- Scenario and risk assessment
- Better intra- and inter-team synergy and collaborations
- More efficient and informed decision support system
- Personalization of products and services
- Better documentation and communication

A list of the main areas of interest is provided:

- Meteorology
- Manufacturing and process technology
- Education

- Cities, transportation, and energy sector
- Health

From above, "manufacturing and process technology" is a relevant sector where the DTs are employed, as pointed to VanDerHorn et al. [87], and Tao et al. [82]. A particular area of interest for us is the "health sector". There are different uses of DT in the "health" sector, e.g., Peng et al. [66] propose a method based on the DT for innovative techniques and management. The DT software system permits real-time visual management and the use of artificial intelligent diagnosis modules. This study aims to produce the DT of an operating theatre by means of the **CFD** support and the **ROM** building.

### 1.3 STATE OF THE ART

In this section the issues related to air quality in the subsection 1.3.1, the numerical and experimental studies in the section 1.3.2, and 1.3.3.

#### 1.3.1 *Air quality issues*

The air quality in the operating theatre had already been tackled in the 1960s, highlighting a link with the development of post-surgery infections, see figure 1.3.1, and the probability of contracting bacterial infections in operating sites (cf. Agodi et al. [5] , Lydon et al. [54], Whyte et al. [91], Lidwell et al. [49], Agodi et al. [5], Pasquarella et al. [61], Pasquarella et al. [63], Pasquarella et al. [62]). Consequently, for the purpose of determining the CFU present in the operating environment, a value used to define microbial contamination of the air, with specifications provided by UNIENISO [32], plates were used for bacterial sedimentation positioned at various points and heights within the operating room.

Chapter 2 introduces the different ventilation systems in the operating theater that were therefore studied: **LAF**, **MOT**, **UOT**, **TOT**, and filtering systems that use the filters called **HEPA** whose requirements are given in UNIEN1822 [33]. The capability of filtration is essential to avoid the contamination of surgical sites. The HEPA filters have an efficiency equal to at least 99.95% of the particles entering the filter, having a size equal to the **MPPS**, according to the international standard EN 1822 [33], and an even greater efficiency value is obtained for particles of different sizes.

Thanks to the possibility of being able to quickly and easily carry out multiple tests, the use of the CFD simulations, in recent decades,

was useful to understand the impact of the different air injection methods in operating theatres, published in the studies by Di Santis[31], Balocco et al. [16], and Al-Waked [6].

It is possible to analyze the different air circulation scenarios in operating theatre in relation to both the type of ventilation systems and the arrangement of filters and filming, the presence of medical personnel, machinery, and scialytic lamps present in the operating room, and considering the conditions of injection of air flows according to the UNI11425 [34] standards. According to these standards the operating conditions are in the range  $20 \leq T[^\circ\text{C}] \leq 24^\circ\text{C}$ ,  $40\% \leq \text{humidity } \% \leq 60\%$  with a maximum pressure variation of 15 Pa, see table 1. In addition, to prevent infections, the quantity of airborne particulate that might carry bacteria and potentially infectious particles coming from the skin and mucous membranes of the patient, and also epithelial residues from the medical staff.

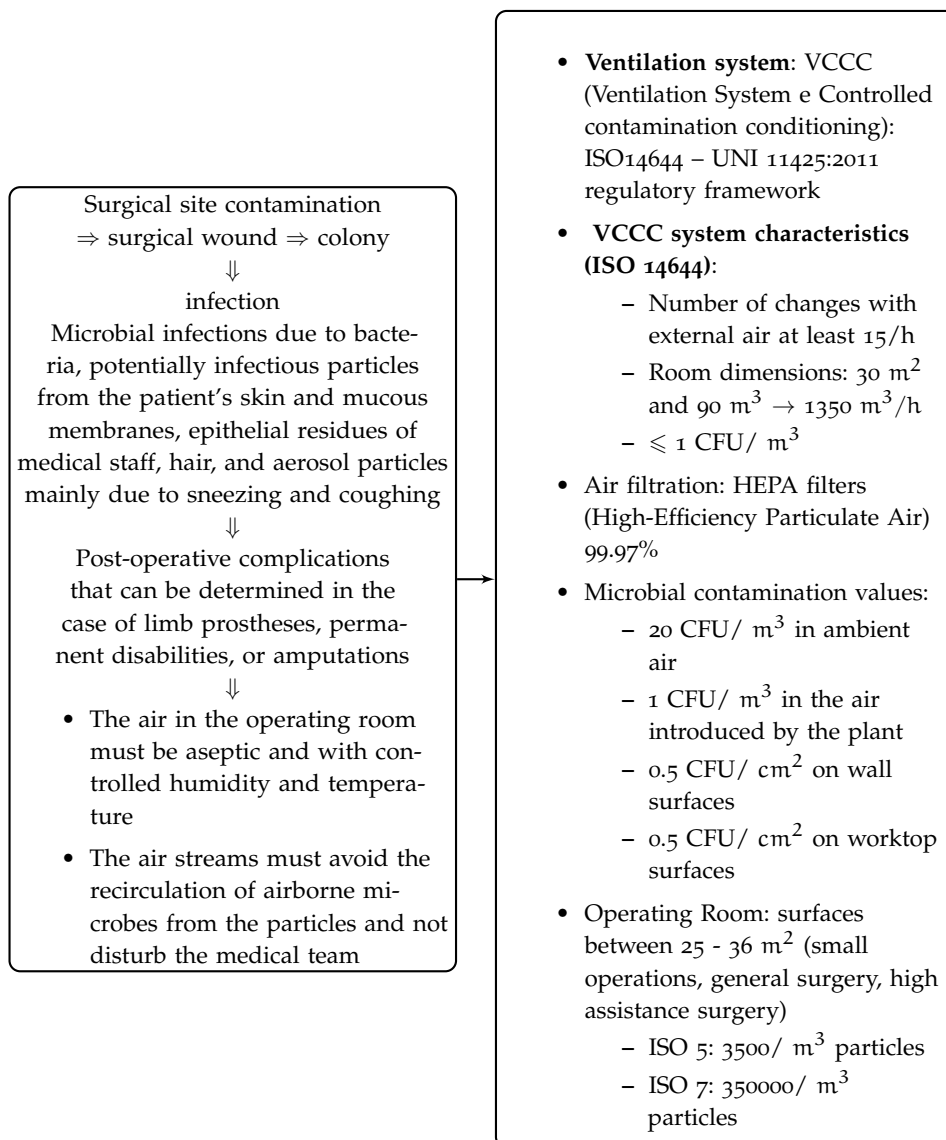


Figure 1.3.1: Surgical site contamination

Characteristics	Operating Rooms		
	very high air quality	high air quality	standard air quality
Temperature (C°)	Winter ≥ 20 Summer ≤ 24		
Relative Humidity (%)	Winter ≥ 40 Summer ≤ 60		
Overpressure (Pa) with respect to the outside	15		
Outside air (vol/l)	15		
Recirculation air	yes	yes	-
Cleaning classes UNI EN ISO14644-1	ISO5	ISO7	ISO8
Final filtration level	H14		
Sound pressure level (dB)	45		

Table 1: Environmental parameters in the operating theatre

Figure 1.3.2 shows the impact of different kinds of operation and ventilation systems on wound contamination.

Variables	Crude analysis			P values	Adjusted analysis		
	Wound contamination, CFU/100 cm <sup>2</sup>				Estimates	OR (95% CI)	P values
	0 (n = 33)	1-10 (n = 21)	>10 (n = 6)				
Procedure							
Cardiac surgery	9 (27.3)	11 (52.4)	6 (100)	<.001	NA		NA
Orthopedic surgery	24 (72.7)	10 (47.6)	0		NA		NA
Type of airflow							
Turbulent	14 (42.4)	15 (71.4)	6 (100)	.01	1.28	3.6 (1.02-12.5)	.05
Unidirectional	19 (57.6)	6 (28.6)	0		Ref		NA
Time from incision to closure, min	145 (116-221)	184 (144-272)	279 (263-326)	.02	0.004	1 (1-1.01)	.16
Air microbial count, time 1	3 (0-7)	6 (2-10)	16.5 (2-42)	.09	NA		NA
Air microbial count, time 2	3 (0-5)	2 (0-6)	14 (1-30)	.16	NA		NA
Air microbial count, time 3	2 (0-6)	4 (1-12)	11 (0-21)	.39	NA		NA
Overall air microbial count	10 (4-25)	12 (4-36)	57 (3-67)	.22	0.01	1 (0.9-1.03)	.39

NOTE. Values are median (interquartile range), n (%), or as otherwise indicated.  
CFU, colony forming units; CI, confidence interval; NA, not applicable; OR, odds ratio.

Figure 1.3.2: Operating theatre and impact on the opening door and their effect on SSI. Reprinted from Birgand et al. [22]

### 1.3.2 Numerical Studies

The section is composed into two parts: the CFD studies, where the recent literature on the CFD numerical studies is reported, and the one on the ROM, FMU, and DT studies, where the ROM concept, FMU, and the DTmodel are briefly presented.

#### 1.3.2.1 CFD studies

CFD is a valid aid for evaluating the best conditions in the operating theater. This way, it is possible to simulate different scenarios and

choose the most appropriate conditions and geometry. Many studies (see, for instance, Di Santis [31], Khankari et al. [47], Massarotti et al. [55], Romano et al. [73], and Romano et al. [74], Balocco et al. [16], Balocco et al. [15], Boer et al. [24], Uyttenhove [86], and Memarzadeh et al. [59]) have used this approach to understand the behavior of airflow in the operating theatre to prevent or decrease post-surgery infection, avoid the contamination wound, and in this way, as published by Sanchez et al. [79], minimize the cost of a new operation.

In Wu et al. [92], an analysis of the ventilation performance in the operating theatres with several ventilation designs, is done. Liu et al. [53] realized a study on the prevention of surgical site infection under different ventilation systems in the operating room environment, see figure 1.3.3. Another solution to resolve the wound contamination problem by managing the airflow is given by Boeret al. [25], and Zhai et al. [94], see figure 1.3.4, where is illustrated a LAD and the air curtains to make a barrier between the operating area and the rest of the room.

In spite of this, simulation of all the possible cases based on any

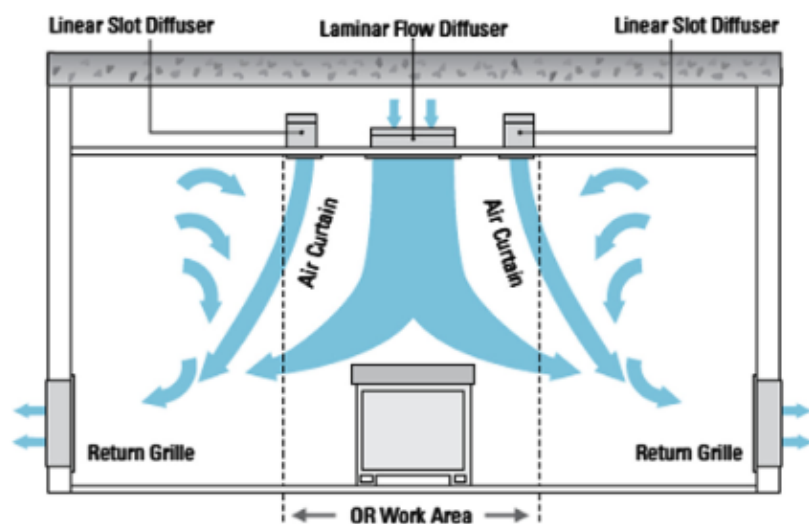


Figure 1.3.3: Sketch of a typical air curtain system. Reprinted from Zhai et al. [94]

combination of the parameters and taking into account the regulatory requirements remains impossible, as it would require a significant amount of time.

### 1.3.2.2 ROM, FMU, DT studies

ROM use gives the possibility of reducing, in part, the calculation times, considering the running only an few number of simulations in a defined parametric range. The advantage of using a ROM is the

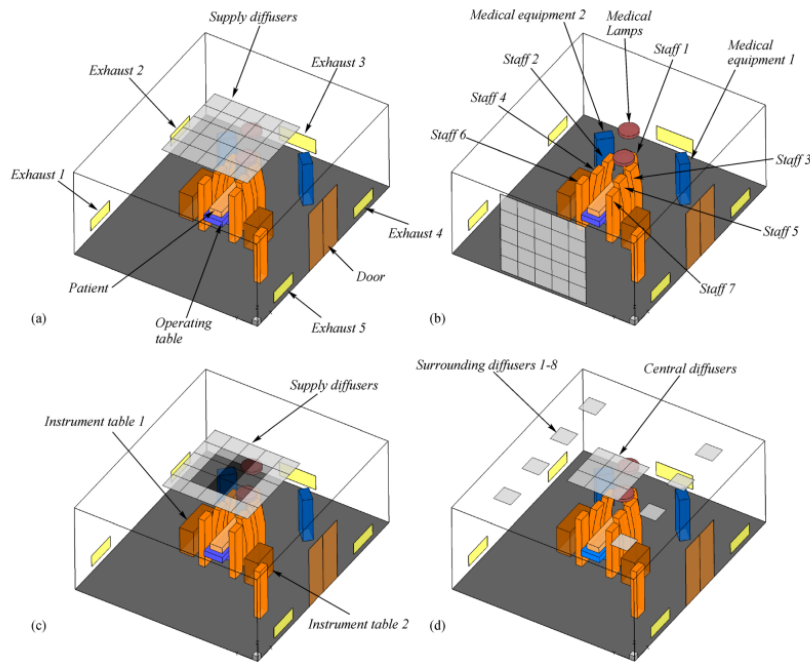


Figure 1.3.4: Description of the several ventilation systems: (a) VLAF, (b) HLAf, (c) DVAf, (d) TAF. Reprinted from Zhai et al. [53]

capacity to vary input variables to return the values of the field or the scalars in a few seconds in the opposite of the CFD simulations, for that is necessary to run them again if we change an input parameter. This ROM capacity is possible thanks to the construction process, which includes using an SVD algorithm (see for instance Weiss [90], Abdi [3], and Ben [18]). Furthermore, once the ROM or the FMU has been generated, it may be possible to develop a control system for the management of HVAC in an operating theatre.

In Tian et al. [84], in Zuo et al. [96], a co-simulation with a CFD code was envisaged in a control system using the Modelica Buildings library which is a free library with source code. The library models, see figure 1.3.5, are used in a dynamic simulation for energy control systems in buildings (HVAC systems, airflow, natural ventilation, contaminant transport, and load prediction on electrical systems). The library has already been used for modeling low-energy systems used for buildings, studying new systems, fault detection, diagnostics, and analyzing unconventional energy and control systems. Concerning that, it may be interesting to build a control and management system for the room's temperature, pressure, and inlet velocity with a simulation that considers a ROM generated FMU model.

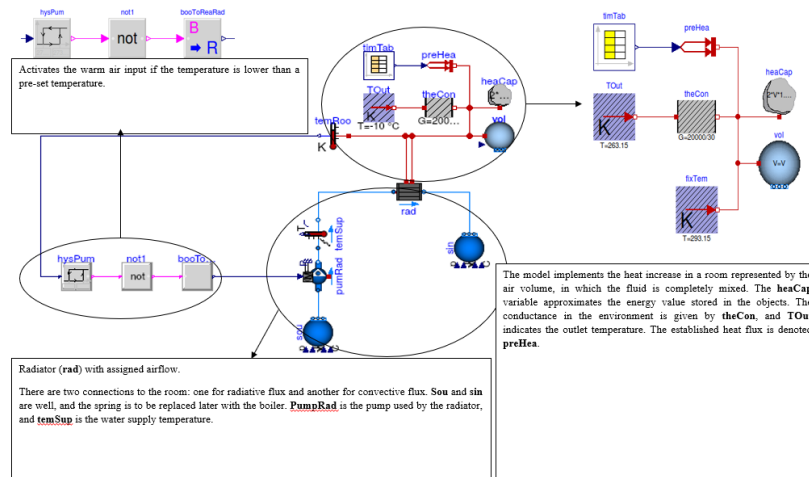


Figure 1.3.5: The figure taken from [97] shows a model that represents the heat exchange in a room to which is added the contribution given by a radiator.

### 1.3.3 Experimental Studies

This section presents the literature, section 1.3.3.1 on small-scale and more commune experiments on full-scale, section 1.3.3.2, which are usually compared with the CFD simulations.

#### 1.3.3.1 Small-scale experiments

Very few experiments were performed on the small-scale model for the operating theatre. Usually, the small-scale models are used to study the field airflow in the room and often use the air as fluid, rarely the water. Among the authors that studied the results obtained on the scale models (Thatcher et al. [83], Tang et al. [81], Araneo et al. [11], Poussou et al. [70], and Mazumdar et al. [56]), who investigate the use of a different fluid from the air in a model scaled (small-scale).

#### 1.3.3.2 Full-scale experiments

Experiments are usually conducted on a real-world scale. The numerical results were compared to experiment results found in the literature by Romano et al. [73], who identified the challenge of reproducing a contamination system by using an artificial contamination system generated by a liquid nebulizer and binary nozzle. The results were compared to those of a CFD simulation. Lee et al. [48] studied the influence of door opening on the interzonal air exchange volume. McNeill et al. [57] used qualitative and quantitative flow visualization techniques to evaluate, in a full-scale chamber, the operating

theatre's air distribution. Liu et al. [52] compared the CFD results to an experiment performed in an operating theatre environment cabin. The dimensions of the cabin were the same as the physical model, as were the size and location of the supply diffusers. The study investigated the effect of a circulating nurse walking on the airflow and BCP. Sadrizadeh [76] considers the experimental benchmark, on a real scale, a test carried out at Aalborg University as a reference to validate CFD predictions of the airflow field. Aganovic et al. [4] investigated the presence of surgical lights that disturbs the flow of ultraclean air in operating rooms using a real operating theatre. Cao et al. [27] researched the performance of LAF and MV to carry out the experimental measurements in two operating theatres equipped with LAF and MV systems. Also, Wang et al. [89] studied a full-scale operating room through field measurements and numerical analyses used to verify the field measurement data. Similarly, Balocco et al. [16] investigated the impact of surgical staff on indoor air quality in uni-directional ventilation in a real operating theatre using the CFD simulations to validate the experimental measurement campaign.

#### 1.4 THESIS SCOPE

The research aims to create a **DT** of an operating theatre. In the literature that we analyzed, we didn't find a DT that reproduces, in an operating theater, entirely the field for interest variables, which usually are reported only the trends of variables.

The build of DT is the first step to using a control system, also remote, to manage the operating theater and discover, in every condition, the best solution in terms of bacterial and airborne reduction and environment comfort. The strength point of the DT is the possibility of deploying it on a simple device and controlling the variables of interest in realtime with the possibility of obtaining the variable values punctually at every point of the operating theater without probs. The DT is a valid aid in managing, controlling, and maintenance operations. Its ability to digitally reproduce various physical elements constituting the parts of complex systems has already been used for some years in optimizing project operations and system management in the mechanical, thermal, and electronic fields. The optimization is obtained by exploiting many simulations to evaluate and adjust the system settings, improve its efficiency, minimize the risks of malfunctioning, and thus reduce costs. Furthermore, the DT is used in terms of maintenance to determine the life in a physical system of the particularly stressed elements and establish the most appropriate moment to maintain or replace the equipment. Through the DT, the anomalies can detect, and possible failures due to a particular anomaly.

However, the relevant aspect is, above all, the possibility for the DT to be able to interface with applications **IIoT** once the elements that will be modeled have been defined. The DT will consider the components and behaviors necessary to interface with the IIoT, thus exploiting the ability of this technology to carry out checks and modifications and transmit the actions to be performed using any device. The integration with the devices takes place through sensors that can be physical or virtual (in case of impossibility to be able to position the sensors on the element of interest). The models, created considering both the physical element and deep learning methods, are updated concerning the data provided by the measurement tools and processed through optimization algorithms to improve the DT to predict future behavior, refine the control, and optimize the functioning of the analyzed physical parts.

It's worth commenting that the proposed approach can be easily extended to other fields such as offices, waiting rooms, common areas, etc., thus obtaining a technology aimed both at air quality control and energy saving in buildings but also at the regulation and management of people flows as well as the maintenance, detection, and management of plant faults.

The research project considers the operating theater design and building of the ROM and the building of DT. We realize an operating theater that appears to be potentially flexible regarding the ventilation system Chapter 6, section §6.8 and from which we can construct the ROM and the DT. The original project established the comparison of the DT and experimental results, but this part, at the moment, has not been possible to complete it.

Summarizing:

- numerical part: DT construction
  - geometry design, CFD setting, and ROM building
  - build the DT from the ROM
- experimental part
  - preliminary CFD test
  - scale model built
  - experimental tests

## 1.5 METHODOLOGICAL APPROACH

The Thesis is organized as follows:

In this **Chapter 1**, we present an overview of the main aspects of the numerical and experimental studies on operating theatres.

In **Chapter 2**, we explore in section §2.2 the several ventilation systems used in the operating theatres. In subsections §2.2.1, and §2.2.2, the standards and guidelines for the building, the operating theatre, and outdoor environments nearby the room are shown.

In **Chapter 3**, the theoretical background is illustrated in several sections, and the computational models are shown. Section §3.1.1 the governing equations, the morph concept, and the concept of ROM are illustrated. Section §3.2 illustrates boundary conditions, numerical mesh generation strategies, and the DoE method to define the points of design and obtain the combinations of parameters that will be used in simulations.

In **Chapter 4** the first attempts to define the geometry, and the parameters that might use in the ROM are shown. Several cases are simulated. **Chapter 5** is dedicated to experimental studies. At the moment of writing the Thesis, it was not possible to complete all the experiments. The Chapter is composed of a part of CFD simulations to understand the possible difficulties in doing the experiments and find a better set-up, and a second part in which the equipment that is will use for the experiments is described.

**Chapter 6** includes two cases with the same geometry but different simulations. Section §6.2 is dedicated to two particular cases: case 6a#, and case 6b#. Case6a# is presented in Chapter 4 and, in this section, has been used as a simplified test case to start building the ROM. Case6b# is the first case where the human dummy is employed; section §6.3 is focused on the comparison and validation of the ROM model, accomplished the results of the validation are then presented in section §6.4, §6.5. The two sections, §6.5, and §6.6 highlight the comparison of results obtained from the CFD, and section §6.7 summarizes the results of the work. The last section and §6.8 considers two simulations with the complete geometry.

**Chapter 7** considers the main conclusions drawn from the CFD analyses and the ROM building applied to the DT.

The thesis includes supplementary material organized in appendices as follows: Appendix §A illustrates the ACH evaluation and the comparison of ACH in the small-scale model and full-scale model; Appendices §B contain a simple tool to obtain the values of water vapor for the calculus of RH; Appendix §C contains some considerations for the evaluation the CO<sub>2</sub> exhaled from the people in the operating theatre. A list of relevant references is included at the end of this thesis. All the simulation runs in this work have been performed using Ansys Fluent version 2021R2 and version 2022R2 <sup>1</sup>, running on HPC dense server with 88 CPU Intel(R) Xeon(R) Gold 6152 CPU @ 2.10GHz and 256 GB RAM. The post-processing has been performed using Ansys

---

<sup>1</sup> ©Ansys. All Rights Reserved

CFD-Post, and Ansys Fluent. The real gas EoS and the evaluation of water vapor have been carried out using Mathematica<sup>2</sup>.

---

<sup>2</sup> ©Wolfram Mathematica, Inc. All Rights Reserved

# 2

---

## VENTILATION AND FILTRATION SYSTEMS

---

### OBJECTIVES OF CHAPTER

This Chapter shows an overview of current ventilation systems in operating theaters, e.g., laminar airflow, turbulent airflow, or mixing airflow. The ventilation systems, to prevent the contamination of surgical sites, decrease wound infections, and provide a comfortable environment to medical staff and patients, are used. We focus the attention on the laminar unidirectional flow, generally considered a good ventilation system for a long time. Only recently, some studies on the main ventilation systems have reconsidered the laminar airflow for some kinds of surgical operations, e.g., orthopedic surgeries, as disadvantageous. Furthermore, the chapter reports the European standards and some of the international standards on ventilation systems in operating theaters, which values in the boundary conditions for the simulations presented in Chapter 4 and Chapter 6 are used.

### 2.1 VENTILATION SYSTEMS

In the previous Chapter 1 in table 1, the environmental conditions for the operating theatre are defined. Better conditions of temperature, humidity, airflow velocity, and particle concentration, can be reached by appropriate design and maintenance of the HVAC equipment, and lighting systems, and the medical accessories within an operating theatre. The parameters, such as temperature, relative humidity, airflow velocity, supply air, and pressure, to obtain control of the contamination and a comfortable environment in an operating theatre should be monitored. Therefore the temperature, the relative humidity, and the airflow velocity tend to be the thermohygrometric condition in an indoor environment, see table 2; moreover, the air supply should not have either high or low values. In fact, in the case of higher values, the growth and the transfer of bacteria transported on the water molecules are increased, and in the case of low values, the blood coagulation rate is increased. Further, the control of the ambient overpressure help to control the concentration of airborne particles and avoid the

Rooms	Temperature [°C]		Relative Humidity [%]		Overpressure with respect to the outside	External air	Recirculation air	Cleaning classes according to UNI EN ISO 1466-1	Final filtration level	Sound pressure level
	Winter	Summer	Winter	Summer	[Pa]	[vol/h]	[-]			[dBA]
Operating theatre with very high air quality	≥ 20	≤ 24	≥ 40	≤ 60	15	15	SI	ISO 5	H 14	45
Operating theatre with high air quality					15	15	SI	ISO 7	H 14	45
Operating theatre with standard air quality					15	15	-	ISO 8	H 14	45

Table 2: Parameters in the operating theaters UNI 11425 [34]. Reprinted from Di Santis [31]

contamination of air from the surrounding.

### 2.1.1 Ventilation Systems in operating theatres

The air quality in an operating theatre is guaranteed by the ventilation system that reduces the particle concentration and gives comfortable working conditions to the medical staff and the patient, see the figure 2; the guidelines consider at least 15 ACH as shown in the figure 2. The dimensions and position of return grilles with respect to the HVAC are also essential to assure the air quality and comfortable conditions and remove the anesthetic gases or other chemical substances which could be aero-transported. Table 3 summarizes the critical elements that can influence the trend of air fluxes. Between the elements are indicated, for instance, the dimensions and position of return grilles with respect to the HVAC as published in the studies by Sadrizadeh et al. [77], the opening doors. In particular, the opening doors determines a variation of pressure and temperature that produce an airflow completely different from the ones aspected increasing the turbulence and influencing the air quality in the operating theatre as in Zhou et al. [95], and Smith et al. [80], see table 4. This effect compromises the important capacity to remove the anesthetic gases or other chemical substances which could be aero-transported in the room. Further, the position and dimensions of surgical lamps, as studied by Cao et al.[27], and Aganovic et al. [4], may be an important factor of distortions in airflow patterns also relating to the inlet airflow.

In Di Santis [31], Romano et al. [74], Sadrizadeh et al. [77], Sadrizadeh et al. [78], Maxemos et al. [69], Traversari [85], Alsved et al. [7], and Liu et al. [53] different kinds of ventilation systems shown in the figures 2.1.1, 2.1.2, and 2.1.3 are studied :

- unidirectional airflow
- turbulent airflow
- upward displacement airflow

Autors (year)	Type of surgery	Ventilation type	Door opening frequency [Openings/h]	Monitoring contamination/ SSI?	Association between door openings and contaminations?	Association between door openings and SSI rate?
Bediako-Bowan et al. (2020) [154]	Abdominal	Mixing <sup>c</sup>	59.3 <sup>a</sup>	SSI	-	Yes
Birgand et al. (2019) [155]	Cardiac/ orthopaedic	LAF/Mixing	20.2	Particles/ CFU	Yes/ Yes	-
DiBartola et al. (2019) [156]	Orthopaedic	Unknown	27.0 – 34.8 <sup>a</sup>	-	-	-
Roth et al. (2020) [157]	Cardiac	LAF	32.4	SSI	-	Yes
Alsved et al. (2018) [20]	Orthopaedic	LAF/Mixing/ TcAF	2.1– 5.6	CFU	No	-
Hamilton et al. (2018) [158]	Total joint arthroplasty	LAF	19.2 – 21.6 <sup>a</sup>	-	-	-
Perez et al. (2018) [159]	Orthopaedic/ general	LAF	12.6– 36.6 <sup>a</sup>	CFU	Yes	-
Teter et al. (2017) [160]	Plastic surgery	Unknown	13.4	Particles	Yes	-
Bohl et al. (2016) [161]	Neurosurgery	LAF	46.2	SSI	-	No
Mathijssen et al. (2016) [162]	Hip revision	Mixing	3.3 <sup>a</sup>	CFU	Yes	-
Elliott et al. (2020) [163]	Cardiac/ general	Unknown	33– 54	-	-	-
Mears et al. (2015) [164]	Joint Arthroplasty	Mixing <sup>b</sup>	16.6	SSI	-	Unclear
Smith et al. (2013) [165]	Orthopaedic	LAF	37.3 <sup>a</sup>	CFU	Yes	-
Andersson et al. (2012) [166]	Orthopaedic	Displacement	37.2 <sup>a</sup>	CFU	-	Yes
Crolla et al. (2012) [167]	Colorectal	Unknown	12.5 <sup>a</sup>	SSI	-	Yes
Panahi et al. (2012) [168]	Total joint arthroplasty	LAF	-	-	-	-
Young and O'Regan (2010) [151]	Cardiac	Unknown	41.4 <sup>a</sup>	SSI	-	Yes
Stocks et al. (2010) [169]	Joint Arthroplasty	Mixing	19.2	SSI	-	Yes
Lynch et al. (2009) [170]	Multiple	Unknown	33.6 <sup>a</sup>	SSI	-	Yes
Scaltriti et al. (2007) [171]	Orthopaedic/ urology/ general	Mixing <sup>b</sup>	19– 50	-	-	-
			56.4 <sup>a</sup>	Particles/ CFU	No/ Yes	-

Table 3: Operating theatre and impact on the opening door and their effect on SSI. Reprinted Sadrizadeh et al. [77].

<sup>a</sup> Calculated based on values given in the article, either information on number of door openings/surgeries and the duration of surgery or openings/minute.

<sup>b</sup> The articles give information on the average ACH.

<sup>c</sup> Non-laminar.

	Airflow distribution concept	Location of supply	Location of exhaust	Air supply conditions as reported in field studies			Air supply conditions as defined by national guidelines		
				Velocity (m/s) Velocity (m/s)	Air change per hour (ACH)	Diffuser size (m2)	Velocity (m/s)	Air change per hour (ACH)	Diffuser size (m2)
Turbulent Flow Air Distribution (TFDA)	The concentration of airborne contaminants is diluted by mixing the supply air with the contaminated OT air	ceiling or wall-mounted	wall mounted near floor	-	11.5-23.8 [2] 12 [3] 15.5-21.3 [16] 50 [17] 5.3-27.6 [18]	-	N/A	≥ 20 [5,11]	N/A
Vertical Laminair Airflow (vLAF)	The unidirectional airflow swipes away the contaminants over the operating microenvironment	Ceiling mounted	Ceiling and/or wall mounted near floor	0.25-0.38 [19]	26-178 [3] 80.5 [16] 58 [17] 15.1-59.9 [3] 67 [19] 100 [20]	2.4 x 2.4-3.2 x 3.2 [2] 3.8 x 1.2-5.18 x 3.83 [3] 3.2 x 3.2 [16] 3.6 x 3.6 [19] 2.75 x 2.75 [20]	#N/A	≥ 20 [5,11]	≥ 3.0 x 3.0 [6] ≥ 3.2 x3.2 [7] ≥ 8 [10] ≥ 9 [13]
Horizontal Laminair Airflow (hLAF)		Wall-mounted	Ceiling and/or wall mounted near floor						
Mobile Laminair Airflow (mLAF)		In the vicinity of the operating table	Ceiling and/or wall mounted near floor	0.5-0.7 [21]	8.4 [22]	0.5 x 0.4 [19] 0.69 x 0.7 [21]	N/A	N/A	N/A 1
Displacement Ventilation Airflow (DV)	Cool air is supplied at floor level and is moved up displacing the contaminated air from the operating microenvironment	Wall mounted near floor	Ceiling or wall mounted near ceiling	0.09-0.15 [19]	21 [19]	-	N/A	N/A	N/A
Temperature-Controlled Airflow (TAF)	Combination of LAF (cool laminar airflow breaking convective currents in the operating microenvironment) and TFW (warm air maintaining temperature gradient)	Both cool and warm air is supplied from the ceiling	Wall mounted near floor	≥ 0.25 [20]	47 [20]	-	N/A	N/A	N/A

Table 4: Characteristics of operating theatre ventilation systems. Reprinted from Sadrizadeh et al. [77]

- mixed airflow

The **unidirectional airflow** is a flow in a preferential direction. This flow works, such as piston flux, and the fundamental concept is to swipe away the contaminants from the clean zone and prevent contaminated air from entering it. In the operating theatre, in older studies, as studied by Traversari [85], the unidirectional plug flow type of ventilation system was also called LAF. In general, a pure laminar flow is very complicated to create because small disturbances of the laminar airflow will result in some turbulence, and the system ventilation LAF usually is called UDF. Usually, this kind of ventilation system is used when low values of contamination above large areas are required and may be a vertical ventilation system, horizontal, or also mobile as shown in Sadrizadeh et al.[78], but when an airflow encounters an object, the unidirectional flow pattern becomes distorted in its proximity.

The **turbulent airflow** has a high velocity of the inlet to produce the convective motions at large scales to increase the diffusion of supply air with the still air present in the room and realize a *perfect mixing of air*.

The **upward displacement airflow** is an air-displacement system that supplies cool air (2-3°C below ambient temperature) above the floor in each room corner and takes advantage of thermal convection. In fact, the airflow is warmed up from the heat load produced in the room by

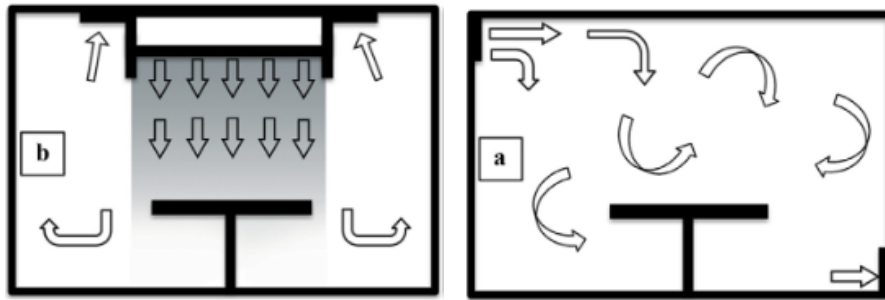


Figure 2.1.1: Figure left is a LAF system, and figure right is a TMA system. Reprinted from Alsved et al. [7].

personnel, equipment, lamps, etc., and through the convection phenomenon, arrives at the ceiling, where are the return grilles, carrying the thermal load and dragging the contaminants.

The **mixed airflow** is a situation where only a part of the room is

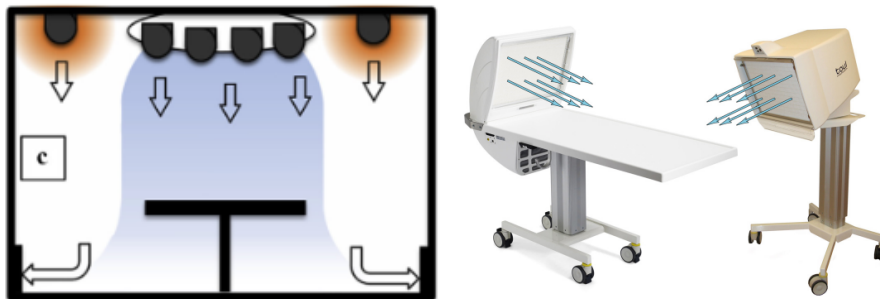


Figure 2.1.2: In figure left, a  $T_cAF$  system reprinted from Alsved[7], and in figure right MLAF system reprinted from Sadrizadeh et al. [78].

involved by a unidirectional flow, in particular, the operating bed, the instrumentation, and the operative area of the staff, while a turbulent airflow invests the other parts. This kind of ventilation system makes some zones with a maximum and others with a minimum particle concentration level, and therefore cleanliness level is not homogeneous.

The filtration system, to guarantee a contamination-controlled environment, addresses a proper number of filtration stages, usually three, installed on an HVAC system, according to UNI EN 1822:2010, [33]. These filters, depending on their position, are compliant with the European reference standard about the high and very high-efficiency filters, and the UNI EN 779:2012 [36], the standard European for the general ventilation filters.

The standards UNI EN 1822 **UNI EN 1822:2010**, [33], now UNI EN 1822 **UNI EN 1822:2019**, classifies the filters according to the performance obtained from tests. In particular, the particles used to test the capacity of filtering have a size range between  $0.2 \mu\text{m}$  and  $0.3 \mu\text{m}$  and the airflow rate to verify the filters are between  $0.24 \text{ m}^3/\text{s}$  and

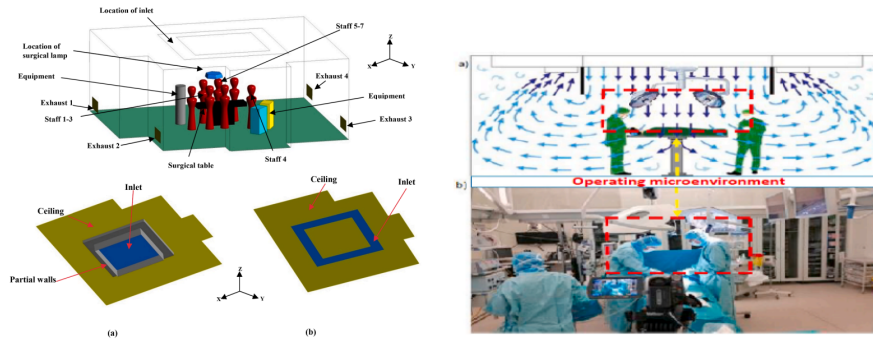


Figure 2.1.3: In the figure left, it is indicated (a) UDF ventilation and (b) Mixing ventilation, Reprinted from Sadeghian[75]. In figure right (a) schematic airflow from a LAF and (b) vertically installed LAF, Reprinted from Sadrizadeh et al. [77].

$1.5 \text{ m}^3/\text{s}$ . In addition, the filter tests consider the maximum final test pressure drop for both coarse filters (G), medium (M), and fine (F) filters.

The **UNI EN 779:2012** [36] concerns the high-efficiency particulate and ultra-low penetration air filters (EPA, HEPA, and ULPA) in the ventilation and air conditioning system. This standard considers the following:

- Classification, performance testing, marking
- Aerosol production, measuring equipment, particle counting statistics
- Testing flat sheet filter media
- Determining leakage of filter elements
- Determining the efficiency of filter elements

as summarised in In Santis [31], and as it is shown in the table in the figure 2.1.4.

The European standards indicate three filtration stages for the incoming air:

- the first filtration stage is installed in the HVAC device. The filter is class F5 (or F7, UNI EN 779:2012, [36]), and the lifetime should be limited to 12 months
- the second filtration stage is installed in the HVAC device. This filter is class F9, and the lifetime should be limited up to 24 months

Filter Group Filter Class	Integral value		Local value <sup>a b</sup>	
	Efficiency (%)	Penetration (%)	Efficiency (%)	Penetration (%)
E 10	≥ 85	≤ 15	--- <sup>c</sup>	--- <sup>c</sup>
E 11	≥ 95	≤ 5	--- <sup>c</sup>	--- <sup>c</sup>
E 12	≥ 99,5	≤ 0,5	--- <sup>c</sup>	--- <sup>c</sup>
H 13	≥ 99,95	≤ 0,05	≥ 99,75	≤ 0,25
H 14	≥ 99,995	≤ 0,005	≥ 99,975	≤ 0,025
U 15	≥ 99,999 5	≤ 0,000 5	≥ 99,997 5	≤ 0,002 5
U 16	≥ 99,999 95	≤ 0,000 05	≥ 99,999 75	≤ 0,000 25
U 17	≥ 99,999 995	≤ 0,000 005	≥ 99,999 9	≤ 0,000 1

<sup>a</sup> See 7.5.2 and EN 1822-4.  
<sup>b</sup> Local penetration values lower than those given in the table may be agreed between supplier and purchaser.  
<sup>c</sup> Group E filters (Classes E10, E11 and E12) cannot and shall not be leak tested for classification purposes.

Figure 2.1.4: EPA, HEPA, ULPA filters, UNI EN 1822-1 [33]. Reprinted from Di Santis [31]

- the third filtration stage is positioned at the end, near the ceiling of the operating theatre. This filter is at least H13 (UNI EN 1822-1 [33]) and can achieve a considerably longer service life.

## 2.2 STANDARDS REFERENCES

By using the DT in the operating room, not only will airborne particles be monitored for scattering, but it will also be possible to instantly simulate the scenarios that can arise when the variables of interest (e.g., temperature, pressure, velocity) change.

The first document to classify the clean room is ISO 14644-1. In 2012 the normative was completed and updated, and the ISO 14644-2 introduced in 2012 and 2015. The normative is divided into ten parts:

- Part 1 (2001): Classification of air cleanliness
- Part 2 (2000): Specifications for testing and monitoring to prove continued compliance with ISO 14644-1
- Part 3 (2006): Metrology and test methods
- Part 4 (2004): Design, construction, and start-up
- Part 5 (2005): Operations
- Part 6 (2008): Terms and definitions
- Part 7 (2005): Separative devices
- Part 8 (2007): Classification of airborne molecular contamination

- Part 9 (2012): Classification of surface cleanliness by particle concentration
- Part 10 (2013): Classification of surface cleanliness by chemical concentration

#### 2.2.1 UNI EN ISO 14644

The standard European and national have originated from the standard used in the clean room, e.g., for particle contamination, ISO 14644 [35]. ISO 14644-5:2004 specifies basic requirements for cleanroom operations. We are considering only the aspects concerning the contamination. The classes of cleanrooms used to produce all types of products are defined in the document, and the specific requirements for individual industries are not considered. ISO 14644-2 and ISO 14644-3 covered particle monitoring, and ISO 14698-1 and ISO 14698-2 micro-organisms monitoring.

#### 2.2.2 UNI EN ISO 11425:11: Italian standards

The standards give recommendations for the design, installation, control performance, and management of systems and components used for environmental contamination control and the maintenance of pre-set thermo-hygrometric conditions in departments allocated for the surgical activity (operating blocks). The standard applies to new constructions and building and/or plant renovations of operating blocks and provides the minimum requirements for verifying the conditions of use of existing ones UNI EN ISO 11425:11, [34]. If the VCCC is defined similarly to a *process*, Di Santis [31], are valid the requirements to ensure the quality of the process, UNI EN ISO 14644 [35], EU-GMP [29], and FDA [39]. The standards indicate the goal of VCCC plants of surgery operating theaters, different surgical applications, and the respective cleanliness levels: from ISO 5 to ISO 8, where the higher numbers specify that the operative theatre is used for low-invasive surgery and short duration. The ISO class depends on the maximum number allowed of total particles of a specified diameter (in the operating theatres, the reference diameter is 0.5  $\mu\text{m}$ ) per meter cube of air. The main velocity of airflow in the area critical, near the operating table, is under 3m/s to avoid the development of eddies. For connected environments to the operating theatre, there is an implementation of the legislation in the guideline, the ISPE SL [67], that defines some requirements during the design stage. In addition, based on the D.P.R 14/1/1997, the number of air changes per hour, 15 ACH or more, is established.

The complex system of the operating theatre implies multiple aspects: the filters with the measurements of the pressure drop by a manometer, the airflow control and ACH, with least 15 ACH, pressure difference with at least 5 Pa, temperature and relative humidity with the temperature between 20 °C and 24 °C and the relative humidity between 40% and 60%, the lightning of lamps, and the noise level. The last point (noise level) uses the values defined in French, German, Swiss, Austrian, and English regulations.

Different tests are defined to verify the operative conditions of the operating theatre: a recovery time test, monitoring of microbiological contamination test, and particle contamination and classification test. In other countries, there are similar standards, but sometimes the values range shows the differences. The differences sometimes depend on several positions of ventilation systems and kinds of ventilation systems that imply different tests.

In English standards, e.g., there are two parts of interest: the first about the ventilation systems and the second about the validation of specialized ventilation systems.

The Swedish technical specification, instead, gives importance to the strategy to minimize the airborne contamination of surgical sites in operating theatres and adjacent rooms and prevent postoperative infections caused by airborne micro-organisms.

The ANSI/ASHRAE/ASHE Standard 170-2013 [12] defines the design requirements of the ventilation system. To aim is to provide environmental control for comfort and asepsis in healthcare buildings, and a division in class is done, for the operating theatres, to classify the surgical procedures they can provide.

# 3

---

## THEORETICAL BACKGROUND

---

### CHAPTER OBJECTIVES

This Chapter briefly presents the governing equations used from the CFD software Ansys Fluent. The use of the DoE for the design research, points allow us to obtain, in a specific interval, an optimal set of combinations of parameters determined based on the chosen method. These parameters will be used in CFD simulations, whose results will form the basis for the construction of the ROM.

### 3.1 THEORETICAL BACKGROUND

The CFD model involved the construction of a finite volume computational mesh. We use the commercial software *Ansys Space Claim* with which it was possible to modify the geometries created in *Design Modeler* and subsequently create, using the *Meshing by Fluent*, the computational mesh.

#### 3.1.1 CFD governing equations

The commercial software Fluent Ansys [8] is employed for the CFD to evaluate the airflow in the theatre chamber. The geometry is realized using *Ansys Space Claim*, and a finite volume computational mesh is built using *Meshing by Fluent*.

Though the changes in the temperature and the various thermal energy sources, as shown by X. He et al. [45], the airflow in the operating theatre has a small Mach number. The compressibility effects are negligible (the convective time scales are more relevant than the acoustic ones). The incompressible ideal gas law is considered, see equation 3.1.1, and the equations 3.1.2, 3.1.3, and 3.1.5, define the law of conservation of mass, conservation of momentum, conservation of energy and equation 3.1.4 is shown the tensor stress equation used in the equation of conservation of momentum. In addition, the law of conservation of species, see equation 3.1.6, is written

$$\rho = \frac{P}{\frac{R}{M_w} T} \quad \text{Incompressible ideal gas law (3.1.1)}$$

$$\frac{\partial \rho}{\partial t} + \nabla \cdot (\rho \mathbf{v}) = S_m \quad \text{Conservation of mass (3.1.2)}$$

In equation 3.1.2 the term  $S_m$  is the mass added to the continuous phase from the dispersed second phase.

$$\frac{\partial \rho \mathbf{v}}{\partial t} + \nabla \cdot (\rho \mathbf{v} \mathbf{v}) = -\nabla p + \nabla \cdot (\bar{\boldsymbol{\tau}}) + \rho \mathbf{g} + \mathbf{F} \quad \text{Conservation of momentum (3.1.3)}$$

In equation 3.1.3,  $p$  is the static pressure,  $\bar{\boldsymbol{\tau}}$  is the stress tensor given in equation 3.1.4 where  $\mu$  is the viscosity, and  $\mathbf{I}$  is the unit tensor.

$$\bar{\boldsymbol{\tau}} = \mu \left( (\nabla \mathbf{v} + \nabla \mathbf{v}^T) - \frac{2}{3} \nabla \cdot \mathbf{v} \mathbf{I} \right) \quad \text{Tensor stress (3.1.4)}$$

$$\begin{aligned} \frac{\partial \rho E}{\partial t} + \nabla \cdot (\mathbf{v}(\rho E + p)) = \\ \nabla \cdot \left( k_{eff} \nabla T - \sum_j h_j \mathbf{J} + (\bar{\boldsymbol{\tau}} \cdot \mathbf{v}) \right) + S_h \quad \text{Conservation of energy (3.1.5)} \end{aligned}$$

In equation 3.1.5, the term  $k_{eff}$  is the effective conductivity given by:  $k_{eff} = (k + k_t)$  with  $k_t$  turbulent thermal conductivity; the  $\mathbf{J}_j$  is the diffusion flux of species, and  $S_h$  includes the heat of chemical reaction and other volumetric heat sources.

$$\begin{aligned} \frac{\partial \rho \phi_k}{\partial t} + \frac{\partial}{\partial x_i} (\rho u_i \phi_k - \Gamma_k \frac{\phi_k}{\partial x_i}) = S_{\phi_k} \\ k = 1, \dots, N \quad \text{Conservation of species (3.1.6)} \end{aligned}$$

In equation 3.1.6, the local mass fraction of each species is  $\phi_k$ , the  $\Gamma_k$  is the diffusion coefficient, and  $S_{\phi_k}$  is the source term supplied by you for each of the  $N$  scalar equations.

### 3.1.2 Time Discretization: Pseudo Transient Method

The simulations envisaged the use of the pseudo-transient method, a method which, in order to converge to the final stationary solution, adds an artificial transitory term to the equation being solved; this allows the solution to "advance" in "time". However, since the flow is stationary, the transient changes tend to zero when convergence is achieved, and thus the steady state solution is obtained. A pseudo-time method is a form of implicit under-relaxation where it is possible to give a Local or Global Time Step, and it depends on the solution method used. The default values of under-relaxation parameters are set to values that work for most cases. When the pseudo-time method is applied, an advanced implicit under-relaxation is dynamically used on the relaxation factor during the simulation according to the flow field behavior.

In the generic transport equation, equation 3.1.7, the integral form of governing equation using the pseudo-time method for a steady-state case is:

$$\int_V \frac{\partial \rho \Phi}{\partial \tau} dV + \oint_S \rho \Phi \bar{v} \cdot d\bar{A} = \oint_S \Gamma_\Phi \nabla \Phi \cdot d\bar{A} + \int_V S_\Phi dV \quad (3.1.7)$$

In the discretized governing equation using the finite volume method, a term  $\Delta\tau$  appears for the steady-state equation. This term is the pseudo time step size that can be computed using the local or global time step method, equation 3.1.8 (PTS discretization of generic transport equation):

$$\rho_p \Delta V \frac{\Phi_p - \Phi_p^{\text{old}}}{\Delta\tau} + a_p \Phi_p = \sum_{nb} a_{nb} \Phi_{nb} + b \quad (3.1.8)$$

where  $\Phi_p^{\text{old}}$  denotes the value of  $\Phi_p$  at the previous iteration and  $\Delta\tau$  is the pseudo-time step. When in governing equations, we have the  $\tau \rightarrow \infty$ , the original form of the equations is recovered.

This technique permits us to resolve the steady state by setting an initial time guess and using a time step to evolve the solution forward; when we obtain a new value, this is set as an initial value. The value of pseudo time depends on the size of the elements of the mesh.

### 3.1.3 Morphing concept

RBF-based mesh morphing is obtained by imposing a displacement on a set of points (called source points); this displacement field is interpolated and applied to the nodes of the computational model (target points). The interpolation result depends on the radial function and the support. The RBF calculates unknown weight functions and polynomial terms from known data. The general form of the interpolation function and the polynomial is shown in equation 3.1.9, as published in the studies by Biancolini [20].

$$s(\mathbf{x}) = \sum_{i=1}^N \gamma_i \varphi(\|\mathbf{x} - \mathbf{x}_{ki}\|) + h(\mathbf{x}) \quad (3.1.9)$$

The scalar function  $s(\mathbf{x})$  is defined for each arbitrary point in space  $\mathbf{x}$  and represents a transformation  $\mathbb{R}^n \rightarrow \mathbb{R}$ . The movement of a point can be considered as the Euclidean distance between source  $\mathbf{x}_{ki}$  and target points  $\mathbf{x}$  multiplied by the radial function  $\varphi$  and the weight  $\gamma_i$ . The polynomial  $h(\mathbf{x})$  is added, and its minimum degree depends on the choice of the basis function, equation 3.1.10:

$$h(\mathbf{x}) = \beta_1 + \beta_2 x + \beta_3 y + \beta_4 z \quad (3.1.10)$$

The desired function values  $g_s$  are obtained at source points, equation 3.1.11:

$$s(\mathbf{x}_{ki}) = g_i, \quad 1 \leq N \quad (3.1.11)$$

The system is completed when the orthogonality conditions are verified for all polynomials  $p$  with a degree less or equal to that of polynomial  $h$  equation 3.1.12:

$$\sum_{i=1}^N \gamma_i \varphi(\mathbf{x}_{ki}) \quad (3.1.12)$$

In equation 3.1.13, the interpolation is shown of a 3D set of displacement at source points.



composed into three matrices, e.g., as in Weiss [90]: two orthogonal (P, Q) and one diagonal ( $\Sigma$ ), equation 3.1.14:

$$\mathbf{M} = \mathbf{P}\Sigma\mathbf{Q}^T \quad (3.1.14)$$

The properties of the SVD imply that the matrix M can be approximated as a linear combination of r modes (the first r left singular vector, [9]). The accuracy of the approximation is shown to follow equation 3.1.15:

$$\text{RRRMSE} = \frac{\| \mathbf{M} - \mathbf{M}_r \|}{\| \mathbf{A} \|} = \sqrt{\frac{\sum_{i=r+1}^n \sigma_i^2}{\sum_{i=1}^n \sigma_i^2}} \quad (3.1.15)$$

It is possible to write the solution field X in design space, equation 3.1.4:

$$\mathbf{X} = \sum_i^r \alpha_i \mathbf{P}_i \quad (3.1.16)$$

Considering that the number of modes is an important element for constructing ROM, this number must be large enough to obtain an accurate data representation but small enough to compress the data without including measurement noise. In the case of small r values, the projection errors are almost the same. For the construction of the ROM, we need a response surface of mode coefficients  $\alpha_i$ , equation , an interpolation obtained using the learning snapshot, and a genetic aggregation algorithm; it is possible to write the equation in term of the equation 3.1.17.

The number of selected singular values r gives the tolerance error, and the result of the approximation is given by the modes. Each dataset case can be linearly expressed through a set of scalar coefficients by exploiting the genetic aggregation response surface (GARS) technique, as in the work of Ben Salem et al. [17]. The variable v, equation 3.1.17, is considered as the aggregation of the product of the response surface factor and the mode data for all of the modes n.

$$v(\mathbf{x}) = \sum_{i=1}^r \text{GARS}_i(\mathbf{x}) \text{mode}_i(\mathbf{x}) \quad (3.1.17)$$

In practice, the construction of the ROM involves the division of the snapshots into two groups, the learning one, which will build a basis of modes used to express each solution as a linear combination of the modes, and the validation one. The construction of a ROM with a different learning set but the same number of snapshots or with the

addition of snapshots to the same set generates a variation in terms of the relative error of the ROM, as well as a possible variation in the number of modes. Just as written, the construction of the ROM provides for the division of the snapshots into two groups:

- *learning group*
- *validation or validation group*

The learning group will build a mode base to express each solution as a linear combination of modes. We obtain a curve called *Reduction*, which represents the precision of the learning set with respect to the number of modes, and a curve called *LOO*, which is the precision of the base of the modes for a snapshot not included in the learning set, see also, the figure 6.4.7. The separation between the two curves is considered the point with the optimal number of modes beyond which the addition of further modes is no longer advantageous for constructing the ROM. Each mode contributes energy to the ROM. Particular attention in the construction of the ROM is given to:

- *relative reduction error*: it is the difference between the reference solution of each field snapshot concerning the projected one, that is, the projection of the reference solution concerning the number of modes of the base. The equation 3.1.18 illustrates the projection of  $X_{ref}$  in the  $r$  modes basis; in this equation, the  $X_{proj}$  are the projections.
- *ROM relative error*: includes both reduction and interpolation errors. This error, therefore, varies as the number of modes chosen varies. The equation 3.1.19 defines the relative ROM error for every design point, i.e., every combination of the parameters. The equation 3.1.19 considers the difference between the  $X_{ref}$  is the solver field, and the  $X_{ROM}$  and the ROM predicted.

Once the error requirements have been met, the ROM obtained will be exported to TB, and it will be possible to obtain, as the input parameters vary over time, snapshots of the temperature field.

$$RRE = \frac{\| X_{ref} - X_{proj} \|}{\| X_{ref} \|} \quad (3.1.18)$$

$$ROMRE = \frac{\| X_{ref} - X_{ROM} \|}{\| X_{ref} \|} \quad (3.1.19)$$

In addition, it is possible to define the *maximum absolute ROM error* equation 3.1.20 and, in equation 3.1.21, the *maximum absolute error* of

each snapshot with respect to the ROM built with a given learning selection.

$$\text{MAROME} = \max_{i=1,\dots,N} |X_{\text{ref}_i} - X_{\text{ROM}_i}| \quad (3.1.20)$$

$$\text{MAE} = \max_{i=1,\dots,N} |X_{\text{ref}_i} - X_{\text{proj}_i}| \quad (3.1.21)$$

In the end, another error must be considered: the *interpolation error*. This error depends on the interpolation of the mode coefficients in the equation 3.1.4 and can be obtained by subtracting the reduction error from the ROM error.

### 3.2 COMPUTATIONAL MODEL AND MESH

The numerical analysis was carried out through CFD simulations which envisaged using the commercial software *Ansys Fluent* [10]. The numerical approach used is the RANS with a PBS solver. The simulations are first-order upwind for the momentum, turbulence, and energy equations with a method of coupling between pressure and velocity and second-order for the species. The transport of species is added to the continuity, momentum, and energy equations, and the standard  $\kappa$ - $\epsilon$  with a standard wall function was used for the turbulence and a pseudo transient for the time. The CFD model involved constructing a computational mesh with finite volumes. Using the commercial software *Ansys SpaceClaim*, it was possible to modify the geometries created in *Design Modeler* and subsequently create, using the *Fluent Meshing*, the computational mesh.

The DoE was used for the research of the project points; it has been possible to obtain, according to the relevant regulations standards, ASHRAE, A.[12], UNI EN ISO 14698:1-2 [32], UNI EN 1822 - parts 1-4 [33]. An algorithm of the "OptimalSpace-Filling Design" type was opted for with a "design type" that considers the maximum and minimum values of the parameters to ensure them sufficient distribution in the field.

#### 3.2.1 Boundary conditions

The boundary conditions used in the cases analyzed are a uniform velocity at the inlet and a set pressure at the outlet. To represent the medical staff was defined as a material called 'human'. This material has features similar to the human body and heat flux in agreement with one used in Balocco et al. [16], Massarotti et al. [55], Romano et al. [73], McNeill et al. [58]. In addition, the mixture material composed by

vapor water to evaluate RH, and CO<sub>2</sub> molar fraction of CO<sub>2</sub> emitted in the exhalation phase during respiration equal to 80 l/h, as published by Balocco et al. [15], have been considered.

### 3.2.2 A method for calculating the DoE

Once the appropriate ranges of variation have been defined for the parameters of interest, whether they are physical or geometric (temperature, HVAC inlet velocity, pressure, the molar fraction of water vapor, and as a geometric parameter, position), based on the regulatory standards, one chooses the most convenient method, based on the problem, which guarantees the appropriate number of combinations.

In the cases studied, an algorithm of the "OptimalSpace-Filling Design" type was opted for with a "design type" which considers maxima and minima to ensure sufficient coverage of the field for each parameter, and several samples assigned by the user, see figure 3.2.1. The number of recommended required minimum combinations is  $8 \times$  (number of input parameters).

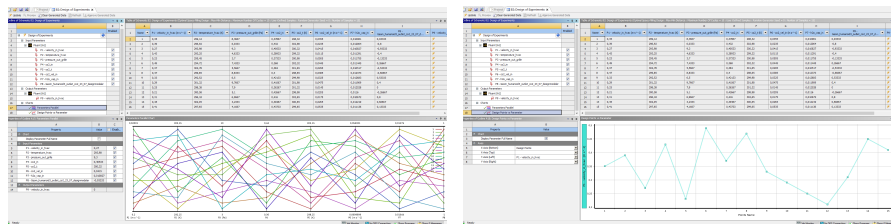


Figure 3.2.1: On the left, the trend between the minimum and maximum of the different input parameters. On the right is the trend of one of the input parameters with respect to the number of samples.

# 4

---

## CASE STUDIES: METHODOLOGY

---

### OBJECTIVES OF CHAPTER

The Chapter reports the preliminary analysis to define a ROM. The analysis, realized in four steps, defines the setup of simulations. A first simulation, realized to generate a ROM is realized, and a simple room model with an HVAC was built in the first step, case 1#, figure 4.4.1. The aim of this simple simulation is to obtain, in a short time, preliminary feedback and verify the good approximation of variable fields and the trends of the quantities of interest. Three steady-state simulations, case 3#, case 4#, and case 5#, with different degrees of mesh refinement, and a pseudo-time step, have been performed; numeric is characterized by first-order discretization and 3rd-order residuals. In addition, a new material called "human" was created. We ran an unsteady state simulation, case 2#, to understand the behavior of the injection of particles and the critical elements for future development.

### 4.1 CASE STUDIES

#### 4.1.1 *Operating Theatre geometry: case study*

The geometry of operating is similar to that of the Monza Hospital. The geometry of the operating theatre shown in figure 4.1.1, (7m x 7m) has a surface of 49 m<sup>2</sup>, a height of 3m, and 8 discharge grates, 4 upper and 4 lower, respectively, of dimensions (0.6m x 0.3m) and (0.9m x 0.3m) as reported in Di Santis [31].

### 4.2 MAIN STEPS

To obtain the DT, we proceeded gradually; we started by considering a simple geometry of the room, without elements (medical stuff, lamps, surgical table, monitor, and other surgical equipment) up to obtaining the final DT by means of successive numerical and geometrical im-

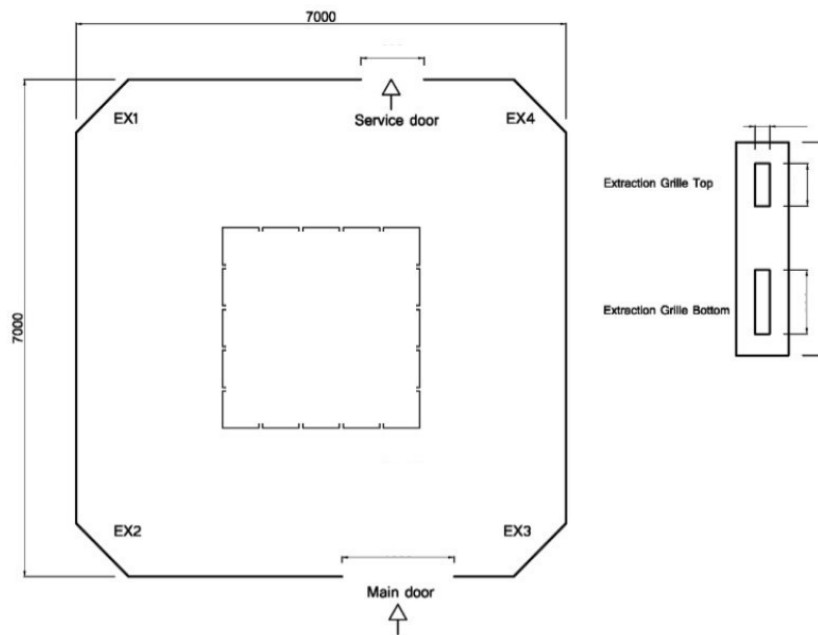


Figure 4.1.1: Sketch of the geometry of the operating theatre, Romano et al. [73]

provements. Table 5 summarizes the procedure steps and the respective cases.

1. The first step to start studying the problem from a CFD and ROM construction point of view was to build an elementary model, a simple room with an HVAC with an air inlet and outlet.
2. The second step required the construction of a more complex geometry, and it was taken as a reference in terms of geometry and dimensions of the room, dimensions and position of the HVAC, the operating theater of the Monza hospital analyzed in Di Santis [31]. A very similar geometry has been reproduced, considering a similar airflow introduced by the HVAC but with the HVAC consisting of a single grid from which the air is introduced with a uniform speed. A steady-state and unsteady simulations were carried out, and the introduction of inert particles into the chamber was also simulated.
3. The third step involved introducing an element into the operating room. This element represents a medical staff member, and in the first phase, it was approximated with a cylinder. The purpose was to study both the response of the variables (e.g., temperature field on the cylinder surface, distribution of the temperature and velocity of the air in the chamber) when changing the physical (temperature, velocity, etc.) and/or geometric

parameters (the position of the cylinder) and the conditions for which the cylinder temperature remains within an acceptable range. A thermal flux was given on the cylinder according to the studies in Balocco et al. [16], Pasquarella et al. [65], and the material was created with specific values for density, specific heat, and thermal conductivity. Finally, the relative ROM was built using TB.

4. The fourth step involved replacing the cylinder with a mannequin with human features. The mannequin represents an element of the medical staff. Moreover, the specie  $H_2O$  has been added to define the percentage of **RH**, with the subsequent addition of the molar fraction (it will be chosen as in Balocco et al. [16] of  $CO_2$  to simulate breathing, see Appendix C. Finally, the obtained ROM was exported in TB to realize a DT.

Case number	Step numbers			
	step#1	step#2	step#3	step#4
1#	V	X	X	X
2#	X	V	X	X
3#	X	V	X	X
4#	X	X	V	X
5#	X	X	V	X
6#	X	X	V	V

Table 5: Table shows the number of cases and the related step.

The DT was constructed for case 2# and case 6 #, as we will show in Chapter 6.

After the ROM generating, which can be integrated into a scheme with lumped parameters created in Modelica, using this scheme, it was possible to transmit data, temperature, pressure, and relative humidity, as ROM input variables. In this way, we would have liked to realize a controlling and managing quality air system in the operating theater, as illustrated in section 1.3.2 through Modelica, see Zuo et al. [96].

The first necessary comparison is between the values of a field, e.g., temperature, obtained from a single combination of input parameters of the ROM and the CFD for that combination, see section 6.7. Subsequent comparisons should be made between the experimental data obtained from the measurements with those obtained from the ROM or between measurements made on plexiglass scale models and the previously validated CFD-ROM results.

### 4.3 SETTINGS

Table 6 shows the main boundary conditions and initial conditions given in the operating theater for every case, and the reference values used for the first tests refer to those of the UNE standards, [1]. Cases 3#, 4# and 5# have a different mesh refinement: in particular, case 3# and case 4# have respectively 370k and 330k volume elements but with a different offset for the boundary layer, and case 5 # has 3 millions of volume elements.

Case number	Variables			
	Room temperature [K]	HVAC temperature [K]	HVAC velocity [m/s]	Room Pressure [Pa]
1#	298.15	293.15	0.3	1325
2#	298.15	293.15	0.1	1325
3#	298.15	293.15	0.3	1325
4#	298.15	293.15	0.3	1325
5#	298.15	293.15	0.3	1325

Table 6: Table shows the main values of setup for the cases: case 1#, case 2 #, case 3 #, case 4 #, case 5 #.

The table 7 shows an overview of parameters and of value ranges used in the complete simulations will show in Chapter 6, section 6.4.1. The reference values used for the first tests refer to those of the UNE standards [1].

In the simulations of cases 3#, 4#, and 5#, convergence to the third order and a numerical spatial discretization to the first order for the energy, momentum, and turbulence equations was required.

Parameter	Min value	Max value
Velocity [m/s]	0.1	0.5
Temperature [K]	291.15	310.15
$\Delta$ Pressure [Pa]	2.0	8.0
Molar Fraction H <sub>2</sub> O	0.01	0.031
Position human dummy [m]	-1.0	1.0

Table 7: Range of variation of the input parameters.

#### 4.4 FIRST STEP: CASE#1

Ansys Workbench and Design Modeler were used to create the elementary model, see figure 4.4.1, with the dimensions defined in table 8.

	Room dimensions [m]	HVAC dimensions [m]	Walls	HVAC walls
Case#1	3.65x3x5	1.2x0.5x0.5	aluminum	aluminum

Table 8: Dimensions of the case1# chamber.

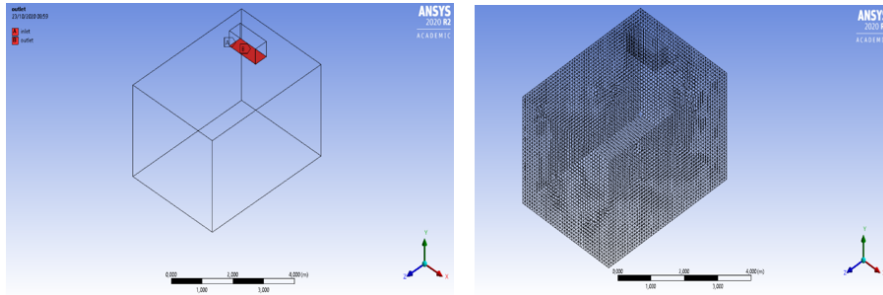


Figure 4.4.1: The figure on the left shows the geometry of a room with an HVAC on which the inlet and outlet of the airflow are indicated. On the right, the same geometry is represented with a mesh with predominantly hexahedral quadrangular elements case #1

The model has been imported into Fluent, figure 4.4.1, and the initial and boundary conditions are shown in the table 9. The flow considered is turbulent, and we use a  $\kappa - \epsilon$  with a wall function, and the solution method is a **RANS**. Finally, the CFD simulations generated files (snapshots), which were imported into the TB software and with which the ROM was created. From the ROM, it is then possible to create, if we want, the FMU model. This model, integrated into a control system, should allow, through a DT, which can be interfaced with a platform, the management of the parameters of interest or maintenance interventions in real-time, considering the possible options to intervene safely in repairing the fault in the rooms considered.

Case 1#	
HVAC output velocity [m/s]	0.1
Room temperature [K]	300
HVAC outlet temperature	295
Pressure [Pa]	101325

Table 9: Initial and boundary conditions in the room and for the HVAC case 1#.

Figure 4.4.2 illustrates the velocity field with current lines for a first attempt hall.

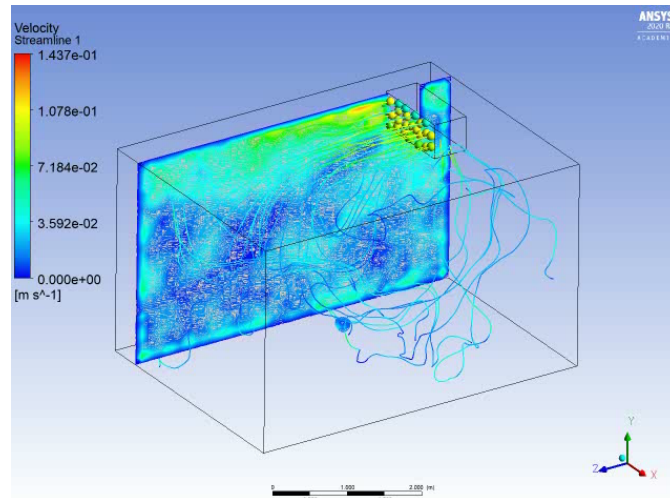


Figure 4.4.2: The figure shows the velocity field on a section of the chamber and HVAC with power lines. The maximum velocity is highlighted in proximity to the exit. HVAC and ceiling case 1#

#### 4.5 SECOND STEP: CASE 2#

In this step, we have also paid attention to unsteady simulations. In particular, have been injected, in the operating theater, with a flow rate of 1e-20 Kg/s, injection velocity 0.3 m/s, and a temperature of 293 K, aggregate particles with different diameters, 5e-7 m and 1e-6 m, see figure 4.5.1. The geometry dimensions have been defined in table 10. The boundary and initial conditions of the transient simulation have been indicated in table 11. The goal of this simulation has been to consider in the future an unsteady case with the injection of particles from which we will build the ROM.

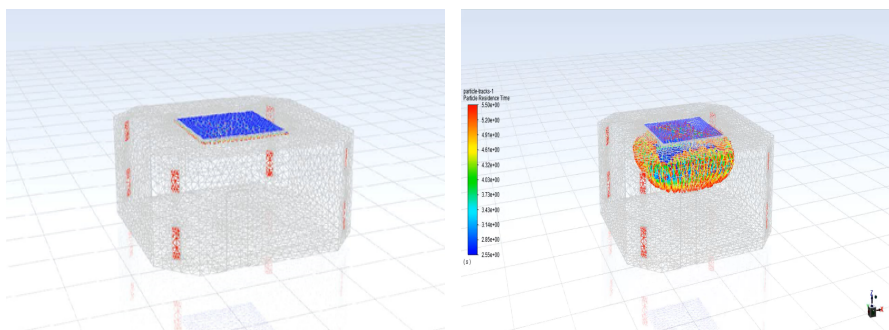


Figure 4.5.1: On the left is the geometry and mesh of the operating room. On the right is represented a transient simulation with particle insertion: inert with two different diameters.

	Size room [m]	Size HVAC [m]	Walls	HVAC walls	Size upper grids[m]	Size bottom grids[m]
Case#2	7x7x3	3x3	aluminum	aluminum	0.6x0.3	0.9x0.3

Table 10: Dimensions of the case 2# chamber.

<b>Case 2#</b>	
<i>HVAC output velocity</i> [m/s]	0.1
<i>Room temperature</i> [K]	300
<i>HVAC outlet temperature</i>	295
<i>Pressure</i> [Pa]	101325

Table 11: Initial and boundary conditions for the chamber and the HVAC case 2#.

#### 4.6 SIMULATION TIMES AND FMU AND ROM MODELS IN TWIN BUILDER

**Calculation times:** The total simulation time was 25s and the time step was 0.05s.

Furthermore, for the stationary simulation, a scheme, see figure 4.6.1, was built in TB in which, as in the first step (case 1#), an FMU model and then the ROM model was inserted. For each ROM model of a variable of interest, tests were carried out by inputting, for the chosen parameters, both constant and time-varying values, obtaining, for each defined time interval, two images of the field, for example, one at the initial time and another at the final time.

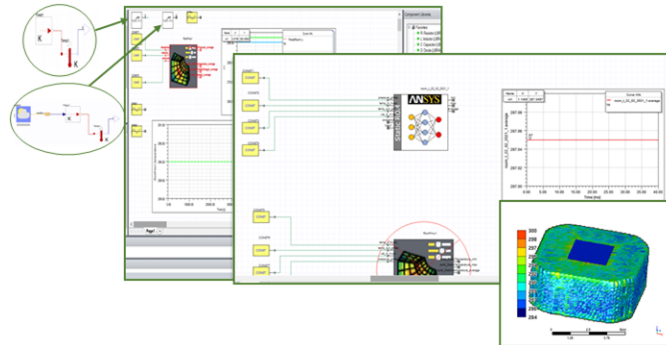


Figure 4.6.1: Twin Builder - FMU model and ROM: results obtained by inserting the ROM or FMU model inside the TB software. The insertion of the input parameter values was highlighted with the circumference and the ellipse.

#### 4.7 SECOND STEP: CASE 3#

The geometry has been discretized with 370k poly-hexa elements, see figure 4.7.1, 900k nodes. It consists not only of the operating room

but also of the addition of a cylinder ( $h = 1.8\text{m}$  and  $r = 0.4\text{m}$ ) which represents an element of the medical staff with a heat flux equal to  $45\text{ W/m}^2$ . The mesh was built with various transitions for the boundary layer.

1. To generate the mesh on the surfaces beyond the definition of the minimum and maximum quantities, a function based on curvature and proximity was used.
2. A method of the **offset** type with uniform transition has been added. This method calculates both the initial local height and the total height using the dimensions of the local element to have a uniform volume variation rate, three layers, and an adjacent element growth rate of change of 0.272. Subsequently, for the regions defined as "fluid", a method has been assigned that controls the proportions of the extruded boundary layer cells, assigning a first cell value equal to 0.5 mm, five layers, and a rate of variation 0.272.
3. On the input and output B.C.s, three layers have been assigned with a transition rate of 1.2 and a growth rate of the **boundary layer** of 1.2
4. In the construction of the volumes, three layers are required for the transitions between the refined and the coarse mesh, and the number of control layers, one between the elements and the geometry, has been specified.

The geometry dimensions have been defined in table 12, and the boundary and initial conditions are summarized in table 13. This simulation converged with a simulation time of approximately 350 steps in 50 minutes with four processors.

**Numerical setting:** The simulations are first-order upwind for the convective term in the momentum, turbulence, and energy equations. The standard  $\kappa$ - $\epsilon$  standard with standard wall function is used for the turbulence. A pseudo transient with values of 1.3s is used.

	Size room [m]	Size HVAC [m]	Walls	HVAC walls	Size upper grids[m]	Size bottom grids[m]
Case#3	7x7x3	3x3	steel	steel	0.6x0.3	0.9x0.3

Table 12: Geometric dimensions of the case 3# operating room.

Figure 4.7.2 shows the trend of the velocity field and of the velocity field vectors, which highlight small recirculation zones.

In figure 4.7.3, the temperature field superimposed on the vectorial one and the temperature trend along a line drawn with respect to the diagonal section of the chamber is shown.

### Case 3#

<i>HVAC output velocity</i> [m/s]	0.3
<i>Room temperature</i> [K]	298.1
<i>HVAC outlet temperature</i>	293.1
<i>Pressure</i> [Pa]	101325

Table 13: Initial and boundary conditions for the chamber and the HVAC case 3#.

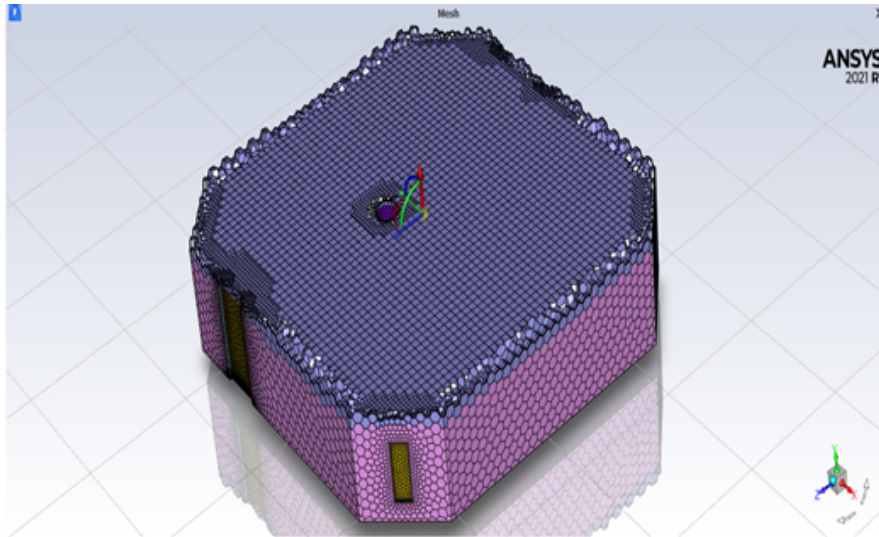


Figure 4.7.1: Operating room geometry discretization: mesh made up of 300k poly-hexa elements.

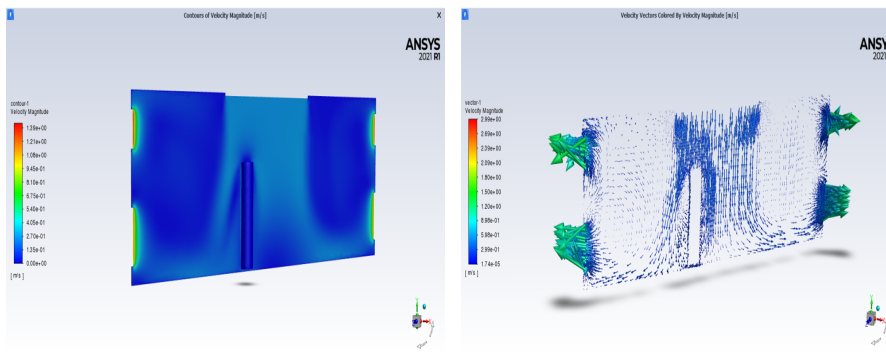


Figure 4.7.2: Left field of velocity. On the right is the velocity vector field.

In figure 4.7.4, zoom along the diagonal section of the chamber and on the transversal plane shows the temperature field present in the chamber and on the cylinder (maximum temperature 311.15K).

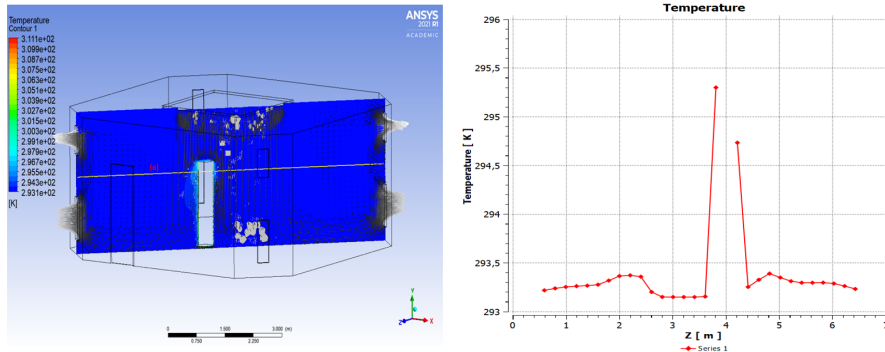


Figure 4.7.3: On the left, temperature field with a superimposed velocity vector field. On the right, the temperature trend in 30 points is extracted along the line on the diagonal section of the chamber.

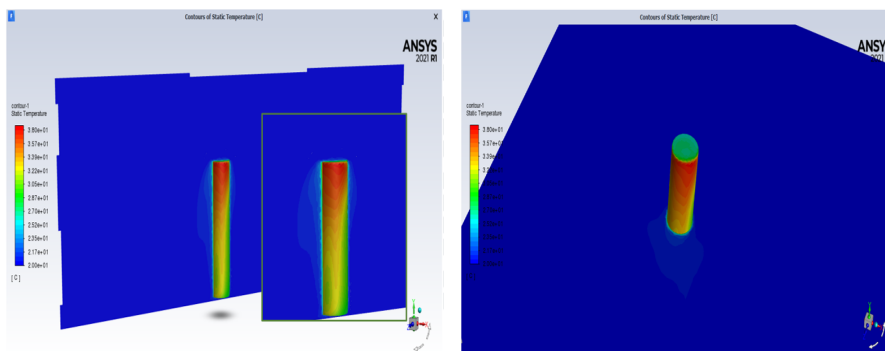


Figure 4.7.4: Temperature field and details according to the diagonal plane and according to an xz plane.

The pressure field, see figure 4.7.5, appears stratified, showing an overpressure in part close to the ceiling. This trend is in agreement with that indicated in Sanchez[79].

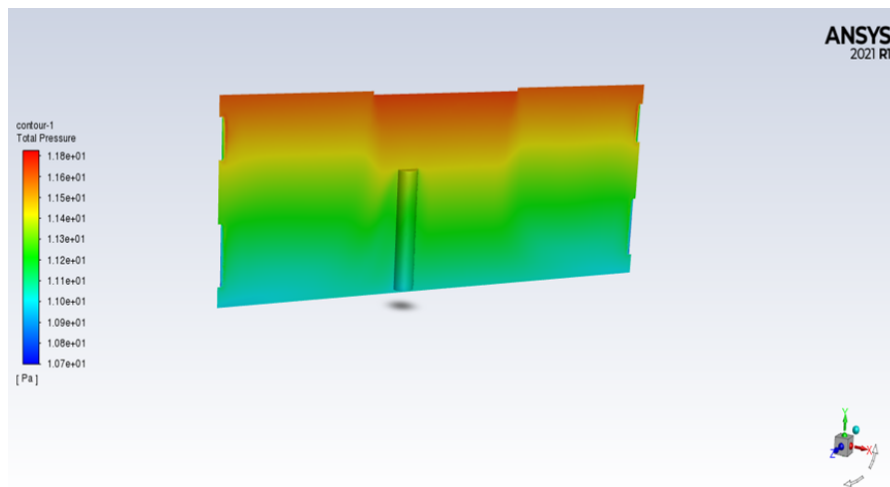


Figure 4.7.5: Trend of the pressure field on the diagonal section of the operating room.

## 4.8 THIRD STEP: CASE 4#

The geometry summarized in the table 14 has been discretized with more than 335k poly-hexa elements, 850k nodes, see figure 4.8.1. It consists not only of the operating room but also of the addition of a cylinder ( $h = 1.8\text{m}$  and  $r = 0.4\text{m}$ ) which represents an element of the medical staff with a heat flux equal to  $45 \text{ W/m}^2$ . The mesh was built with various transitions for the boundary layer.

1. To generate the mesh on the surfaces beyond the definition of the minimum and maximum quantities, a function based on curvature and proximity was used.
2. A method of the **offset** type with uniform transition has been added. This method calculates both the initial local height and the total height using the dimensions of the local element to have a uniform volume variation rate, three layers, and an adjacent element growth rate of change of 0.272. Subsequently, for the regions defined as "fluid", a uniform transition method was assigned with three layers, a rate of variation of 0.272, and development along the walls.
3. On the input and output B.Cs, three layers have been assigned with a transition rate of 1.2 and a growth rate of the **boundary layer** of 1.2
4. In the construction of the volumes, three layers are required for the transitions between the refined and the coarse mesh, and the number of control layers, one between the elements and the geometry, has been specified.

In cases, 3# and 4#, the **buffer layer** specifies the additional number of layers required for the transition between the finer cells of the contour and the sparse cells of the Cartesian mesh is 3. The **peel layer** for controlling the gap between the hexahedral elements and those of the rest of the geometry is 1.

The boundary and initial conditions are summarized in the table 15 This simulation converged with a simulation time of approximately 350 steps in 50 minutes with four processors.

**Numerical setting:** The simulations are first-order upwind for the momentum, turbulence, and energy equations with a pressure-velocity coupling method. The standard  $\kappa$ - $\epsilon$  standard with standard wall function is used for the turbulence. A pseudo transient with values of 1.3s is used.

It is observed in figure 4.8.2 the trend of the velocity field, of the vectors of the velocity field, and the presence of recirculation zones.

	Size room [m]	Size HVAC [m]	Walls	HVAC walls	Size upper grids[m]	Size bottom grids[m]
Case#4	7x7x3	3x3	steel	steel	0.6x0.3	0.9x0.3

Table 14: Geometric dimensions of the case 4# operating room.

### Case 4#

<i>HVAC output velocity [m/s]</i>	0.3
<i>Room temperature [K]</i>	298.1
<i>HVAC outlet temperature</i>	293.1
<i>Pressure [Pa]</i>	101325

Table 15: Initial and boundary conditions for the chamber and the HVAC case 4#.

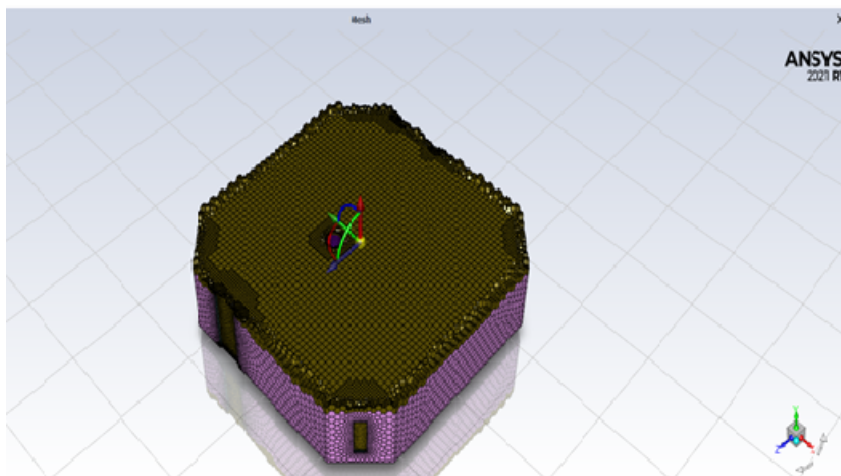


Figure 4.8.1: Operating room geometry discretization: mesh made up of more than 300k poly-hexa elements.

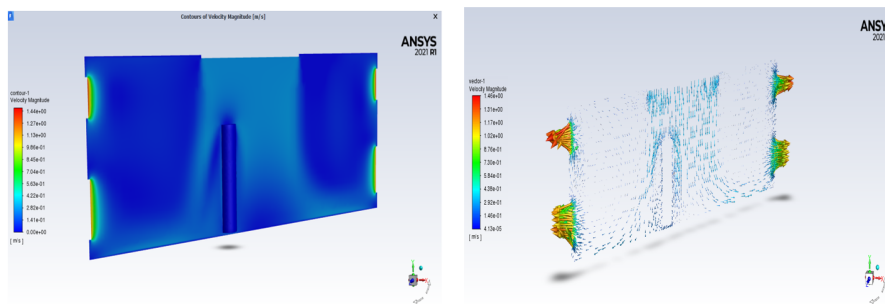


Figure 4.8.2: Left field of velocity. On the right is the velocity vector field.

In figure 4.8.3, the temperature field superimposed on the vectorial field and the temperature trend along a line drawn with respect to the diagonal section of the chamber is shown.

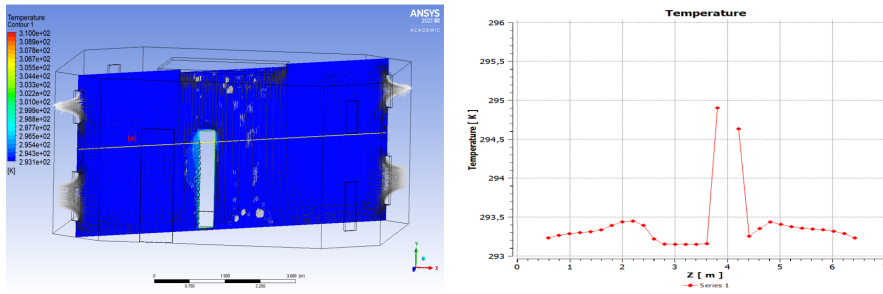


Figure 4.8.3: On the left, temperature field with a superimposed velocity vector field. On the right, the temperature trend in 30 points is extracted along the line on the diagonal section of the chamber.

In figure 4.8.4, zoom along the diagonal section of the chamber and on the transversal plane shows the temperature field present in the chamber and on the cylinder (maximum temperature 310.15K).

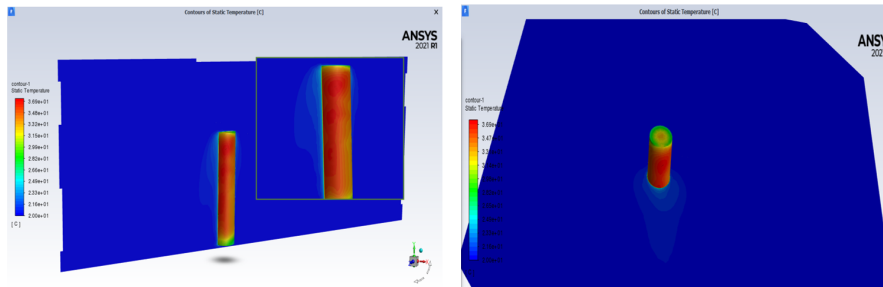


Figure 4.8.4: Temperature field and details according to the diagonal plane and according to an xz plane.

The pressure field, see figure 4.8.5, appears stratified, showing an overpressure in part close to the ceiling. This trend agrees with that found in [79]

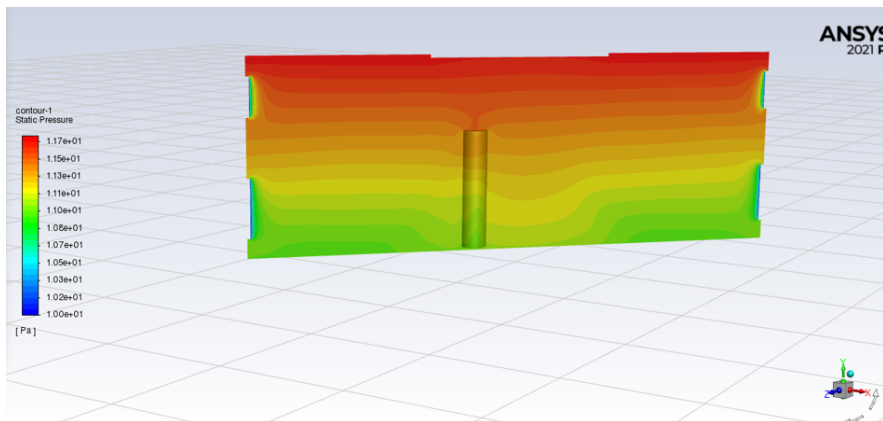


Figure 4.8.5: Trend of the pressure field on the diagonal section of the operating room.

#### 4.9 THIRD STEP: CASE 5#

The geometry, summarized in table 16, has been discretized with about 3 millions poly-hexa elements, see figure 4.9.1. It consists not only of the operating room but also of the addition of a cylinder ( $h = 1.8\text{m}$  and  $r = 0.4\text{m}$ ) which represents an element of the medical staff with a heat flux equal to  $45 \text{ W/m}^2$ . The mesh was built with multiple transitions for the boundary layer:

1. To generate the mesh on the surfaces beyond the minimum and maximum quantities definition, and a function based on curvature and proximity was used.
2. For regions defined as "fluid", a method has been assigned that controls the proportions of the extruded boundary layer cells, assigning a first cell value of  $0.9 \text{ mm}$ , adding ten layers, rate of change  $0.09$ , and development along the walls.
3. On the entrance and exit B.C.s, three layers have been assigned with a transition rate of  $1.2$ , the growth rate of the **boundary layer**, and development along the walls.
4. In the construction of the volumes, a sizing of the cells was chosen (such as the growth rate and the maximum length of the cells) on a region-by-region basis. Four layers are required for the transitions between fine and coarse mesh, and the number of control layer layers, one between the elements and the geometry, has been specified. Corner adjustments have been included to preserve the quality of the mesh of polyhedral elements and a limit to automatically improve the quality of the mesh.

The boundary and initial conditions are summarized in the table 17. This case failed to converge due to problems due to very long simulation times, about seven times slower than cases 3# 4# and about 50 steps in 50 minutes with four processors.

**Numerical setting:** The simulations are first-order upwind for the momentum, turbulence, and energy equations with a pressure-velocity coupling method. The standard  $\kappa\text{-}\epsilon$  with a standard wall function was used for the turbulence. A pseudo transient with values of  $1.3\text{s}$  is used.

	Size room [m]	Size HVAC [m]	Walls	HVAC walls	Size upper grids[m]	Size bottom grids[m]
Case#5	7x7x3	3x3	steel	steel	0.6x0.3	0.9x0.3

Table 16: Geometric dimensions of the case5# operating room.

It is observed in figure 4.9.2 the trend of the velocity field, of the vectors of the velocity field, and the presence of recirculation zones.

### Case 5#

<i>HVAC output speed</i> [m/s]	0.3
<i>Room temperature</i> [K]	298.1
<i>HVAC outlet temperature</i>	293.1
<i>Pressure</i> [Pa]	101325

Table 17: Initial and boundary conditions for the chamber and the HVAC case 5#.

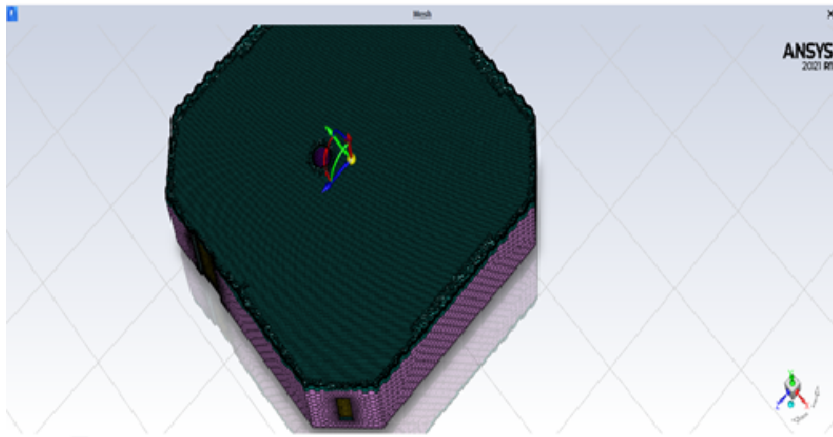


Figure 4.9.1: Operating room geometry discretization: mesh made up of about three millions poly-hexa elements.

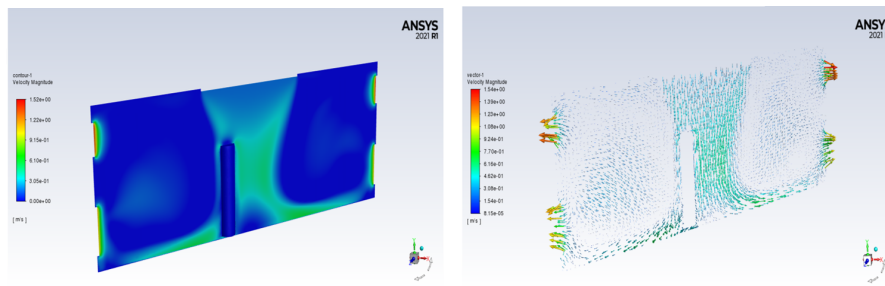


Figure 4.9.2: Left field of velocity. On the right is the velocity vector field.

In figure 4.9.3, the temperature field superimposed on the vectorial field and the temperature trend along a line drawn with respect to the diagonal section of the chamber is shown.

In figure 4.9.4, the temperature field in the chamber and on the cylinder is highlighted with a zoom along the diagonal section of the chamber and the transverse plane.

The pressure field, see figure 4.9.5, appears stratified, showing an overpressure in part close to the ceiling. This trend is in agreement with that indicated in [79].

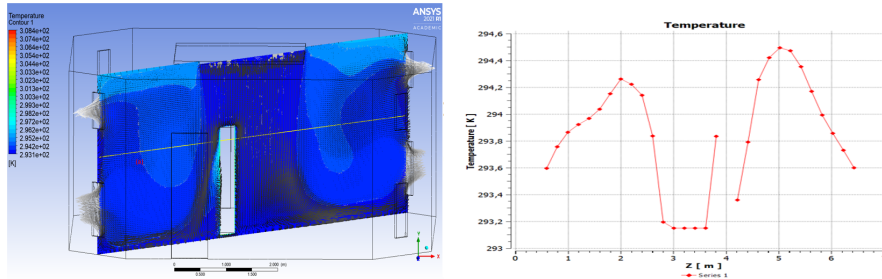


Figure 4.9.3: On the left, temperature field with a superimposed velocity vector field. On the right, the temperature trend in 30 points is extracted along the line on the diagonal section of the chamber.

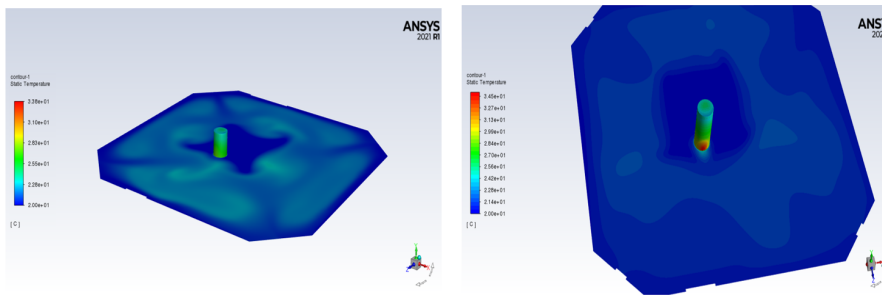


Figure 4.9.4: Temperature field and details according to the diagonal plane and according to an xz plane.

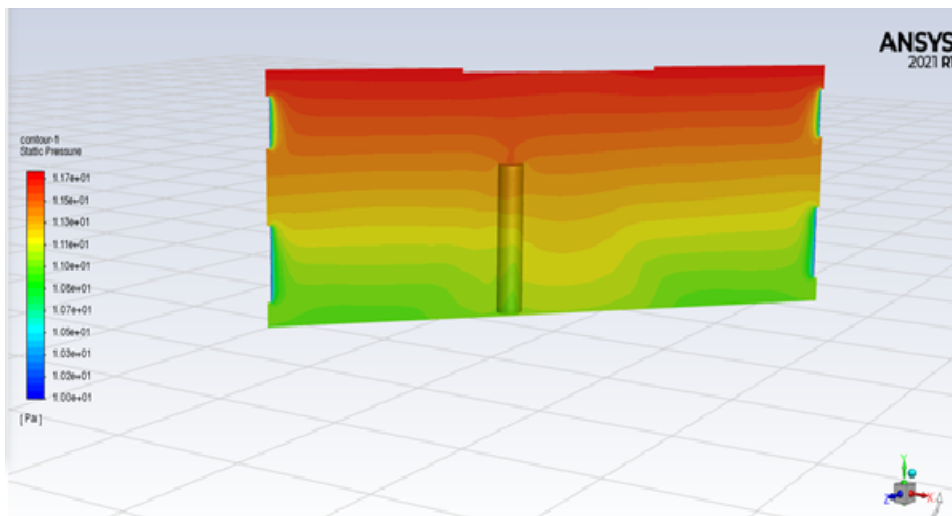


Figure 4.9.5: Trend of the pressure field on the diagonal section of the operating room.

In the figures 4.9.6 and 4.9.7, the temperature trends extracted along the straight line on the diagonal plane of the operating room are compared; the two curves behave in agreement, and the values are similar. In the figure 4.9.6, the temperatures of the cases 3# 4# are compared. In this case the deviation between the values is approximately 0.14% while in the figure 4.9.7 the cases 3# 4# and 5# are compared. Case

5# was added in figure 4.9.6, and the comparison shows a greater deviation, between 0.4 and 0.5%, compared to the values obtained in the previous cases whose simulations were at convergence.

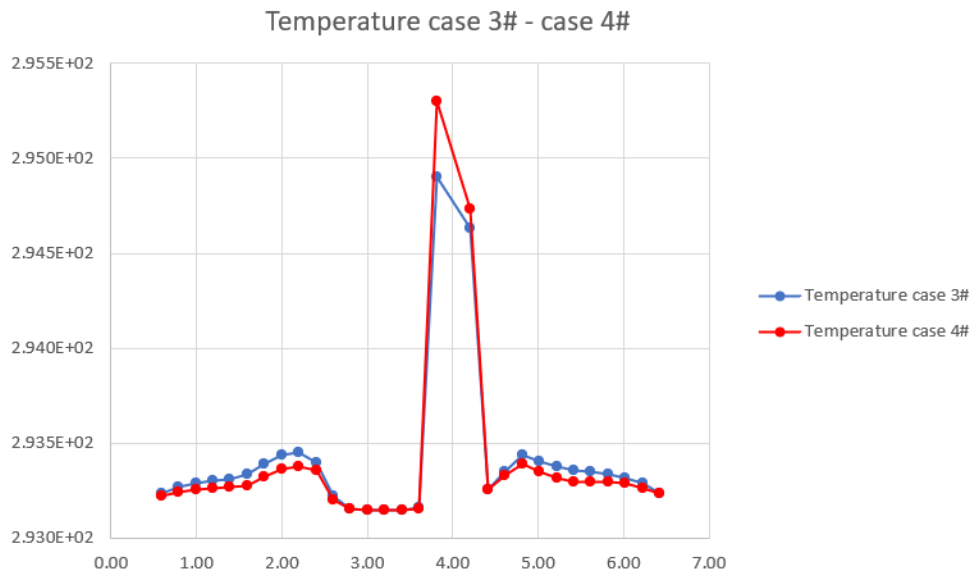


Figure 4.9.6: Comparison between the temperatures obtained in case 3# and case 4#. Diagonal section of the chamber on the straight line (a) with coordinates: P1(0.573879, 1.62396, 6.42445) and P2(6.41105, 1.62396, 0.588).

The following figure, 4.9.8, is a preview of the simulations that are shown in Chapter 6. The cylinder was replaced with a dummy (an element of the medical staff), and the relative humidity and temperature values were reported, as shown in figure 4.9.8. A relative humidity of 50% was considered, and in agreement with the results obtained in Liu et al. [50], the relative humidity is inversely proportional to the temperature. No quantity of CO<sub>2</sub> emitted during respiration was considered in the simulation, but a mole fraction was introduced in subsequent simulations. The simulations do not consider the thermal resistance given by the clothes or the influence of the different elements of the medical staff and the patient.

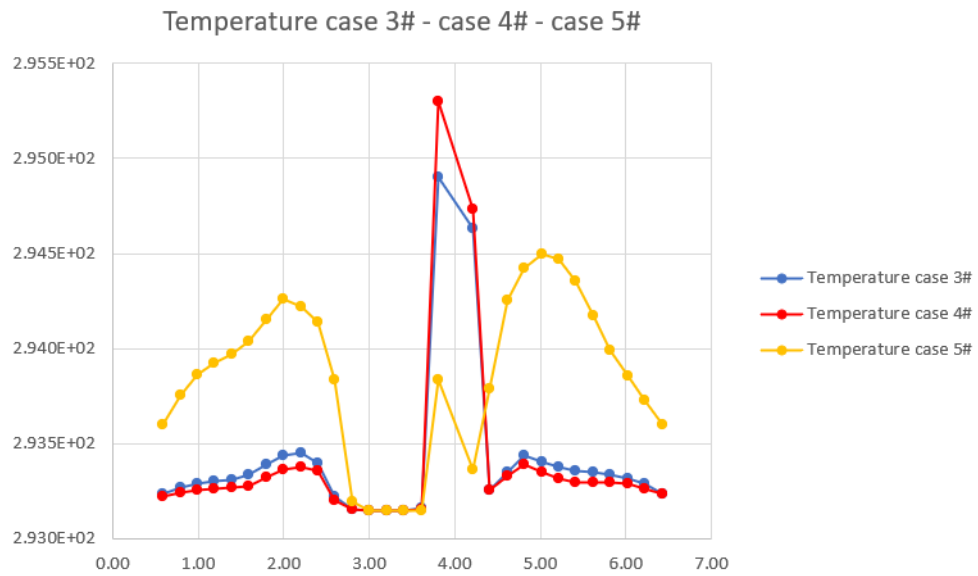


Figure 4.9.7: Comparison between the temperatures obtained in case 3#, case 4# and case 5#. Diagonal section of the chamber on the straight line (a) with coordinates: P1(0.573879, 1.62396, 6.42445) and P2(6.41105, 1.62396, 0.588).

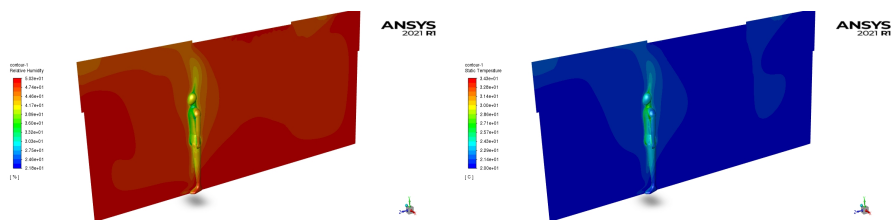


Figure 4.9.8: On the left, the RH field shows the trend for a maximum value of 50%. On the right, the trend of the temperature field in C°.

# 5

---

## EXPERIMENTAL STUDIES

---

### OBJECTIVES OF CHAPTER

This Chapter shows a preliminary study focused on finding the best methodology to conduct the experiments. At this time, the experimental part restarted after two years of interruption and is a work in progress. The small-scale model has been manufactured and linked to the equipment in the last two months. We must choose the better fluid among water, glycerine, or air to perform the experimental setup. We completed the study by means of the CFD analysis to understand the range of values of the variables and decide the better representative fluid to be used in the small-scale model.

### 5.1 THE WORKING FLUIDS: FEATURES

The interpretation of results of the fluid dynamics effects of HVAC in an operating theatre when there is a change in physical scale and when a different fluid (air or water) is adopted can be complicated compared to the results of the effects that there are in a full-scale model. Finlayson et al. [41] work on the diffusion of the pollutant using small scale model, Thatcher et al. [83] investigate the small-scale using water and air and the uranine dye as pollutants. They compared the different fluids and scales using a detailed scaling analysis of a water tank experiment designed to model an ample indoor space. From their calculations, it is possible to predict the effects of molecular diffusion losses, small-scale eddies, turbulent kinetic energy, and turbulent mass diffusivity in a scale model. Studies by, Tang et al., [81], and Araneo et al. [11] are focused on understanding the differences in the use of a different fluid from the air in a model scaled (small-scale). An interesting investigation is presented by Poussou et al. [70], and Mazumdar et al. [56], where is considered the relevance to the equivalence of the numbers of air change is given. It is considered significant to prevent high virus concentrations in the indoor environment, and a possible strategy considers evaluating the number of air changes compatible with the conditions of kinematic, fluid dynamics, and

dynamic similitudes. In this case, we consider it relevant to maintain the number of air changes among the small-scale and full-scale. Table 18 compared the water, air, and glycerine to decide which fluid we will be used for the experiments. The use of air should be the best choice, very similar to reality, but the problem, in this case, is the simulation with particles that can be made of dangerous materials. For this reason, we also consider the possibility of using other fluids in particular fluids in the liquid phase. The liquids evaluated are water and glycerine; the Reynolds numbers and Euler numbers are compared in table 19 to understand the velocity and the pressure to give to the scale model.

Elements	Element Properties							
	Temp <sub>min</sub> [K]	Temp <sub>max</sub> [K]	$\rho_{min}$ [Kg/m <sup>3</sup> ]	$\rho_{max}$ [Kg/m <sup>3</sup> ]	$\mu_{min}$ [Pa/s]	$\mu_{max}$ [Pa/s]	$\nu_{min}$ [N/s]	$\nu_{max}$ [N/s]
N <sub>2</sub>	18	30	1.1729	1.1263	1.75E-05	1.80E-05	1.49E-05	1.80E-05
H <sub>2</sub> O	18	30	998.6	995.65	1.05E-03	7.97E-04	1.05418E-06	7.97E-04
Glycerine	19.9	30	1261.53	1254.86	1.4	0.51	1.11E-03	0.51

Table 18: Comparison between water, air, and glycerine

We consider nitrogen in place of air due to the high quantity of this element in the air composition (78% nitrogen, 20.95% oxygen, 0.93% argon, 0.041% Carbon dioxide, and other gases), and in table 19, we analyze the two fluids in detail.

Elements	Element dimentions								
	L <sub>tot</sub> [m]	L <sub>min</sub> [m]	Re <sub>crdmin</sub> L <sub>tot</sub>	Re <sub>crdmin</sub> L <sub>min</sub>	Re <sub>crdmax</sub> L <sub>min</sub>	Eu <sub>min</sub>	Eu <sub>max</sub>	velox <sub>min</sub> [m/s]	velox <sub>max</sub> [m/s]
N <sub>2</sub>	2.6	0.521	1.68E+04	3.50E+02	1.75E+03	8.64E+06	3.46E+05	0.1	0.5
H <sub>2</sub> O	2.6	0.521	2.37E+05	4.94E+03	2.47E+04	1.01E+04	4.06E+02	0.072	0.35

Table 19: Comparison between water and air (N<sub>2</sub>)

Figures 5.1.1 show the compressibility of nitrogen and water in terms of the Z factor in the gas phase, and in table 20, the critical values are shown. The Z factor for an ideal gas is evaluated in equation 5.1.1, in figure 5.1.1 line green, and for real gases, we have chosen the Van der Waals equation, 5.1.2. The Mach number is evaluate for different temperature in relations 5.1.3, 5.1.5, 5.1.5, and 5.1.6.

$$Z = \frac{p}{\rho RT} \quad (5.1.1)$$

Element	T <sub>c</sub> [K]	P <sub>c</sub> [atm]
N <sub>2</sub>	126.20	33.98
H <sub>2</sub> O	373.94	220.64

Table 20: Critical values of N<sub>2</sub> and water

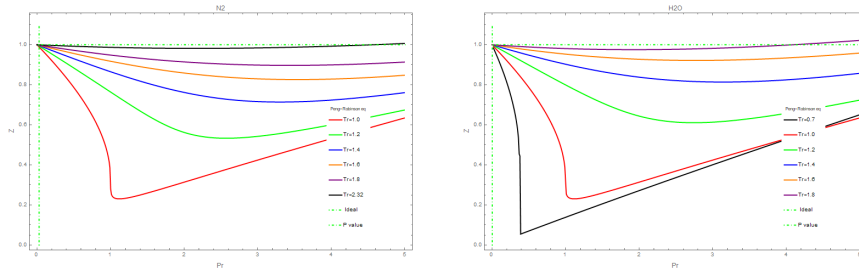


Figure 5.1.1: The Z compressibility factors in the gas phase are shown on the left and right.

$$P = \frac{RT}{V - b} - \frac{a}{(V + b)} \quad (5.1.2)$$

The Mach number for different temperatures are:

$$v_{N_2}/a_{N_2}(T = 293.15K) = 0.1/340[m/s] = 2.9 * 10^{-4} \quad (5.1.3)$$

$$v_{N_2}/a_{N_2}(T = 298.15K) = 0.1/352[m/s] = 2.8 * 10^{-4} \quad (5.1.4)$$

$$v_{H_2O}/a_{H_2O}(T = 293.15K) = 0.1/1100[m/s] = 1.0 * 10^{-4} \quad (5.1.5)$$

$$v_{H_2O}/a_{H_2O}(T = 298.15K) = 0.1/1482[m/s] = 6.7 * 10^{-5} \quad (5.1.6)$$

In the last table 21, we present a comparison between the number of air changes between air and water to verify the possibility of reproducing the correct volumetric mass flow. The quantity of water volume indispensable for experiments need to be calculated with the disponibility of pumps and tanks to inflate the flow rate.

Elements	Vol <sub>cf<sub>d</sub></sub>	L <sub>cf<sub>d</sub></sub>	J[m <sup>3</sup> /s]	l/min	ACH
Air	147	6.25E + 00	6.25E-01	3.75E+04	1.53E+01
H <sub>2</sub> O	0.147	6.25E - 02	6.25E-04	3.7E+01	1.53E+01

Table 21: Number of air changes per hour

	H <sub>2</sub> O	Air
Pressure [Pa]	1280	2.6
Velocity [K]	0.072	0.1
Pseudo time step	0.13	1.3

Table 22: Pressure, velocity, pseudo time step set-up

The fluid chosen for experimental tests is water. To understand the behavior of the water in a small-scale model and test the suitable experiment setup, we ran the CFD simulations. The CFD simulations consist of a small-scale model of the operating theatre, and the fluid considered is water. Table 22, table 23, and 24 report the B.Cs. A simulation (see table 22) with the fluid dynamic similarity (Re number) and the dynamic similarity (Eu number) is realized, while the other simulations consider only the fluid dynamic similarity (Re number). The pseudo time step was chosen in a simulation equal for both fluids (see table 23), air (N<sub>2</sub>) and water, and in other simulations, was chosen proportional similar to kinematic similarity, as studied by Araneo et al. [11] Mazumdar et al. [56]. Figure 5.1.2 illustrates the field of pressure in the case of Re similarity is respected, see table 22. The pressure is homogenous and very high in the cases of water. The velocity field shown in figures 5.1.3 is similar for the water and air, and the order of magnitude is the same. In this simulation, fluid dynamic and dynamic similarity are used. The time similarity is not wholly correct.

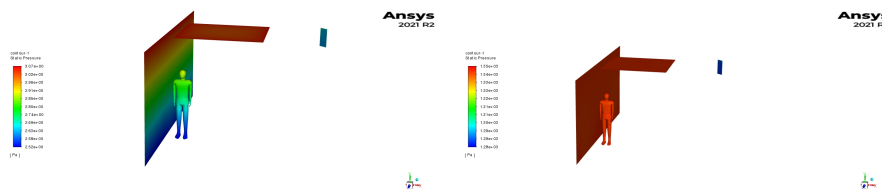


Figure 5.1.2: The pressure field of air and water are shown on the left and right.

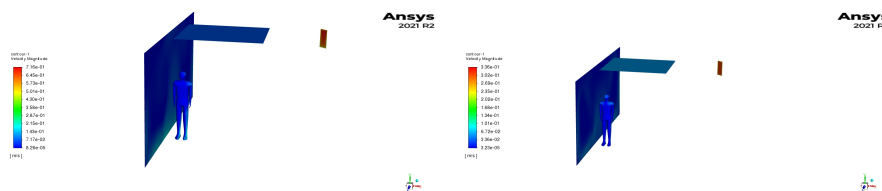


Figure 5.1.3: The velocity field of air and water are shown on the left and right.

Figure 5.1.4 illustrates the field of pressure in the case of Re similarity is not respected, see table 23. The pressure is homogenous in the case of water, and the orders of magnitude are comparable. The veloc-

	H <sub>2</sub> O	Air
Pressure [Pa]	2.6	2.6
Velocity [K]	0.01	0.1
Pseudo time step	1.3	1.3

Table 23: Pressure, velocity, pseudo time step set-up

ity field shown in figures 5.1.5 is similar to the water and the air in the order of magnitude. The fluid dynamic similarity, dynamic similarity, and time proportionality are not respected in these simulations.

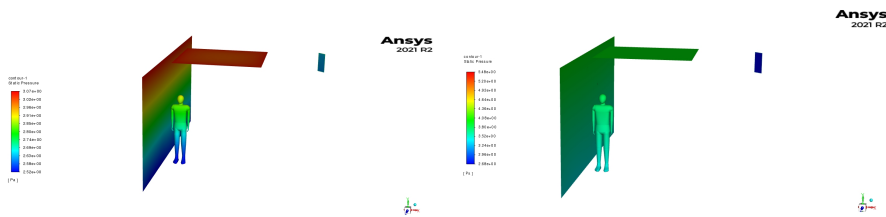


Figure 5.1.4: The pressure field of air and water are shown on the left and right.

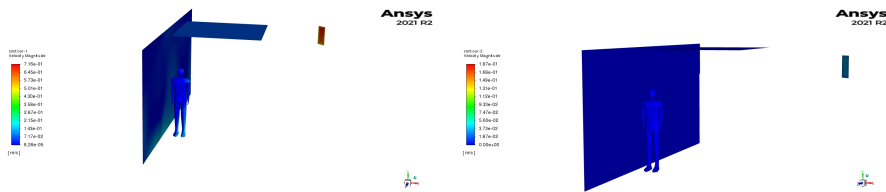


Figure 5.1.5: The velocity field of air and water are shown on the left and right.

Figure 5.1.6 illustrates the field of pressure in the case of Re similarity is not respected, see table 24. The pressure is homogenous in the case of water, and the orders of magnitude are comparable. The velocity field shown in figures 5.1.7 is more homogenous in the water than in the air. The order of magnitude is similar to air and water. This simulation does not respect fluid dynamic, dynamic similarity, and time proportionality. The velocity field is shown in figures 5.1.7

In Appendix A is shown the relation between the volumetric flow, ACH for the water (small scale) and the air (full scale)

## 5.2 TEST EQUIPMENT

The first step is the qualitative analysis. The scale model is in plexiglass material. The experiment consists of determining the motions of the particles, and for this reason, is used an orthogonal laser to the lateral

	H <sub>2</sub> O	Air
Pressure [Pa]	2.6	2.6
Velocity [K]	0.01	0.1
Pseudo time step	0.13	1.3

Table 24: Pressure, velocity, pseudo time step set-up

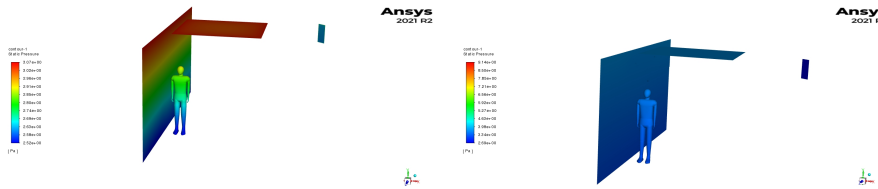


Figure 5.1.6: The pressure field of air and water are shown on the left and right.

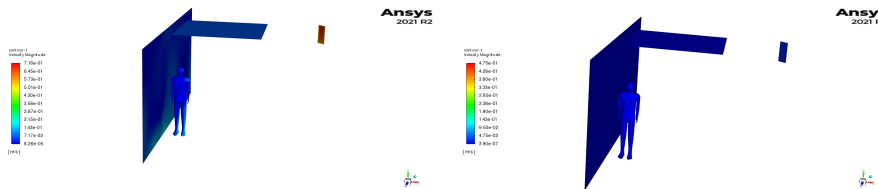


Figure 5.1.7: The velocity field of air and water are shown on the left and right.

surface of the scale model plane to identify the fluorescent particles made of silicone and take a video with a camera orthogonal to the laser. The camera resolution is essential to have a correct resolution, particularly for the second step, which consists of the quantitative investigation with the PIV (a non-intrusive optical measurement technique), see, for instance, Raffel et al. [71], Westerweel et al. [2], and Ferrara [40], e.g., as the investigations of the flow field associated with prosthetic heart valves studied by Balducci et al. [14], D'Avenio et al. [30], that requires precision or the flow field in the total cavopulmonary connection, published by Grigioni et al. [43]. The camera needs calibration before use for the measurements. The calibration is done with a sheet with white points to define the error in the resolution. We highlight that using only one fluid, water, not two (the water and the air), helps reduce the refraction between the materials.

The scale model is composed by:

- a plexiglass box, see figure 5.2.1 within green a bulkhead to control and stabilize the water level (in red ellipse)
- a scale model (1:10) of an operating theatre, see figure 5.2.2 item external equipment for the water circuit

Figure 5.2.3 illustrates the design of the mock-up scale model built.

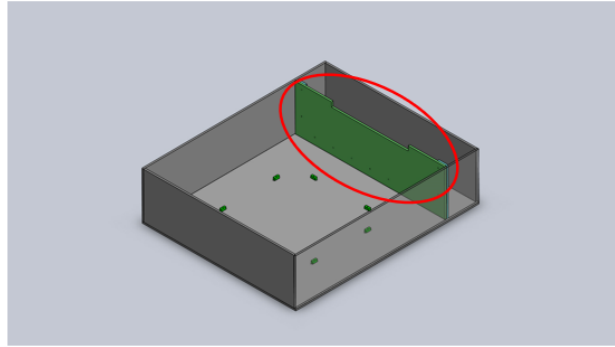


Figure 5.2.1: The figure shows the box model

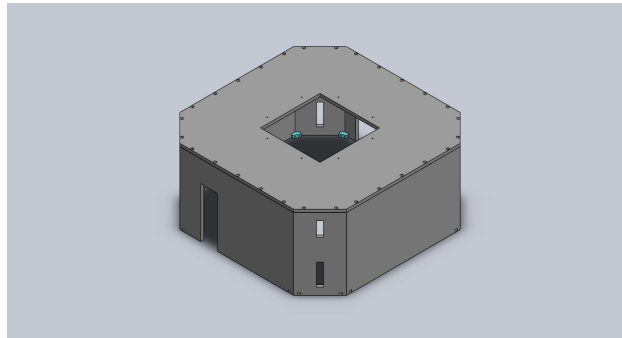


Figure 5.2.2: The figure shows the scale model of the operating theatre

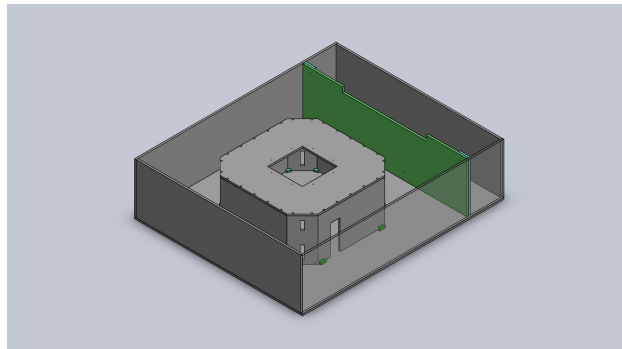


Figure 5.2.3: The figure shows the whole scale model

The equipment of experiments is illustrated in figure 5.2.4, which shows a calming baffle to laminarize the injected flow. The idea is to reproduce the CFD experiment using a scale model (1:10). The model is made of several parts and should give a laminar or like-laminar flow. For this reason, the HVAC is built with 1800 straws to laminarize the flow that comes from the tank. The path of flow is shown in the sequence of figures 5.2.5, 5.2.6, and 5.2.7.

We start from figure 5.2.5 1, where there are three water containers and the pump that supplies the tank, see figure 5.2.5 (2), located on

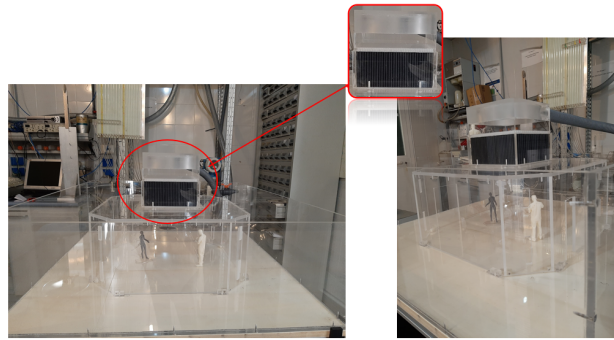


Figure 5.2.4: In the figure is shown the mock-up made of the plexiglass material of the operating theatre. A zoom on the calming baffle is realized



Figure 5.2.5: The figure shows to the left the scale model and three basins used to fill up the tank or to empty it, and to the right, the tank where is highlighted the maximum level of water called "overfull".



Figure 5.2.6: In the figure to the left is shown the pressure gauge; to the right at the top is shown the electromagnetic flowmeter, and at the bottom, the flowmeter that will be linked to the scale model.

top. The tank is divided into three septums to dampen the water oscillations when the water is pumped inside. The last septum is higher than others and is essential to manage the water pressure and

level (the red circle). The next step is the supply of water to the model. Before the arrival of water in the scale model, the water path goes is:

- the water start from the basin, see figure 5.2.5 (1)
- the water fills up the tank, see figure 5.2.5 (2),
- the water passes through the measurement device, see figure 5.2.6 (3), where the gauge measures the pressure that is shown in figure 5.2.6 (4)
- after the passage in the electromagnetic flowmeter (precision 1:1000), the water arrives at the operating theatre

The last step, see figure 5.2.7 (7), uses the laser to show the particle tracks on a plain. At the end of the experiment, the scale model is emptied by the holes in the small part of the box containing the model and divided from the room model by a bulkhead, see figure 5.2.7 (6), and the water goes again into the tree swimming pool. The tank manages 45l/min, and the whole system is around 500 kg the water. The particles that will be used are fluorescent particles made of silicone, and it will be essential to get them back.

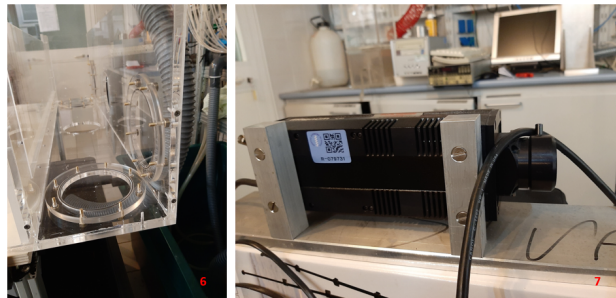


Figure 5.2.7: In the figure is shown the laser.

# 6

---

## RESULTS

---

### CHAPTER OBJECTIVES

In this Chapter, the CFD simulations consider the operating theatre with a member of the medical staff inside, initially represented with a cylinder, case 6a#, and after with a human dummy, case 6b# and case 6c#. In particular, the simplified case 6a# considers a cylinder (as the case 5# in Chapter 4), to mimic the human, and a reduced number of variables to set-up the ROM. After that, two simulations with a human dummy are presented, together with the relative ROMs comparison.

### 6.1 NUMERICAL RESULTS

The numerical results are divided into CFD results and ROM results. After the ROM construction, the TB is made.

### 6.2 CFD RESULTS

#### 6.2.1 CFD: Case 6a# and 6b#

The operating theatre takes as a reference, the geometry details are indicated in the table 25, is similar to that of Monza Hospital. The geometry, see figure 6.2.1, has a surface area of  $49 \text{ m}^2$ , ( $7\text{m} \times 7\text{m}$ ), a height of 3m and eight discharge grilles, four upper and four lower, respectively of dimensions ( $0.6\text{m} \times 0.3\text{m}$ ) and ( $0.9\text{m} \times 0.3\text{m}$ ) as reported in Di Sanctis [31]. The central ventilation system consists of a single grid from which the air is introduced with a uniform velocity and has dimensions  $2.6\text{m} \times 2.6\text{m}$  (case 6b#, and case 6c#) and  $3\text{m} \times 3\text{m}$  (case 6a#).

**Case 6a#:** The geometry with the cylinder inside, summarized in table 25, was discretized with one million poly-hexa elements, see figure 6.2.2, 1.7 million nodes, and we have more transitions for the boundary layer:

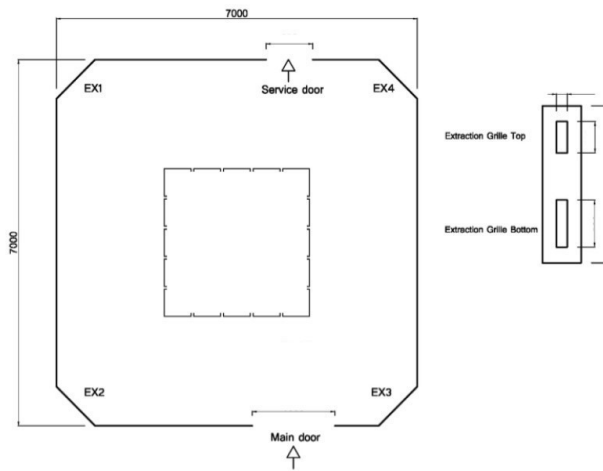


Figure 6.2.1: Geometry of the operating room. Reprinted from Romano et al. [73]

1. On the B.C of the cylinder, a local control on the curvature was given for the construction of the mesh on the surfaces.
  2. A method of the **offset** type with a uniform transition was added. This method calculates both the initial local height and the total height using the dimensions of the local element to have a uniform volume variation rate, three layers, and an adjacent element growth rate of change of 0.272. Subsequently, for the regions defined as "fluid", a method was assigned to control the proportions of the extruded boundary layer cells, assigning a first cell value equal to 0.68 mm and ten layers for the transition with the rate of change 0.272.
  3. In the construction of the volumes, eight layers are required for the transitions between the refined and coarse mesh.
- In table 26 are reported the initial conditions.

	Size room [m]	Size HVAC [m]	Walls	HVAC walls	Size upper grids[m]	Size bottom grids[m]
Case#6a	7x7x3	3x3	steel	steel	0.6x0.3	0.9x0.3

Table 25: Geometric dimensions of the case operating room: case 6a#.

#### Case 6a #

<i>Room temperature</i> [K]	298.15
<i>Chamber pressure</i> [Pa]	101325

Table 26: Initial conditions for the room and the case HVAC case 6a#.

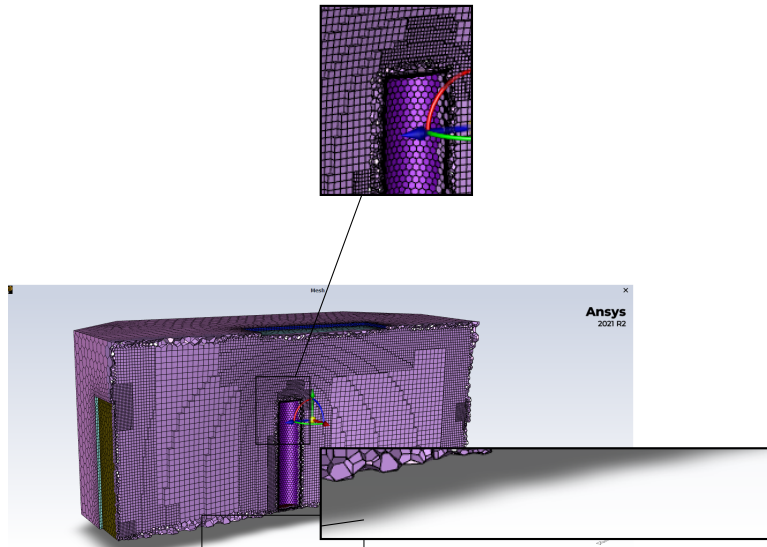


Figure 6.2.2: Detail of the mesh of the operating room and the cylinder.

**Case 6b#:** The geometry summarized in table 30, containing the case with the human dummy, was discretized with 2.4 million poly elements -hexa, 3.7 million nodes, and more boundary layer transitions, see figure 6.2.3, and figure 6.2.4:

1. On the B.C, legs, and arms (defined as "wall"), of the human dummy, for the construction of the mesh on the surfaces, control was given on the size of the faces.
2. A method of the **offset** type with a uniform transition was added. This method calculates both the initial local height and the total height using the dimensions of the local element to have a uniform volume variation rate, three layers, and an adjacent element growth rate of change of 0.272. Subsequently, for the regions defined as "fluid", a method was assigned which controls the proportions of the extruded boundary layer cells, assigning a first cell value equal to 0.68 mm, five layers, and a rate of variation 0.272.
3. In the construction of the volumes, eight layers are required for the transitions between the refined and coarse mesh.

In table 27 are reported the initial conditions.

**Case 6a#:** The geometry with the cylinder inside, summarized in table 25, was discretized with one mil poly-hexa elements, see figure 6.2.2, 1.7 mil nodes, and we have more transitions for the boundary layer.

### Case 6b #

Room temperature [K]	298.15
Chamber pressure [Pa]	101325

Table 27: Initial conditions for the room and for the case HVAC case 6b#.

**Numerical setting:** A numerical approach, like the previous cases, RANS and a PBS solver, were chosen for the simulations of cases 6a# and 6b#.

Both simulations are first-order upwind discretized for the convective term in the equations of momentum, turbulence, and energy; in addition, a pressure-velocity coupling method was used, and for the turbulence, a standard  $\kappa$ - $\epsilon$  with a wall function to describe the behavior of the fluid to the wall. A pseudo transient is used with a value of 1.3s.

In the first simulation (case 6a#), a cylinder ( $h = 1.8\text{m}$  and  $r = 0.4\text{m}$ ) was used as an element of the medical staff. The power given to the cylinder was 131.9 W, according to Balocco et al. [16], the heat flow of  $53\text{ W/m}^2$  was obtained consequently. After, the cylinder was replaced by a human dummy, whose details of the geometry and mesh are visible and zoomed in figure 6.2.4. In this case, a power 117.0 W was given and, therefore, a heat flux equal to  $53.25\text{ W/m}^2$ , as used in Di Santis [31], and Balocco [16]. This value is similar to the value obtained from the use of the *Formula of Du Bois* (Du Bois [37]), was established in ASHRAE [13]. Haddad et al. reported it in their study, [44], on the metabolic rate estimation in the calculation of the PMV of thermal sensation for children, where 1 MET is the metabolic heat production rate of a person ( $1\text{ MET} = 50\text{ kcal/ (h.m}^2) = 58.15\text{W/m}^2$ ). The initial and boundary conditions of the case are reported in the tables 26 and 27.

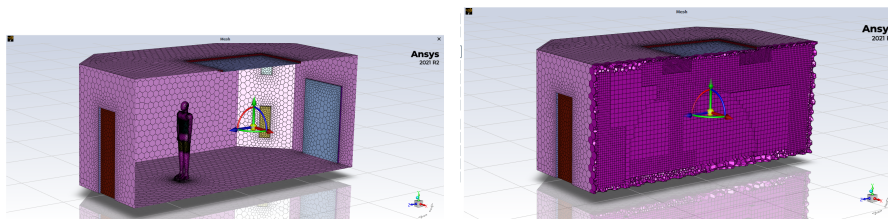


Figure 6.2.3: The mesh of the operating room and the human dummy inside according to the YZ plane is shown on the left and right.

### 6.3 ROM RESULTS

For the construction of the ROM of cases #6a and #6b, 15 simulations were carried out using 15 combinations of parameters whose variations

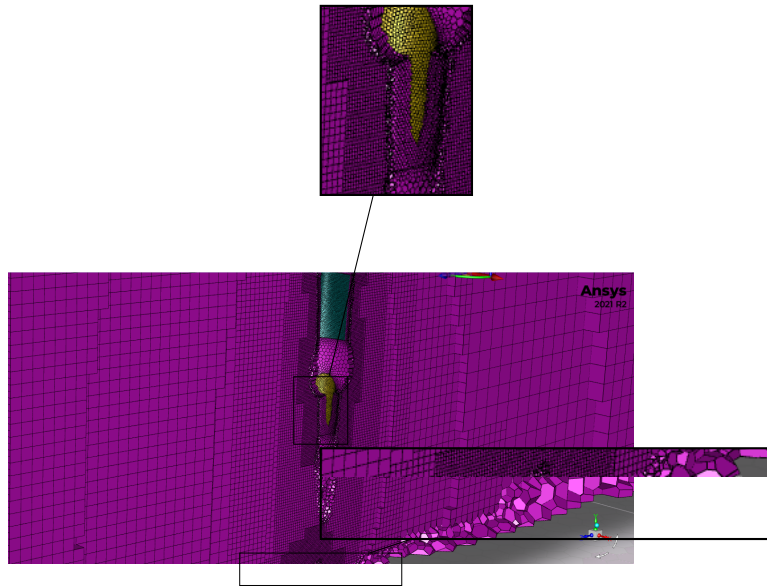


Figure 6.2.4: Detail of the mesh of the operating room and the human dummy.

occur in the interval indicated in table 28 for case 6a# and in the table 29, for case 6b#.

Parameter	Min value	Max value
Velocity [m/s]	0.1	0.34
Temperature [K]	290.0	297.5
$\Delta$ Pressure [Pa]	5.2	14.0
Fraction Molar H <sub>2</sub> O	0.01	0.012
Position cylinder [m]	0.14	1.0

Table 28: Range of variation of the case input parameters case 6a#.

### 6.3.1 ROM: case 6a# and case 6b#

In figure 6.3.1, the ROM of the temperature field of the case 6a# is shown. This ROM considers a few parameters, in particular, 4 that implies, as written in Chapter 3, section 3.2.2 that the number of the simulations is at least 32; in this case, used as test the number of simulations (snapshots) is 15. In table 28, the value range for the case6a# is shown. In case 6a#, the simulations used to obtain the field by snapshots that constitute the two sets, the learning set and the validation set for the construction of the ROM, did not converge. In particular, for case 6a#, the time for each simulation was 18 minutes, about 45s per step, for 20 steps.

Parameter	Min value	Max value
Velocity [m/s]	0.1	0.5
Temperature [K]	291.15	310.15
$\Delta$ Pressure [Pa]	2.0	8.0
Molar Fraction H <sub>2</sub> O	0.01	0.031
Position human dummy [m]	-1.0	1.0

Table 29: Range of variation of the input parameters: case 6b#.

We use this setup of the simulation (case 6a#) to recalibrate the setup for the following simulations.

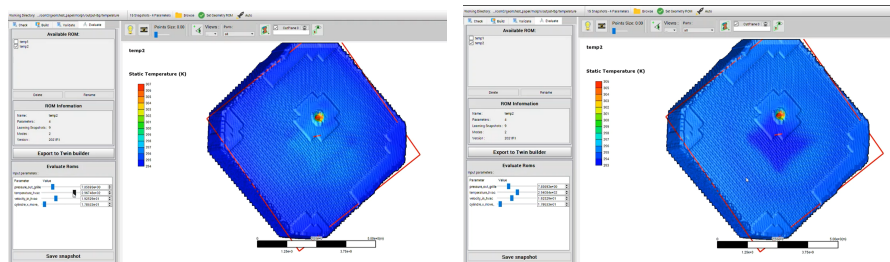


Figure 6.3.1: The values of the temperature field relating to two different values of the parameter of temperature are shown on the left and right: case 6a#

In table 29, the value range of the parameters in case 6b# is shown, and figure 6.3.2 shows the ROM built for case 6b#.

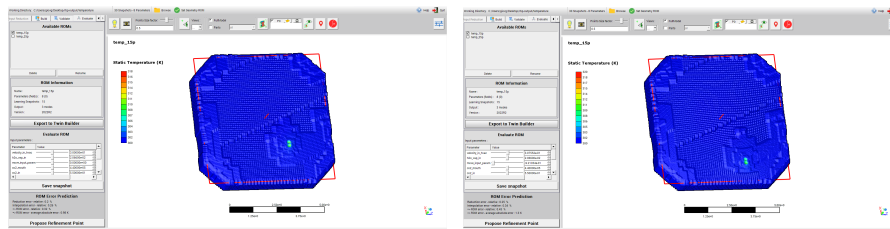


Figure 6.3.2: The values of the temperature field relating to two different values of the parameter of position are shown on the left and right: case 6b#

#### 6.4 CASE STUDY: CASE 6C# FROM CFD TO DT

The operating theatre geometry is similar to the Monza Hospital, see figures 6.2.1, 6.4.1, and the differences are highlighted in previous cases. We remember that the original operating theatre has an HVAC system and several blocks of HEPA filters that supply the air with different velocities according to the position of the blocks. In this analysis, a geometry similar to the reference one was reproduced, except

for the HVAC. In this case, the HVAC system has a surface of 3m x 3m with a real area of the inlet flow equal to 2.6m x 2.6m, see table 30. From the filter, the air is injected with a uniform velocity; only in a preliminary phase was it entered the same mass flow present in Di Sanctis [31]. This is because the velocity was used among the parameters of interest chosen for constructing the ROM. Consequently, there will be a variation of the flow rate  $\dot{m}$ , affecting the number of ACH, which will vary. The ACH is shown in equation 6.4.1, see Appendix A as evaluated in Romano et al. [73]:

$$ACH = \frac{\left(\frac{\dot{m}}{\rho}\right)}{Vol_{room}} * 3600 \quad (6.4.1)$$

with 3600 seconds.

The chamber is under overpressure to avoid contamination from the outside environments, and a mixture made of air and water vapor is considered to evaluate the RH. The case study was based on the

	Size room [m]	Size HVAC [m]	Walls	HVAC walls	Size upper grids[m]	Size bottom grids[m]
Case studio	7x7x3	2.6x2.6	steel	steel	0.6x0.3	0.9x0.3

Table 30: Geometric dimensions of the operating room: case6b# and case6c#.

a creare la quota. Fare clic tenendo premuto Ctrl su due oggetti per creare un punto o una linea virtuale.

Ansys  
2021 R2

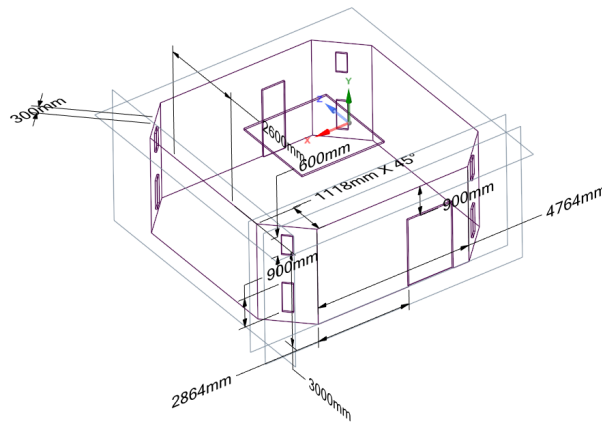


Figure 6.4.1: Geometry of the operating room.

simulations of simpler cases, which allowed the optimization of the settings for the CFD. A simplified geometry was created consisting of a chamber with a cylinder inside to represent the medical staff

involved in the operation (case 6a#). Thanks to this simplification, it was possible to evaluate both the influence of the mesh for calculating the heat flux produced and, consequently, the temperature of the elements of the medical staff. In addition, it was possible to carry out the first tests to obtain a ROM in which it was also possible to vary the position of the medical staff through the introduction of a geometric parameter that defines the displacement that was simulated through the Fluent RBF-Morph add-on (case 6b #), RBF for Fluent [21]. Now we implement case 6b#, and by CFD simulations carried out on case 6c #, we obtain the ROM and, subsequently, the digital twin. In diagram 6.4.2 is shown a workflow:

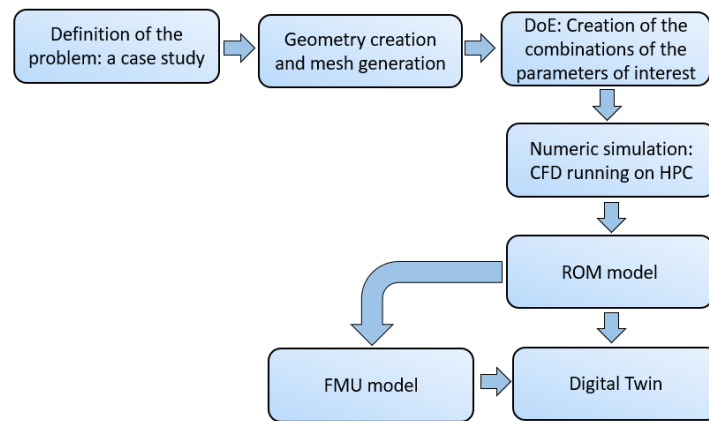


Figure 6.4.2: Diagram of the workflow used.

The numerical set-up is similar to the previous cases simulated: the RANS approach and a PBS solver. The simulations performed are first-order upwind discretized for the convective term in the equations of momentum, turbulence, and energy with a method of coupling between pressure and velocity and second-order for the species. The turbulence is a standard  $\kappa$ - $\epsilon$  with a standard wall function to approximate the turbulence behavior at the wall. Similar to other cases, a pseudo time step to 1.3s is used.

The material was created, called "human", with the characteristics of density, conduction, and specific heat typical of the human body as defined in Balocco et al. [16].

**Boundary and initial conditions:** the analyzed case has foreseen as boundary conditions: a uniform velocity at the input and a pressure at the output. The material defined as "human" was used with the characteristics of density, conduction, and specific heat typical of the human body as defined in Balocco et al. [16] and Pasquarella et al. [65], and Liu et al. [50].

The mannequin with human features used to reproduce an element of the medical staff, whose geometry and mesh details are visible in figure 6.4.4, has the same characteristics as that dummy of case 6b#. Power equal to 117.0 W was given on the dummy to obtain a heat flux equal to  $53.25 \text{ W/m}^2$ , as studied by Di Santis [31], Balocco et al. [16], Massarotti et al. [55], Romano et al. [73], and in the study by Neil et al., [58]. From the heat flow, it will be possible to obtain the temperature present on the human dummy; in this calculation, the thermal resistance given by the clothes and the influence of the different elements of the medical staff and the patient were neglected.

The initial and boundary conditions of the case analyzed are reported in the tables 31 and 32. In table 32 is reported the mole fraction of  $\text{H}_2\text{O}$  just as evaluated in Appendix B.

Furthermore, the parameters of RH (in terms of mole fraction of water vapor) and the mole fraction of  $\text{CO}_2$  emitted during the exhalation phase during respiration, equal to 80 l/h as defined in Balocco et al. [15], and Cheng et al. [28], are considered (in the Appendix C is evaluated the mass flow used as B.C input.). The presence of  $\text{CO}_2$  in the operating theatre was studied in the work of Pereira et al. [68], and also in Nowak et al. [60], Villafruela et al. [88],  $\text{CO}_2$  presence in environment has been studied. Butt et al. [26], consider the  $\text{CO}_2$  exhaled during the breath as a tracer to highlight the contaminant particles and airborne in the room, and for this reason, we include the  $\text{CO}_2$  as a boundary condition in term of mass flow .

The geometry was discretized with 3.3 million poly-hexa elements and 5.7 million nodes, see figure 6.4.3. There are more transitions for the boundary layer with different levels of refinement both on the wall and with respect to the human dummy, as shown in figures 6.4.3 and 6.4.4:

1. On the B.C, legs, and arms (defined as "wall"), of the human dummy, for the construction of the mesh on the surfaces, the control was given on the size of the surfaces.
2. A method of the **offset** type with a uniform transition was added. This method calculates both the initial local height and the total height using the dimensions of the local element to have a uniform volume variation rate, three layers, and an adjacent element growth rate of change of 0.272. Subsequently, for the regions defined as "fluid", a method was assigned which controls the proportions of the extruded boundary layer cells, assigning a first cell value equal to 0.68 mm, five layers, and a rate of variation 0.272.
3. In the construction of the volumes, eight layers are required for the transitions between refined mesh and coarse mesh.

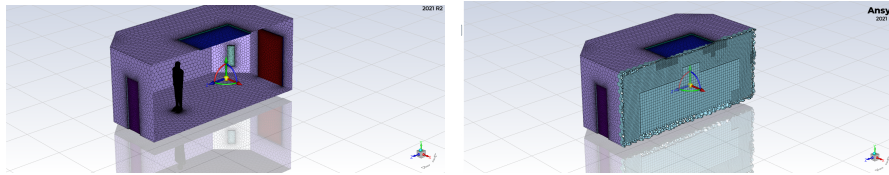


Figure 6.4.3: Case 6c#: on the left, we observe the mesh of the operating room and the human dummy present inside it according to the YZ plane, and on the right, the mesh refinement is shown.

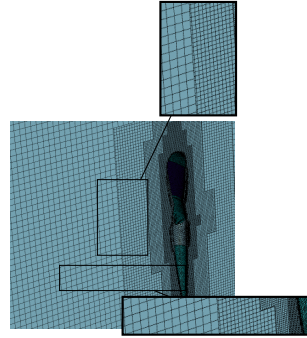


Figure 6.4.4: Case 6c#: detail of the mesh of the operating room and the human dummy.

The DoE permits obtaining the project points in a specific range and an optimal set of combinations of parameters that can be used in CFD simulations. The regulations defined the appropriate ranges of variation of the parameters of interest, whether physical or geometric (temperature, HVAC inlet velocity, pressure, the molar fraction of water vapor, and as a geometric parameter, position). To guarantee the appropriate number of parameter combinations, based on the problem, the most convenient method to explore the parameter space and cover it whole is applied.

In particular, for the case studied, an algorithm of the "*OptimalSpace-Filling Design*" type was opted with a "*design type*" which considers maxima and minima values to ensure sufficient coverage of the field for each parameter, and several samples assigned by the user. Based on the number of input parameters, in the case considered 8, and of output parameters, the optimal number of combinations varies between 10 and over 80 respectively if using a "*linear model*", "*full quadratic model*" or "*CCD*" (*Central Composite Designs*) (from Workbench manual [10] manual the number of recommended minimum combinations is  $8 \times$  (number of input parameters) ). In the case considered, there are 64 samples (combinations), and 64 tests were carried out with different combinations of input parameters. The samples obtained define the inputs for the 64 numerical simulations, see figure 6.4.5. Figure 6.4.5, left, represents in the big box at right, in the columns, the parameters

used to build the ROM and in the rows the values of parameters in the different ranges required. In the small box at the right, in the bottom part, are visible every 8 vertical lines that specify the ranges of parameters while the 64 obliques lines represent the 64 combinations of parameters. Figure 6.4.5, left, represents in the big box at right in the columns the parameters used to build the ROM and in the rows the values of parameters in the different ranges required. The small box at the right, in the bottom part, represents the trend of a parameter, e.g., the velocity inlet, with respect to the 64 combinations.

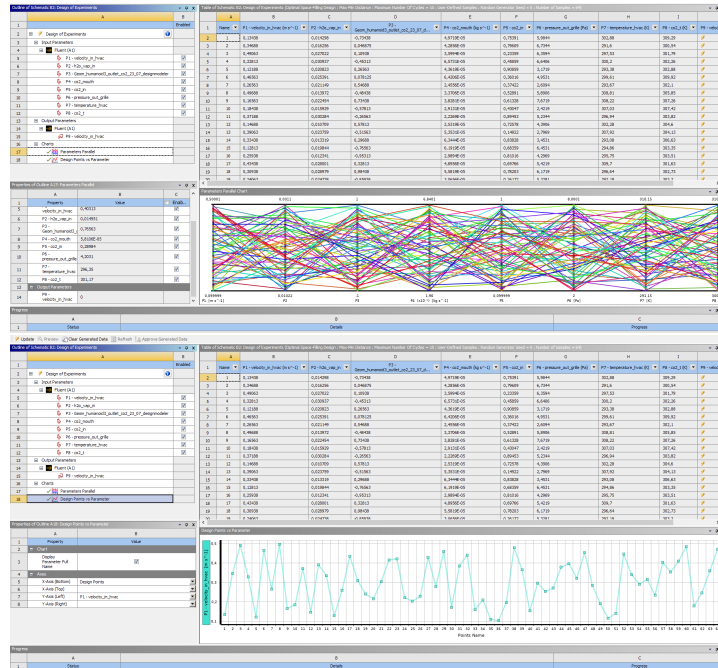


Figure 6.4.5: On the top is the trend between the minimum and maximum of the different input parameters. On the bottom is the trend of one of the input parameters with respect to the number of samples.

<b>Case study</b>	
<i>Room temperature [K]</i>	298.15
<i>Chamber pressure [Pa]</i>	101325

Table 31: Initial conditions for the room and the HVAC.

### 6.4.1 Case Study: case 6c# ROM

After having obtained, through the combinations of parameters given by the DoE, the snapshots of the field (reference solutions), an SVD algorithm was used for the construction of the ROM to compress

Parameter	Min value	Max value
Velocity [m/s]	0.1	0.5
Temperature [K]	291.15	310.15
$\Delta$ Pressure [Pa]	2.0	8.0
Molar Fraction H <sub>2</sub> O	0.01	0.031
Position human dummy [m]	-1.0	1.0

Table 32: Range of variation of the input parameters.

the solutions, in combination with an interpolation method which reconstructs the values of the variables of interest at each point within the chosen parametric interval.

From figure 6.4.6, it is possible to observe the field's average value for each snapshot and then the average over all the snapshots. Moreover, figure 6.4.6 reports two temperature fields (reference solutions), snapshot number 56 (left) and number 50 (right), obtained from the combinations of the parameters adopted for the ROM. The temperature variations of the two fields are shown with regard to the fields' average values. In particular, the left boxes on both the figures shown in figure 6.4.6 report all the snapshots obtained from CFD simulations. The columns contain the parameter values, which are used for the CFD simulations; the rows give all combinations of parameters used for the simulations. On the right boxes, the field of considered variable (in this case, the temperature) is illustrated for every combination (every row).

The first step is the ROM built, see figure 6.4.7. ROM built considers the division into two parts of the set of snapshots, as we explained in subsection 3.1.4, and that we reported following:

- *learning group*
- *validation or validation group*

and we obtain a curve called *Reduction*, which represents the precision of the learning set with respect to the number of modes, and a curve called *LOO*, which is the precision of the base of the modes for a snapshot not included in the learning set, see figure 6.4.7 in boxes at left for both figures. Every figure in figure 6.4.7 has at left, in the upper part, the number of snapshots used, in percentage and samples, and the method used to select the snapshots (in this case *optimal distribution*). On the left, in the bottom part, two curves are shown: the red curve is the relative error, and the green curve is the LOO. In addition, the number of modes is shown. The right part contains all the snapshots with the reduction relative errors, and between





excluded from the learning set. Figure 6.4.8 shows, for the temperature field, the difference between two different ROMs concerning the snapshots of the field. On the left part, in the bottom, are summarized the number of parameters used (in this case, 8), the number of learning snapshots used to build the ROM (32 and 45), and the number of modes for the two ROM (5 modes and 6 modes) are summarized. In the center part, for both ROM, the number of snapshots, the parameters used, and the reduction relative errors are shown in the columns. On the right part, the ROM of the two temperature fields are compared and the *difference* is shown. Similar considerations can be done for figure 6.5.8, and figure 6.5.13.

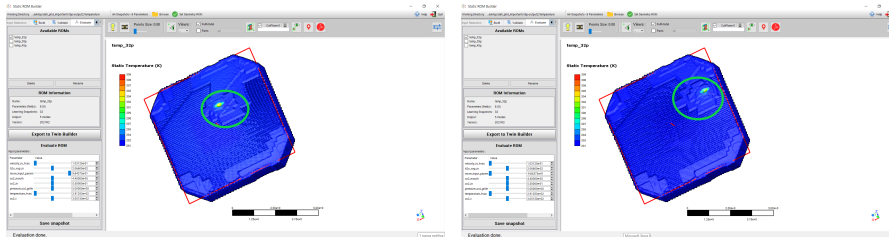


Figure 6.4.9: The two images show the temperature field obtained from the ROM as a geometric parameter varies, which determines a different position of the dummy.

Figure 6.4.9 shows the variation of the temperature field as the mannequin's position varies. Both the figures in figure 6.4.9 show the information on the ROM, the parameters (8), the learning snapshots (32), and the number of modes (5); at the bottom, the input parameters from which we observe the changes in the ROM (on the right part) are shown. In particular, in figure 6.4.9 it is possible to see a different position of the "human dummy" highlighted with green circles.

The *third step* is the use of ROM and the export of the result obtained. This result can be exported to TB as a model composed of the response surface model component and the SVD component or as a complete model (ROM), obtaining, as the input parameters vary over time, the snapshots of the temperature field.

## 6.5 ROM VS ROM

Different ROMs to understand the weight of the error in constructing ROM are compared. The ROMs are constructed using a different number of snapshots, i.e., a different number of CFD simulations. Figure 6.5.2 represent the temperature (top figure) and the RH (bottom figure) fields obtained by CFD simulations with the parameter values shown in the figure 6.5.1. In Case 6b#, 30 combinations of parameters, from

which obtained 30 snapshots of the field and the relative ROM, were used. Comparing the ROM results with CFD ones, we observe that the number of snapshots is insufficient to reproduce an identical field obtained using CFD. It was observed in subsection 3.1.4 the relevance of division in two parts, the learning set and validate set, of the snapshot set on the relative and absolute errors; in both cases, different snapshot numbers or different choices of element number for the learning set imply the variation from CFD result.

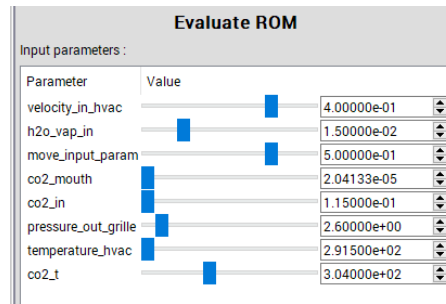


Figure 6.5.1: Parameter values used to compare CFD and ROM results

In Case 6b#, 30 combinations of parameters were used, from which were obtained 30 snapshots of the field and the relative ROM. Compared to the ROM results with CFD ones, we observe that the number of snapshots is insufficient to reproduce an identical field obtained using CFD, see figure 6.5.2.

The figures 6.5.3, and 6.5.4 illustrate the temperature field of the CFD compared to the one of the ROM for the values according to the one shown in figure 6.5.1. The temperature field of ROM is underestimated, see figure 6.5.3, and the RH field is overestimated, see figure 6.5.4. We can think that increasing the number of snapshots to construct the ROM can give a better result, but this is only partially correct.

The figures 6.5.3 and 6.5.5 show the CFD results for the temperature field and the ROM results. When 15 snapshots are used, the error with respect to CFD for the field of temperature is 4.53%. In case the ROM is built to 25 snapshots, the error with respect to CFD is 7.1%.

Figure 6.5.6 and figure 6.5.7 have the same structure of data that figure 6.4.7. The main difference shown between the results in the figures 6.5.7 and 6.4.7 (or figure 6.5.6) is the kind of error computed: the reduction relative error for the results in the figure 6.4.7 and ROM relative error for the results in the figure 6.5.7. In the right box in the bottom part where are shown the min and max values concerning the ROM reduction error. Tables 33 and 34 summarize the errors derived from the comparison CFD v.s. ROM and different kinds of error (re-

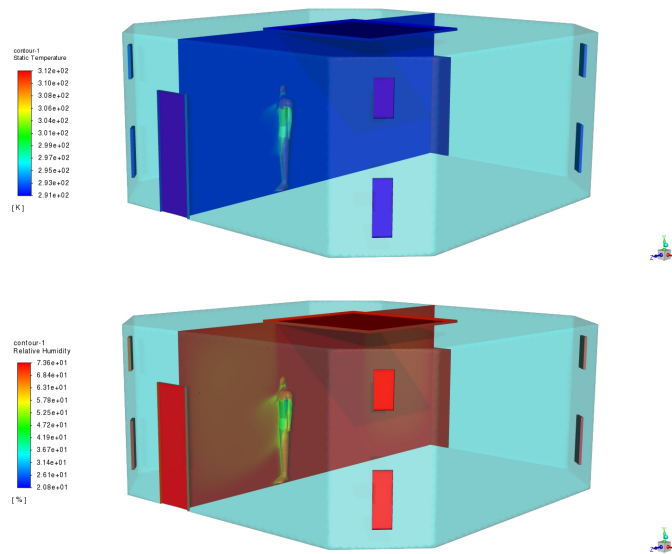


Figure 6.5.2: CFD simulations: on the top figure the result obtained through CFD of the temperature field; on the bottom the result obtained through CFD of the RH field;

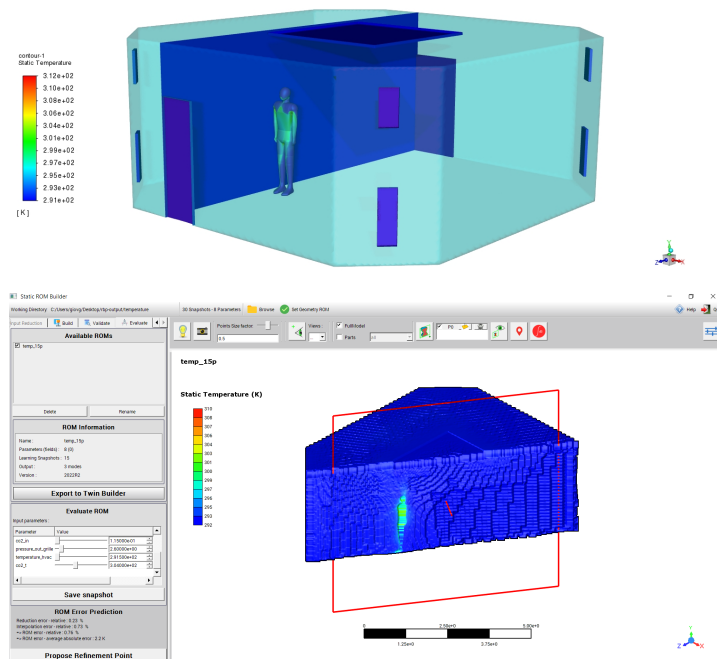


Figure 6.5.3: CFD-ROM comparison: on the top the result obtained through CFD of the temperature field; the bottom figure the ROM with 15 snapshots, with the same values of the parameters used, figure 6.5.1

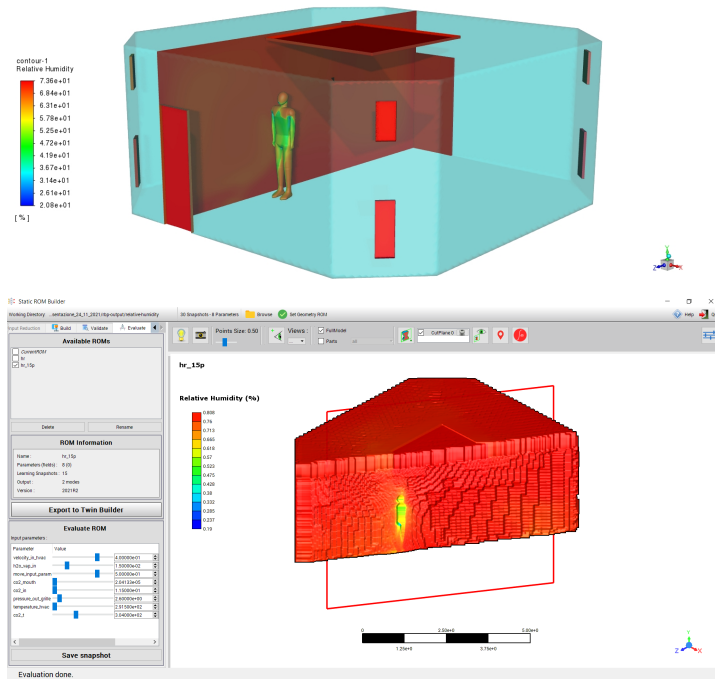


Figure 6.5.4: CFD-ROM comparison: on the top the result obtained through CFD of the RH field; the bottom figure the ROM with 15 snapshots, with the same values of the parameters used, figure 6.5.1

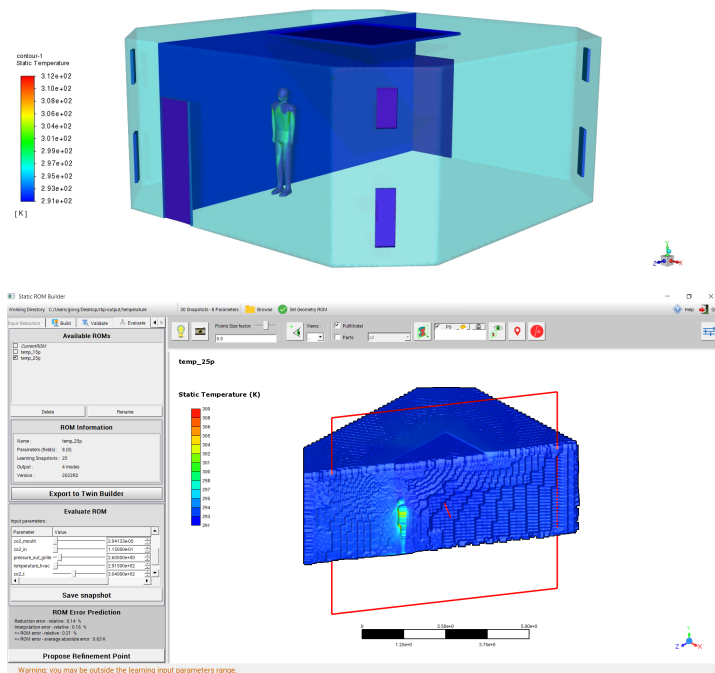


Figure 6.5.5: CFD-ROM comparison: the top figure shows the result obtained through CFD of the temperature field; the bottom figure shows the ROM for 25 snapshots, with the same values of the parameters shown in figure 6.5.1

duction error or ROM relative error).

Comparing the same set of snapshots made to 30 simulations and building the ROM with a different number of snapshots, we observe that the relative error and LOO are different, as we expected. In particular, when we use 15 snapshots/30 snapshots (i.e., 50.0% /100%), see figure 6.5.6, the relative error and the LOO are bigger than of the ones evaluated with 25 snapshots/30 snapshots (i.e., 83.33% /100%). To confirm that, figures 6.5.6, and 6.5.7 show the *ROM relative error*, and the *reduction error* between two ROM obtained by the same snapshot set but using a different number of snapshots for the learning set and validate set. In the ROM built with 15 snapshots, we observe a smaller error between the CFD temperature field and the ROM temperature field, see figure 6.5.5. In this case (30 snapshots), it could be that the number of snapshots is very few, or in some cases (64 snapshots), not bigger enough, and the errors are influenced by that. This influence could imply that by comparing the ROM and CFD results, the ROM constructed with 15 snapshots exhibits a better reproduction of the CFD field. In this case, the maximum number of snapshots is 30, and two ROMs are built, one by 15 and the other by 25.

We highlight again, that the number of the snapshots should be suitable to the number of parameters; in this case, 30 snapshots are half the minimum number of snapshots, 64.

We remember that the interpolation error is given by means difference between the reduction error and the ROM error, equations 3.1.18, 3.1.19. In addition, figure 6.5.8 shows two different ROM constructed by 15 snapshots and 25 snapshots and two different numbers of modes, three modes, and four modes. To the left and the right, a third viewer shows the difference between the results of the two selected ROMs.

A similar analysis can also be made for case 6c# when the parameter combinations and, consequently, the simulation number and snapshots are 64. Figures 6.5.9, 6.5.10, show the reduction error and LOO error for the construction of a ROM made of 32 snapshots/ 64 snapshots (50%), 45 snapshots/ 64 snapshots (70%) and 54 snapshots/ 64 snapshots (83.33%). Also, in these cases, as in the previous cases (maximum number of snapshots 30), the figures 6.5.9, and 6.5.10 exhibit the relative reduction error, and the figures 6.5.11, and 6.5.12 show the ROM error that decreased for a higher number of snapshots used in the ROM construction.

Similar to the previous cases also, in this case, it is possible to verify the difference in terms of the number of modes between two ROM built from the same set of snapshots but with a different number of snapshots, see figure 6.5.13. Two ROM, built with 32 snapshots and



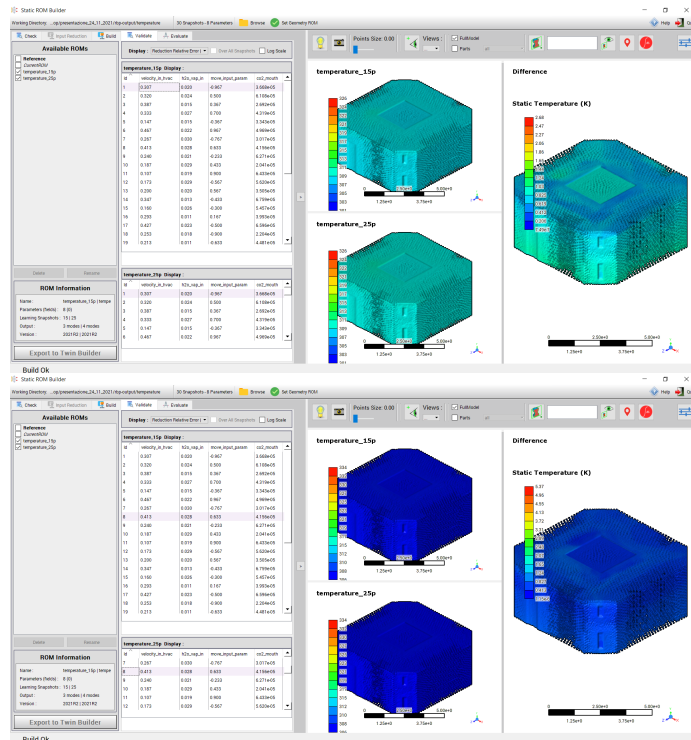


Figure 6.5:8: Temperature comparison between two different snapshots for two ROMs constructed with 15 snapshots and 25 snapshots

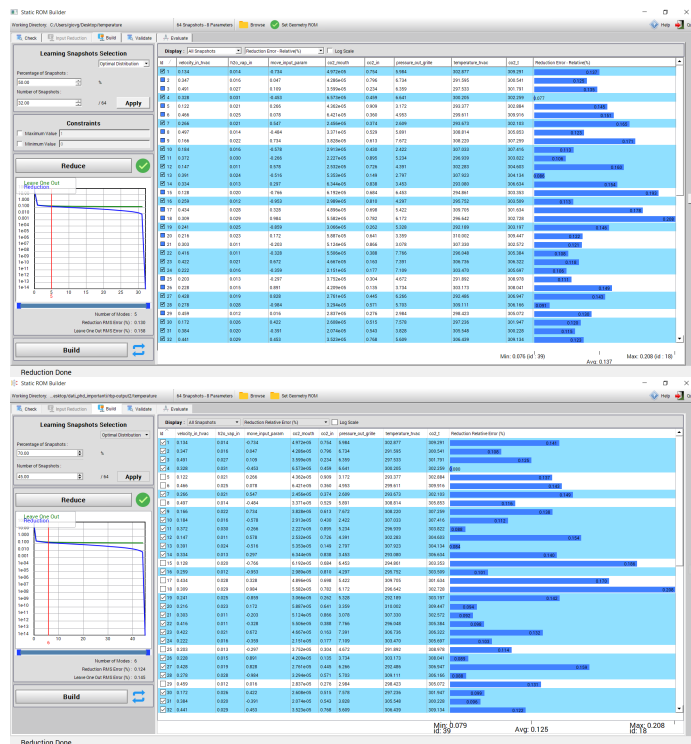


Figure 6.5:9: Temperature reduction error between two different snapshots for two ROMs constructed with 32 snapshots (top) and 45 snapshots (bottom)

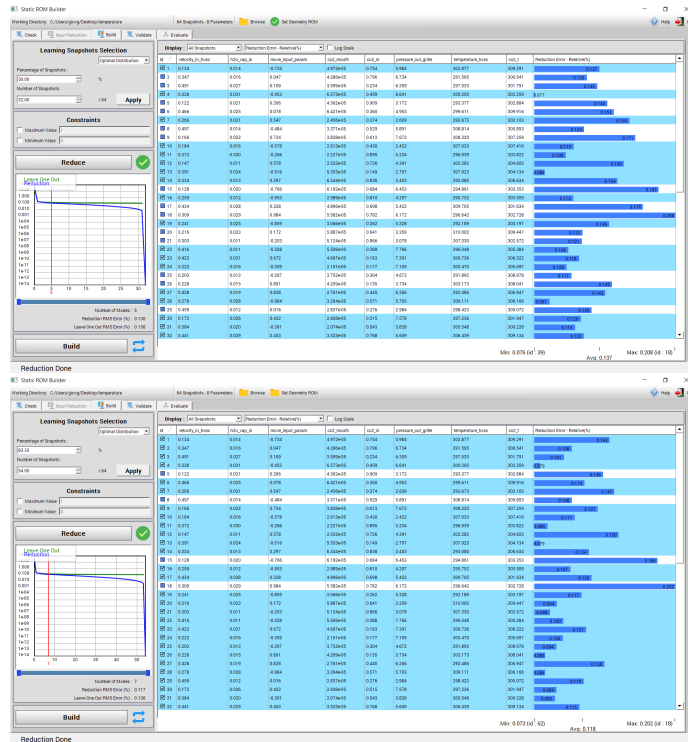


Figure 6.5.10: Temperature reduction error between two different snapshots for two ROMs constructed with 32 snapshots (top) and 54 snapshots (bottom)

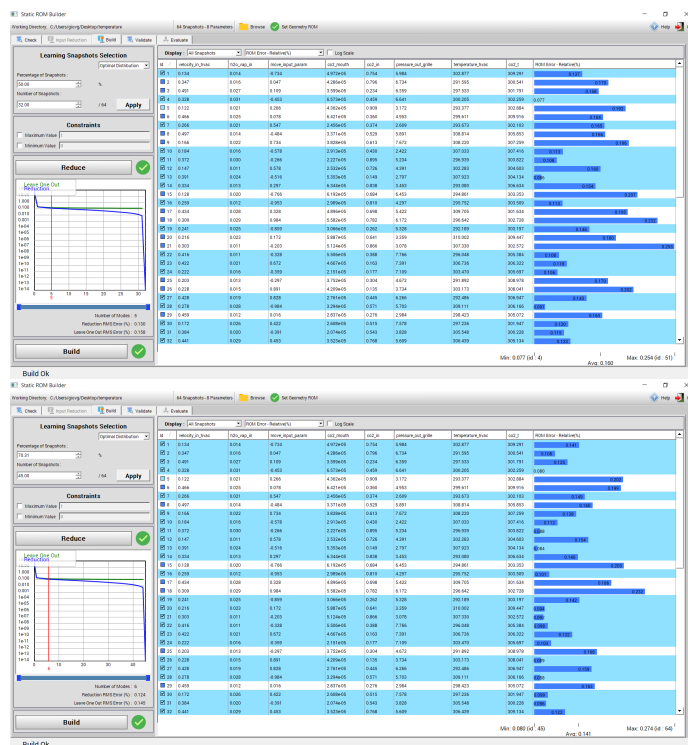


Figure 6.5.11: Temperature reduction error between two different snapshots for two ROMs constructed with 32 snapshots (top) and 45 snapshots (bottom)

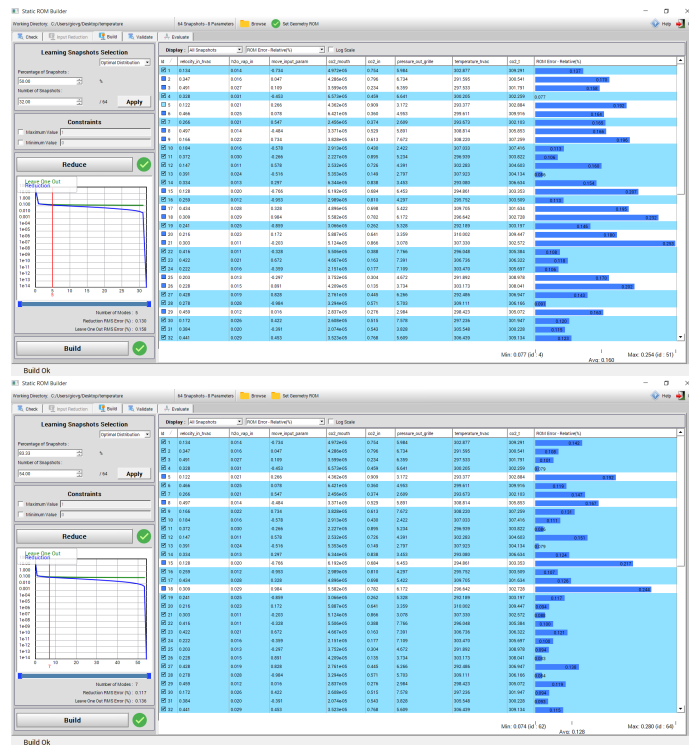


Figure 6.5.12: Temperature ROM error between two different snapshots for two ROMs constructed with 32 snapshots (top) and 54 snapshots (bottom)

45, in terms of temperature field, are compared in the figures 6.5.13 and show the difference in the temperature between the two ROM for every snapshot in the right area. The two ROM also have different numbers of modes, 5 and 6.

The comparison with CFD in figures 6.5.14, 6.5.15, 6.5.16, and 6.5.17 highlights three different errors for the three ROM; concerning that, it is possible to deduct the optimal number of snapshots to use for constructing the ROM. When 32 snapshots are used, the error concerning the CFD for the temperature field is 0.64%. In case the ROM is built to 45 snapshots, the error concerning the CFD is 1.94%, and at the end, for 54 snapshots, the error concerning the CFD is 1.94%, the same that there is for 45 snapshots.

To improve the accuracy, should increase the set of the snapshots, i.e., the reference solutions obtained from the CFD, more than the minimum number of snapshots required from the construction of ROM. In this way, it's possible to increase the number of snapshots of learning that can be selected without heavily reducing the number of snapshots in the validation set.

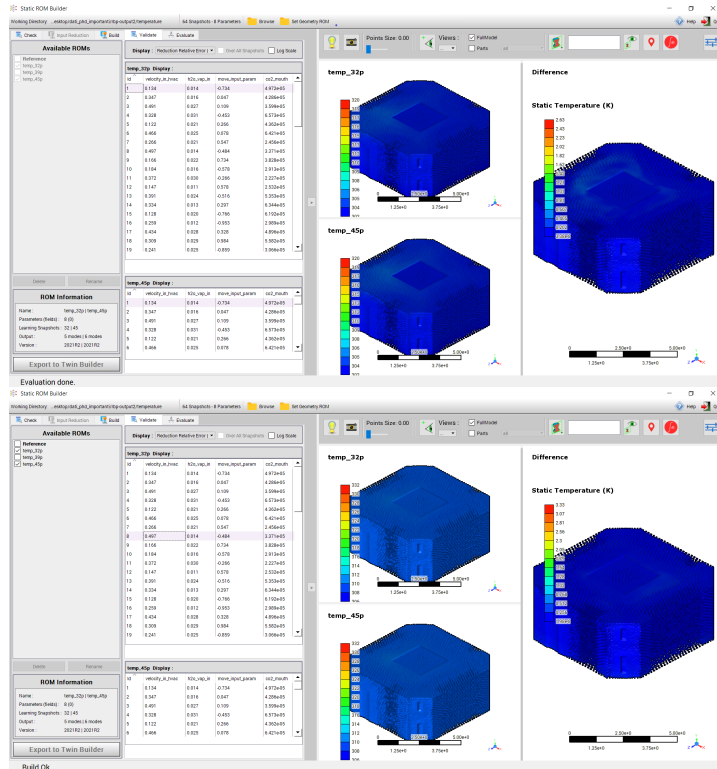


Figure 6.5.13: Temperature comparison between two different snapshots for two ROMs constructed with 32 snapshots and 45 snapshots

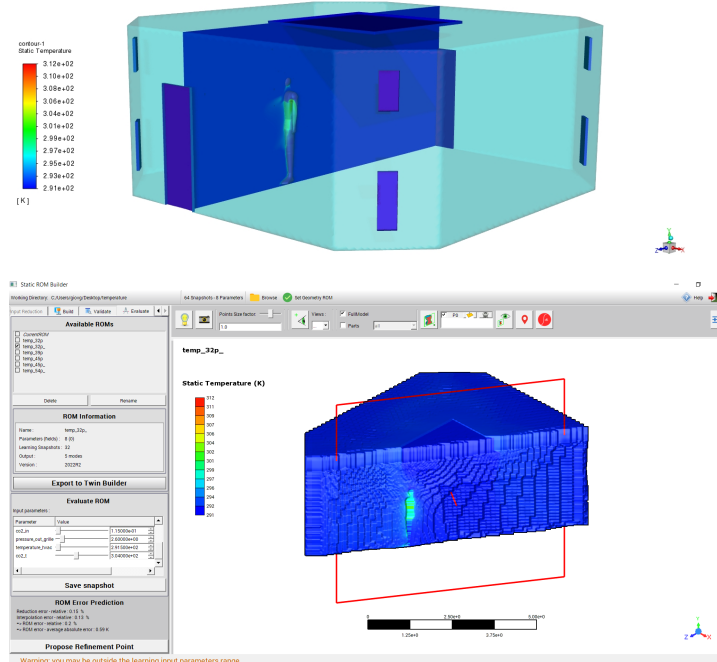


Figure 6.5.14: The two images show on the top the CFD temperature and on the bottom the ROM temperature with 32 snapshots

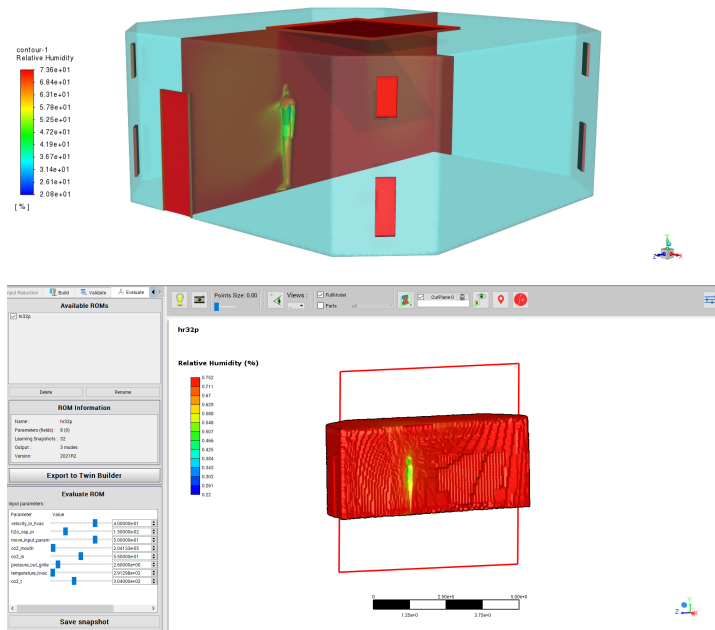


Figure 6.5.15: The two images show on the top the CFD relative humidity and the bottom the ROM relative humidity with 32 snapshots

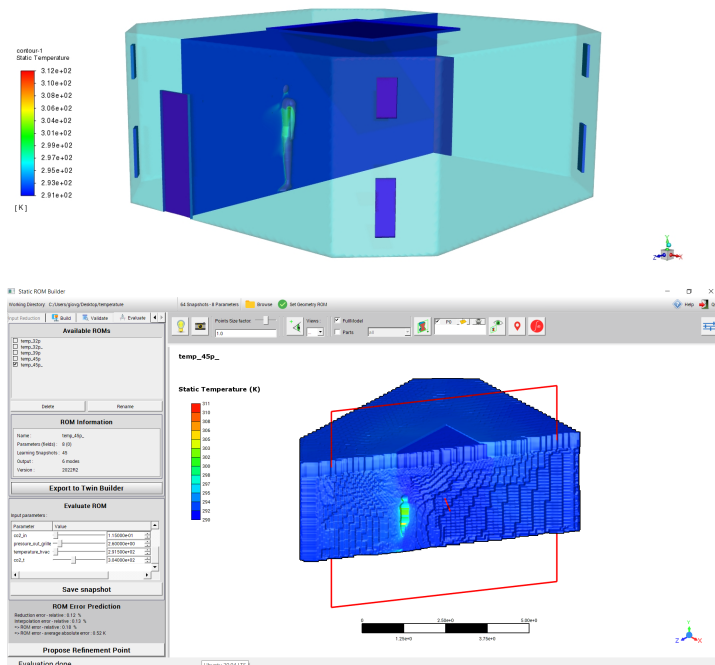


Figure 6.5.16: The two images show on the top the CFD temperature and on the bottom the ROM temperature with 45 snapshots

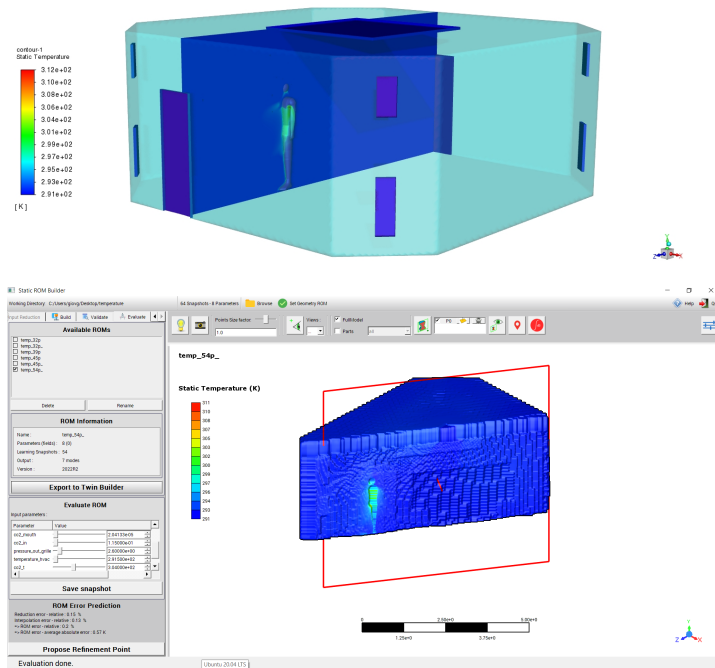


Figure 6.5.17: The two images show on the top the CFD temperature and on the bottom the ROM temperature whit 54 snapshots

## 6.6 RESULTS: CASE 6C# CFD VS ROM RESULT

The minimum number of combinations of parameters for the problem is 64. In the first analysis, we used 30 combinations, from which were obtained 30 snapshots of the field and the relative ROM. However, we verified that this number was insufficient, and based on the minimum number of combinations necessary for the number of parameters considered, we used 64 combinations. This number of combinations, obtained by the use of DoE, permits to construct of the ROM, in the case of temperature and also in the one RH, with a good agreement with respect to the results provided by the CFD field, see figures 6.6.5 and 6.6.6. Just as described, in particular, in Liu et al. [51], and also by Uyttenhove[86], the humidity field is higher than the temperature field in the zones where the temperature field is lower than the humidity field. The combination of the ROM and the morphing, as studied by Biancolini et al. [21], gives the possibility to study the influences that the different inlet parameters, temperature, and velocity airflow, different position of the surgeon, or variation of pressure or mole fraction, have on the operating theatre. This impact can be shown in the figures 6.6.1 and 6.6.2.

In figure 6.6.1, the change of temperature in the operating theatre and on the human dummy for the same environmental parameters when the human dummy changes her position is visible. Instead, in

figure 6.6.2, the influence parameter is the airflow velocity, and it is possible to observe the temperature variation in the operating theatre and human dummy.

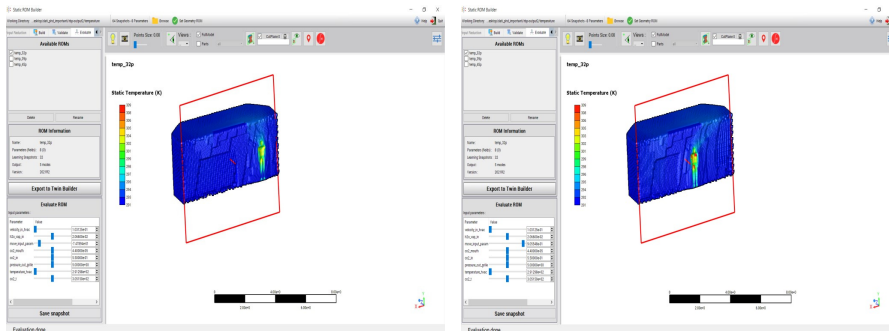


Figure 6.6.1: Different positions of the human dummy for the temperature field obtained from ROM: -0.75m (left) and 0.9m (right).

Figure 6.6.2 show the ROM of the influence on the temperature field of the inlet velocity airflow when the velocity change.

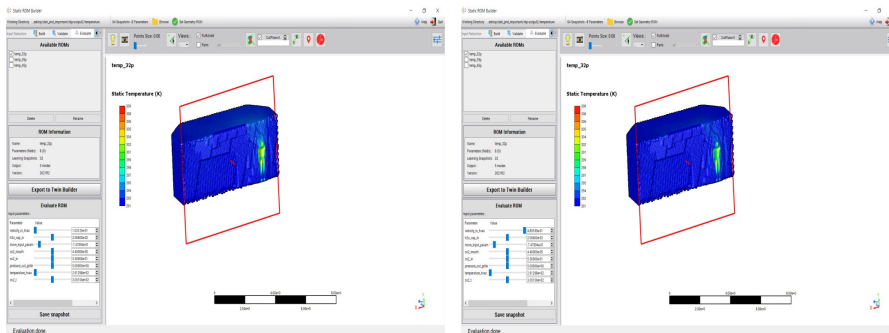


Figure 6.6.2: Different velocity of the human dummy for the temperature field obtained from ROM: 0.1m/s (left) and 0.5m/s (right).

After building the ROM, we can export it in TB software, figure 6.6.3. The results in figure 6.6.3 show the temperature field and the behavior of the average temperature in different time instants.

The input signal is given from the functions, but it might be possible to read and send to TB the input from the environment that will be processed by the DT in real-time, giving back the field of the variable of interest and the average of the variable on the field. In particular, the simulations are steady state, but the DT describes an evolution in the time of the field of variables, an unsteady case. This event, in any case, is not in conflict with the study results because the DT, in practice, considers that for every time step, the steady-state condition is obtained and produces the quasi-steady states of the fields (e.g., temperature).

In the simulations, 64 cores were used, and the time for each was about 2.5 sec per step, for a total of 22726 steps and 61 convergence

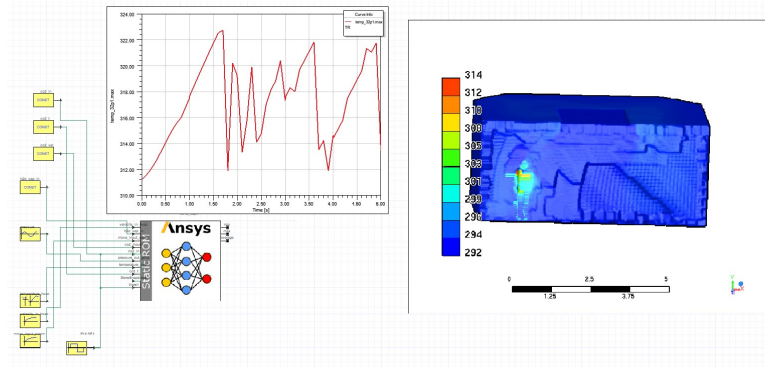


Figure 6.6.3: Operating theatre DT: in the left part, there are the probes of the inlet values; in the right part, there is the ROM and the behavior of average temperature.

simulations. The DT power using the ROM performs so fast that a real-time evaluation of the field of interest is observed at the update of the input parameters.

Figure 6.6.4 illustrates the process in terms of time (seconds, minutes, hours, days) for every single part. Similar to those shown in Kardampiki et al. [46], CFD, ROM, DT, and, at the bottom of the figure, are shown the ideal steps to produce a DT exploitable on a simple device.

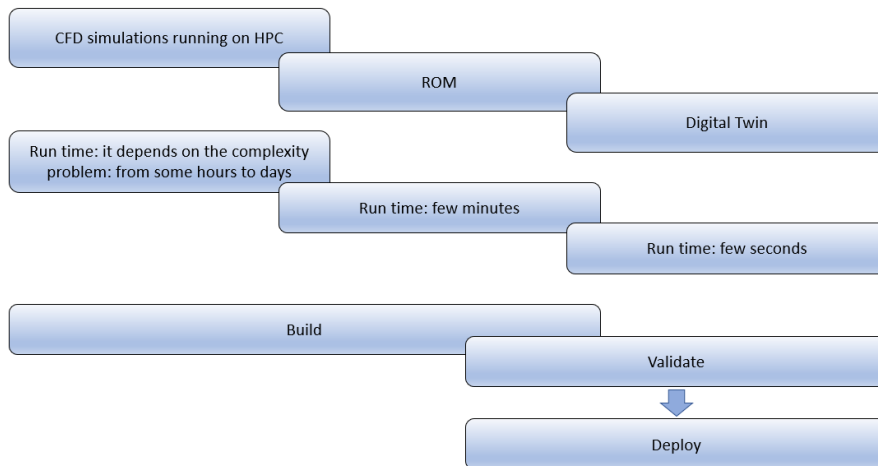


Figure 6.6.4: Map of features of the singular part: CFD, model, ROM

As shown previously, the HR produced, see figure 6.6.5 and 6.6.6 agrees with the results obtained in Liu et al. [50] and therefore is

inversely proportional to the temperature.

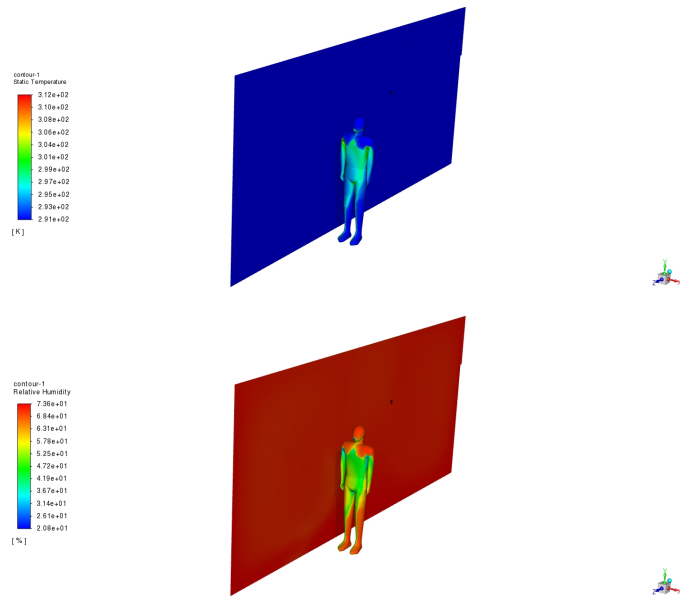


Figure 6.6.5: The temperature CFD field is shown on the top and the related RH field on the bottom.

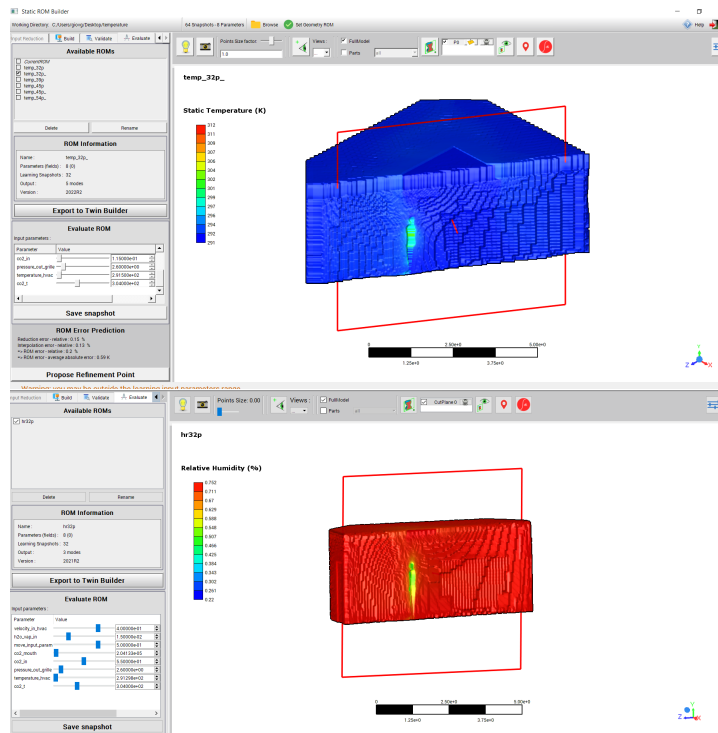


Figure 6.6.6: The ROM related to the temperature field is shown on the top, and the ROM related to the RH field is shown on the bottom.

The CFD field can be compared with that obtained from the ROM for each point belonging to the interval established for each variable to verify, in this way, the deviations and compare them with those obtained from TB, quantifying the errors, table 33, and 34. Table 33 shows the temperature error between the CFD and ROM field for the values of parameters reported in figure 6.5.1. Table 34 reports the RE, ROMRE. In addition, in the table, the Reduction, ROM, and Interpolation errors, and the ROM error- average absolute error in cases #6b and #6c for the values of the parameters shown in figure 6.5.1, are reported.

number of snapshots	snapshots %	Temperautre error
15/30	50%	4.53%
25/30	83.3%	7.1%
32/64	50%	0.64%
45/64	70.31%	1.94%
54/64	83.3%	1.94%

Table 33: In the table is shown the percent of the number of snapshots and the error between the CFD and ROM in cases #6b and #6c.

number snapshots	snapshots %	RRE (Average)	ROMRE (Average)	Reduction Error Relative	ROM error relative	ROM error average absolute error	Interpolation error relative
15/30	50%	0.167	0.202	0.23%	0.76%	2.2K	0.73%
25/30	83.3%	0.140	0.148	0.14%	0.21%	0.63K	0.15%
32/64	50%	0.137	0.160	0.15%	0.2%	0.59K	0.13%
45/64	70.31%	0.125	0.141	0.12%	0.18%	0.52K	0.13%
54/64	83.3%	0.118	0.128	0.15%	0.2%	0.57K	0.13%

Table 34: In the table is shown the percent of several snapshots, the RRE, ROMRE, Reduction, ROM, and Interpolation errors, and the ROM error- average absolute error in cases #6b and #6c.

## 6.7 DISCUSSION

Currently, the study needs to be completed for the experimental part, which is in the set-up phase. Comparing the experiments - CFD - ROM results is important to confirm the study and the good agreement with the CFD results and experimental ones. We briefly explained the experiment equipment and procedure in Chapter 5. According to literature references, we remember that the experiments consist of reproduction at a 1:10 scale of the operating theatre and using water as a fluid, see figure 6.7.1. One of the experimental difficulties is the replica of the scale model and carrying it out with fluid within a density 1000 times higher than air.



Figure 6.7.1: Model in Plexiglas of the operating theatre, scale 1:10, with two elements of medical staff.

In conclusion, an interesting application that uses the ROM to study the airflow in an operating theatre was illustrated and applied in a DT. The DT tool permits us to evaluate the better actions to take, in real-time, to correct the values of the variables considered for the air quality in the operating theatre. This might be possible thanks to continuous interaction with the room environment and might allow managing also the modifies from remote intervening quickly. The management of the parameters of interest (temperature, pressure, inlet velocity, etc.) might be with the help of a “Data Connector Component” that receives the actual values measured from probes in the room, as published in the studies by Yang et al. [93] and broadcasts them to the server or a device. It is possible to think of a system in which a microcontroller captures the voltage level provided by a temperature sensor and a humidity sensor using, e.g., software of the National Instruments or an Arduino Uno Board, an Arduino Ethernet Shield, Ethernet Crosswire, and a device, e.g., a tablet that monitors the air quality in the operating theatre, and in the critical areas, and real-time apply the correction to preserve, in this way, the air quality. Using the sensors is possible to measure the concentration of the virus or the contaminants products of breathing using the  $\text{CO}_2$  and to monitor the presence of it. The values of the parameters, e.g., temperature, can be given to DT, which uses them to simulate the behavior of the temperature field for every input sent. Communication occurs over a network using TCP/IP communication, and we can give the temperature values through a

temperature probe. The temperature probe sends the measurement to the TPC port number. This component acts as a server, and the remote application needs to function as a client. The two modes of synchronization could be possible:

- Real-time – Communication at every sample point is wall clock-based with nonblocking mode
- Blocked – Communication at every sample point is blocked until the data is received/sent within a given Time-out, as in the user guide of Ansys, I Twin Builder Help [9].

## 6.8 PRELIMINARY STUDIES: A COMPLETE SIMULATION AND FURTHER CONSIDERATIONS

Starting from the geometry reported in table 30, we realize a complete geometry considering the medical staff, patient, surgical lamp, and surgical table and consider the lamp with different sizes and positions as shown in figure 6.8.1, see for instance Liu et .al [52].

We run two simulations, simulation (a) and simulation (b), and table 35 shows the initial conditions for both simulations (a) and (b). The simulations (a) and (b) consider the geometry of the operating theatre complete and report the preliminary studies on the influence of surgical lamp sizes and positions.

<b>Case study</b>	
<i>Room temperature</i> [K]	298.15
<i>Chamber pressure</i> [Pa]	101325

Table 35: Initial conditions for the room and the HVAC.

Tables 36 and 37 reported the B.Cs for simulation (a) and simulation (b).

<b>Variables</b>	<b>value</b>
<i>Velocity</i> [m/s]	0.15
<i>Temperature</i> [K]	293.15
$\Delta$ <i>Pressure</i> [Pa]	4.0
Molar Fraction H <sub>2</sub> O	0.01
Position human dummy [m]	0

Table 36: Range of variation of the input parameters: simulation (a) and simulation (b).

In the table, 38 are reported the geometry changes; the mesh for both geometries is around 15 mil od nodes and 9 million cells.

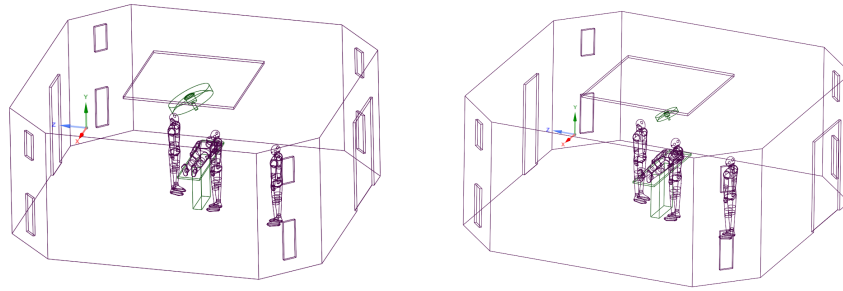


Figure 6.8.1: The geometries of the operating theatre with different surgical lamps: in the left figure (a), the radius of the lamp is smaller than the one in the right figure (b).

people	heat flux [W/m <sup>2</sup> ]	CO <sub>2</sub> [kg/s]
medical staff	47.5	$4 * 10^{-5}$
patient	30	$6 * 10^{-6}$
surgeon	57.5	0.137

Table 37: The table shows the relevant difference between simulations (a) and (b).

simulation	dimension surgical lights [mm]	distance surgical lights from HVAC [mm]
<i>a</i>	500	556
<i>b</i>	250	760

Table 38: The table shows the relevant difference between the simulations (a) and (b).

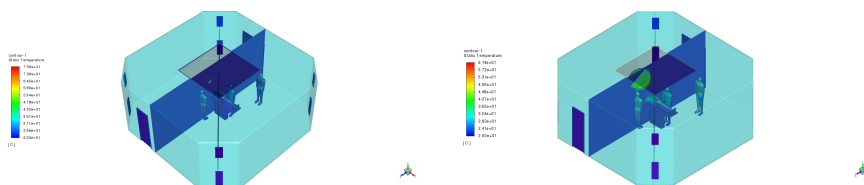


Figure 6.8.2: The temperature field for two different positions and dimensions of surgical lamp: in the left figure (a), the diameter of the surgical lamp is smaller than the one in the right figure (b).

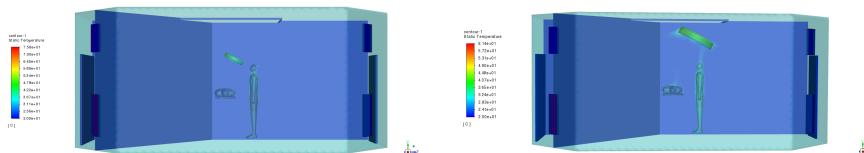


Figure 6.8.3: The temperature field for two different positions and dimensions of surgical lamp (in evidence): in the left figure (a), the diameter of the surgical lamp is smaller than the one in the right figure (b).

Figures 6.8.2 and 6.8.3 show the effects of different positions and sizes of surgical lamps in the operating theatre on the temperature field.

Figures 6.8.4, 6.8.5 show the effects of different positions and sizes of surgical lamps in the operating theatre on the velocity field. In particular, in the case where the surgical lamp has a radius = 250 mm and a distance from the HVAC of 760 mm, the velocity field is more uniform than in the case where the lamp dimension is bigger.

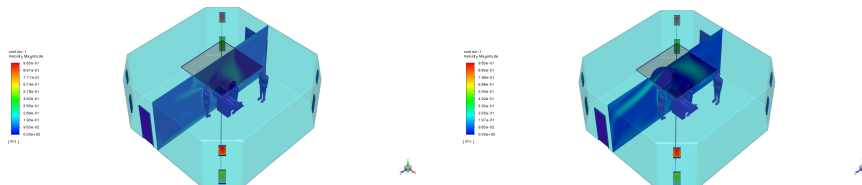


Figure 6.8.4: The velocity field for two different positions and dimensions of surgical lamps: in the left figure (a), the diameter of the lamp is smaller than the one in the right figure (b).

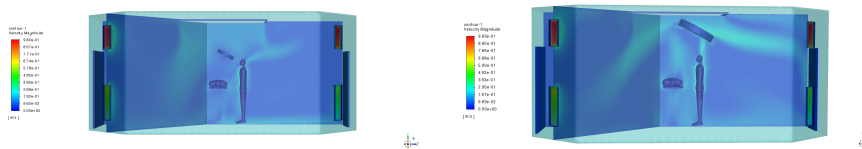


Figure 6.8.5: The velocity field for two different positions and dimensions of surgical lamps (in evidence): in the left figure (a), the diameter of the lamp is smaller than the one in the right figure (b).

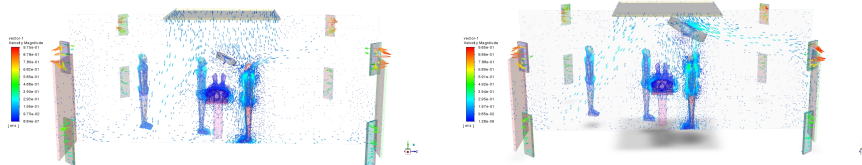


Figure 6.8.6: The vector field of velocity for two different positions and dimensions of surgical lamps (in evidence): in the left figure (a), the diameter of the lamp is smaller than the one in the right figure (b).

Figure 6.8.7 shows the vector field of velocity. In both cases (small lamp or big lamp), the vector field shows the recirculation areas near the patient.

Figure 6.8.8 shows the vector of the velocity field on a temperature slice. On the slice, there is a red line from that are extracted the values of temperature for simulation (a) and simulation (b), see figure 6.8.8.

Figure 6.8.9 shows the vector of the velocity field on a temperature slice and four lines to extract the trend of temperature and velocity. On the slice, there is a red line ( $y=1.35\text{m}$ ) from which are extracted

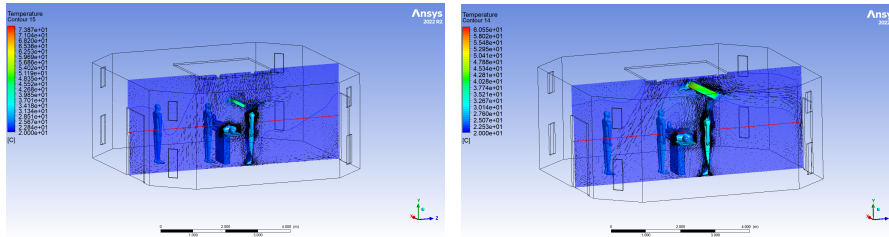


Figure 6.8.7: The temperature slice and vector field of velocity for two different positions and dimensions of surgical lamps (in evidence): in the left figure (a), the diameter of the lamp is smaller than the one in the right figure (b).

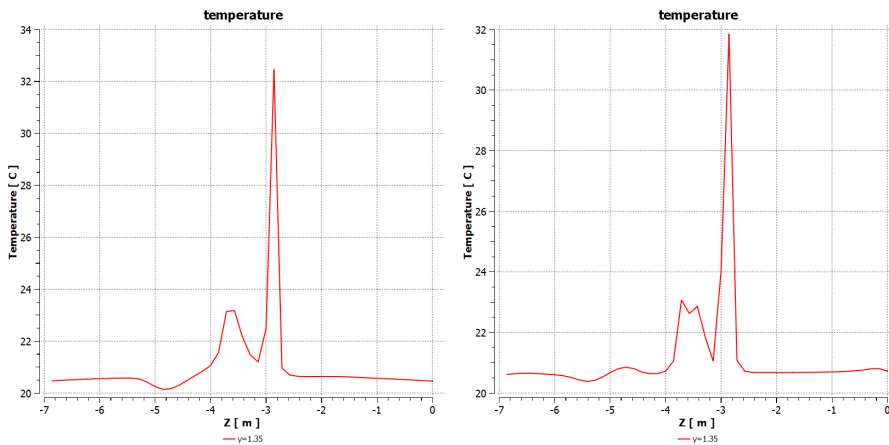


Figure 6.8.8: The chart of temperature extract on the red line ( $y=1.35\text{m}$ ) for two different positions and dimensions of surgical lamps (in evidence): in the left figure (a), the diameter of the lamp is smaller than the one in the right figure (b).

the values of velocity for simulation (a) and simulation (b), see figure 6.8.10. In figure 6.8.11, the velocity trend extract from three lines ( $z=-1.5$ ,  $z=-3.5$ , and  $z=-4.5$ ) for simulation (a) and simulation (b)

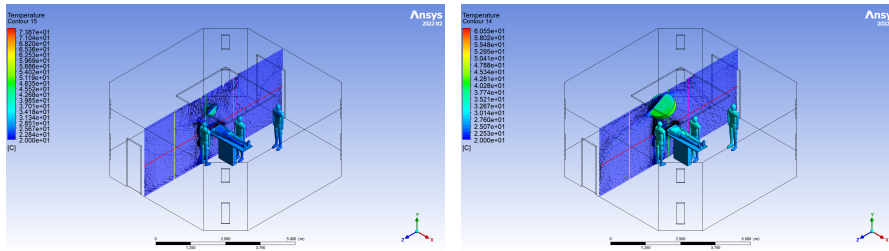


Figure 6.8.9: The temperature slice and vector field of velocity, and four lines to extract the velocity, for two different positions and dimensions of surgical lamps (in evidence): in the left figure (a), the diameter of the lamp is smaller than the one in the right figure (b).

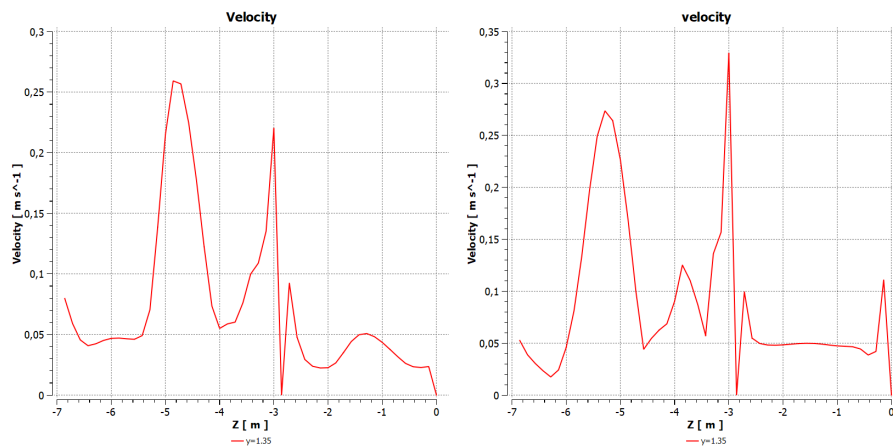


Figure 6.8.10: The chart of velocity extract on the red line ( $y=1.35\text{m}$ ) for two different positions and dimensions of surgical lamps (in evidence): in the left figure (a), the diameter of the lamp is smaller than the one in the right figure (b).

In the end, we give an overview of a possible implementation of work concerning the flexibility of RBF-morph, a change of the geometry of the operating theatre. Figures 6.8.12 and 6.8.13 show two different geometry and three different possibilities of the ventilation system: from a LAF to a UDF or Air curtains.

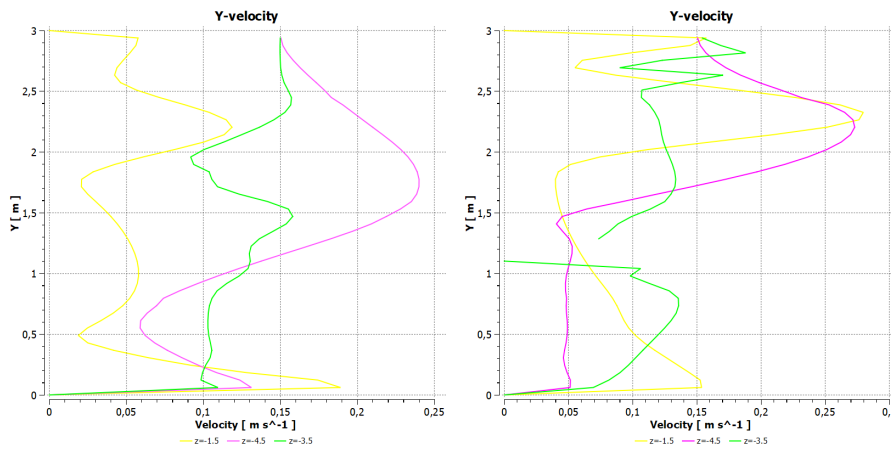


Figure 6.8.11: The chart of velocity extract on the three lines ( $z=-1.5$  yellow line,  $z=-3.5$  green line, and  $z=-4.5$  pink line) for two different positions and dimensions of surgical lamps (in evidence): in the left figure (a), the diameter of the lamp is smaller than the one in the right figure (b).

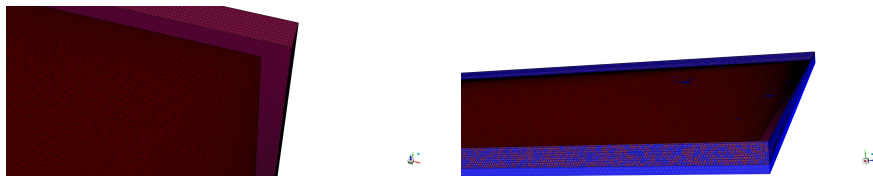


Figure 6.8.12: The different geometry of the ventilation system: in the left figure, the system is similar to a LAF or an air curtain; in the right figure, the system is similar to a UDF.



Figure 6.8.13: The different geometry of the ventilation system obtained by means RBF Morph.

# 7

---

## CONCLUSIONS

---

### 7.1 INTENTIONS AND ACCOMPLISHMENTS

In the hospital, it is well known a high possibility of developing infections. The aim of this Thesis is to help reduce and prevent this high possibility by using not only the CFD but also the DT.

The CFD simulations represent a fast way to obtain the field's behavior for the variable of interest and give the advantage of obtaining the results in a few hours without the difficulties of organizing and managing a sequence of experiments. However, CFD simulations can take several hours or days, and exploring all parameter combinations results in an arduous and complex process. Instead, we illustrated that the ROM produces three relevant benefits:

- the ROM can represent the fluid dynamic field with a sufficient degree of accuracy, see figure [6.5.14](#), and [6.5.15](#)
- the ROM can provide good indications of the influence of one parameter concerning another in relation to the problem considered, textcolorblacksee figures [6.6.1](#), [6.6.2](#).
- after data training construction, the ROM extraction requires a few minutes, and the consumption takes only some seconds.

Once built the ROM and exported to obtain a DT, the time of resolution and visualization of the problem decreased once again with respect to the experiment and CFD simulations. The possibility of interacting in real-time is a great advantage. It is possible to use a DT for both a predictive point of view in the event of maintenance, using, e.g., the virtual probes applied in a critical area where it is impossible to take the measurements with a real sensor, and a pro-reactive one where the management of damage might be forecast. For all the uses discussed of the management and control of environmental, safety, or operating conditions, the possibility to interact and apply, see figure [6.6.3](#), correctives is desirable in real-time. The results of the ROM are exported to TB, the temperature field picture, and the average temperature of the operating theatre are shown in the DT. The temperature trend changes

concerning the variation of parameters, and the DT can return the values of the field of the variables or the scalars (such as the average value of the temperature range or its maximum and minimum values) in real-time, showing the images of the temperature field for relevant instants in time.

The analysis can take into account the information about the environmental contamination tracking the amount of CO<sub>2</sub>, and in case of unsteady analysis, the AoA might be calculated.

The work was divided into two main parts: the CFD simulations and the experiments. The experiments to carry out consider a scale model filled with water instead of air. The model is made of a plexiglass box and an operating theatre, with a geometry similar to the operative one, which has been chosen for the CFD simulations. The advantage given by the ROM is to show the influence of a variable on the other instantaneously. If the ROM is interrogated in the range of parameter values used to build it, it is possible to maintain a contained simulation number decreasing, after its building, the use of HPC; in the other case, it will be necessary to increase the simulation number to cover new parameter values. The ROM process can be split into two parts: one part of creation and another of consumption. The first part of the ROM creation is composed of a step of generating training data and a step of ROM extraction. The ROM creation part takes a massive use of HPC. The second part, the consumption, requires only a few minutes, and the deployment requires simply a device.

Furthermore, building the DT is very simple to manage, and the results can be deployed on a simple device. This flexibility suggested that the DT can be embedded in a control system for the management of the HVAC of the operating theatre based on the ROM exported as an FMU usable on an IIoT platform.

## 7.2 OPEN ISSUES

In the future, the experiments will be used to help verify the match with the ROM built from simulations. Further analysis might imply the construction of an operating theatre complete with medical staff and a patient and, using the flexibility of RBF Morph, a changing of the geometry of the operating theatre and the position and dimensions of surgical lamps. As shown in the previous Chapter 6 in section 6.7, a preliminary geometry was built for the HVAC of the operating theatre, and a preliminary analysis was done on the different sizes of lamps. The change of the geometry allows for changing the kind of HVAC, simulating the air curtain or a unidirectional flow, similar to the plug,

thanks to the sliding wall, in addition to the HVAC illustrated in this work. The preliminary studies considering the possibility of changing the surgical lamp position using RBF show a change of the flow in the operating theatre between the two solutions (a) and (b)

# A

---

## ACH

---

The ACH term defines the air change per hour, and the relation is:

$$\text{ACH} = \frac{\left(\frac{\dot{m}}{\rho}\right)}{\text{Vol}_{\text{room}}} * 3600 \quad (\text{A.o.1})$$

with 3600 seconds.  $V_{\text{room}}$  is the volume of room and  $Q = \frac{\dot{m}}{\rho}$  volumetric flow rate or  $Q = vA$ .

The  $\dot{m}$  is mass flow rate  $\dot{m} = \rho vA$  and  $A$  is the surface, and  $v$  is the velocity.

The subscript 'water' indicates the sub-scale model, and the word 'air' indicates the full-scale model.

$$L_{\text{air}} = 10L_{\text{water}} \quad (\text{A.o.2})$$

$$v_{\text{air}} = \frac{10L_{\text{water}}}{t} \quad (\text{A.o.3})$$

$$Q_{\text{air}} = L_{1\text{air}}L_{2\text{air}}v_{\text{air}} \quad \text{con} \quad v_{\text{air}} = \frac{L_{\text{air}}}{t} \quad (\text{A.o.4})$$

$$Q_{\text{water}} = L_{1\text{water}}L_{2\text{water}}v_{\text{water}} \quad \text{con} \quad v_{\text{water}} = \frac{L_{\text{water}}}{t} \quad (\text{A.o.5})$$

$$\begin{aligned} Q_{\text{air}} &= L_{1\text{air}}L_{2\text{air}}v_{\text{air}} \Rightarrow Q_{\text{air}} = L_{1\text{air}}L_{2\text{water}}v_{\text{air}} \Rightarrow \\ &\Rightarrow Q_{\text{air}} = 10L_{1\text{air}}L_{2\text{water}}v_{\text{air}} \frac{10L_{\text{water}}}{t} \quad (\text{A.o.6}) \end{aligned}$$

$$Q_{\text{air}} = 1000(L_{\text{water}}L_{2\text{water}}v_{\text{water}}) \Rightarrow Q_{\text{air}} = 1000Q_{\text{water}} \quad (\text{A.o.7})$$

Considering the equal number of air changes:

$$\text{ACH}_{\text{air}} = \text{ACH}_{\text{water}} \quad (\text{A.o.8})$$

$$\text{ACH}_{\text{air}} = \frac{Q_{\text{air}}}{L_{\text{air}}^3} \quad (\text{A.o.9})$$

$$\text{ACH}_{\text{water}} = \frac{Q_{\text{water}}}{L_{\text{water}}^3} \quad (\text{A.o.10})$$

$$\begin{aligned} L_{\text{air}}^3 = 1000L_{\text{water}}^3 \Rightarrow \text{ACH}_{\text{air}} &= \frac{Q_{\text{air}}}{L_{\text{air}}^3} = \\ &= \frac{1000Q_{\text{water}}}{1000L_{\text{water}}^3} = \\ &= \text{ACH}_{\text{water}} \end{aligned} \quad (\text{A.o.11})$$

# B

---

## H<sub>2</sub>O

---

This Appendix shows a simple tool written using Wolfram Mathematica to evaluate the quantity of H<sub>2</sub>O present in the operating theatre.

```
Vtot = 138.11717(*7*7*3*);
Tctot = 20;
Ttot = Tctot + 273.15;
P = 101325;
Proom = 10;
Ppatot = P + Proom;
Ptot = Ppatot/1000;
Rconst = 8.31;
hr = 50/100;
Ph2osat = 2.338;
nspecies = 2;
```

```
psypd = PsychrometricPropertyData[<| "DryBulbTemperature" -> Quantity[Tctot, "DegreesCelsius"], "RelativeHumidity" -> Quantity[50, "Percent"] |>, {"MoleFractionDryAir", "MolarMass", "MoleFractionWater"}];
psypd[[1]];
```

```
psypd2[Temp1_, Hum1_] :=
Module[(*{i,MoleFractionDryAir,MolarMass,
MoleFractionWater}*){i, ncolH, ncolT,
Psyapp}, {ncolH = Table[i, {i, 40, 60, 2.5}],
ncolT = Table[i, {i, 20, 26, 0.7}],
Do[Print[ Psyapp = PsychrometricPropertyData[<| "DryBulbTemperature"
->
Quantity[ncolT[[i]], "DegreesCelsius"], "RelativeHumidity" -> Quantity[ncolH[[i]], "Percent"] |>, {"MoleFractionDryAir", "MolarMass", "MoleFractionWater"}]], {i, 1, 9} ]];
Return[Psyapp];
]
```

psypd2[Temp, Hum]

### Output 1

```
<| MoleFractionDryAir->0.991,MolarMass->28.864g/mol,  
MoleFractionWater->0.00927|>  
<| MoleFractionDryAir->0.990,MolarMass->28.853g/mol,  
MoleFractionWater->0.0103|>  
<| MoleFractionDryAir->0.989,MolarMass->28.841g/mol,  
MoleFractionWater->0.0114|>  
<| MoleFractionDryAir->0.987,MolarMass->28.829g/mol,  
MoleFractionWater->0.0125|>  
<| MoleFractionDryAir->0.986,MolarMass->28.815g/mol,  
MoleFractionWater->0.0138|>  
<| MoleFractionDryAir->0.985,MolarMass->28.801g/mol,  
MoleFractionWater->0.0151|>  
<| MoleFractionDryAir->0.984,MolarMass->28.786g/mol,  
MoleFractionWater->0.0165|>  
<| MoleFractionDryAir->0.982,MolarMass->28.769g/mol,  
MoleFractionWater->0.0180|>  
<| MoleFractionDryAir->0.980,MolarMass->28.752g/mol,  
MoleFractionWater->0.0195|>
```

```
psypd3[Temp2_, Hum2_] := Module[{i,MoleFractionDryAir,MolarMass,  
MoleFractionWater}{i, ncolH2, ncolT2, Psyapp2}, {ncolH2 = Table[i,  
{i, 40, 60, 2.5}], ncolT2 = DOEctrT, Do[Print[ Psyapp2 = Psycho-  
metricPropertyData[<| "DryBulbTemperature" -> Quantity[ncolT2[[i]],  
"DegreesCelsius", "RelativeHumidity" -> Quantity[ncolH[[i]], "Per-  
cent"|>, {"MoleFractionDryAir", "MolarMass", "MoleFractionWater",  
"WetBulbTemperature"}]], {i, 1, 9} ]]; Return[{ncolT2, ncolH2}] ] psypd3[Temp,  
Hum] <| "MoleFractionDryAir" -> 0.980, "MolarMass" -> Quantity[28.752,  
("Grams")/("Moles")], "MoleFractionWater" -> 0.0195|>
```

### Output 2

```
<| MoleFractionDryAir->0.982,MolarMass->28.765g/mol,  
MoleFractionWater->0.0184,WetBulbTemperature->21°C|>  
<| MoleFractionDryAir->0.974,MolarMass->28.681g/mol,  
MoleFractionWater->0.0261,WetBulbTemperature->26°C|>  
<| MoleFractionDryAir->0.990,MolarMass->28.857g/mol,  
MoleFractionWater->0.00998,WetBulbTemperature->13°C|>
```

```

<| MoleFractionDryAir->0.974,MolarMass->28.676g/mol,
MoleFractionWater->0.0265,WetBulbTemperature->26°C | >
<| MoleFractionDryAir->0.987,MolarMass->28.828g/mol,
MoleFractionWater->0.0126,WetBulbTemperature->15°C | >
<| MoleFractionDryAir->0.982,MolarMass->28.77g/mol,
MoleFractionWater->0.0179,WetBulbTemperature->19°C | >
<| MoleFractionDryAir->0.967,MolarMass->28.601g/mol,
MoleFractionWater->0.0334,WetBulbTemperature->28°C | >
<| MoleFractionDryAir->0.987,MolarMass->28.82g/mol,
MoleFractionWater->0.0134,WetBulbTemperature->15°C | >
<| MoleFractionDryAir->0.988,MolarMass->28.83g/mol,
MoleFractionWater->0.0124,WetBulbTemperature->14°C | >

```

```

{{31.5423, 36.7128, 19.2862, 34.9893, 21.3928, 26.3718, 36.5213, 20.0523,
18.1372}, {40., 42.5, 45., 47.5, 50., 52.5, 55., 57.5, 60.}} For [ncolT = Ta-
ble[i, {i, 20, 26, 0.7}]; ncolH = Table[i, {i, 40, 60, 2.5}]; i = 1, i <= 9, i++,
{Print[ncolT[[i]], Print[ncolH[[i]]]} ];

```

### Output 3

```

20. 40. 20.7 42.5 21.4 45. 22.1 47.5 22.8 50. 23.5 52.5 24.2 55. 24.9 57.5
25.6 60.

```

```

psypd3[Temp2_, Hum2_] := Module[{i,MoleFractionDryAir,MolarMass,
MoleFractionWater}){i, ncolH2, ncolT2, Psyapp2}, {ncolH2 = Table[i,
{i, 40, 60, 2.5}], ncolT2 = DOEctrT, Do[Print[ Psyapp2 = Psychro-
metricPropertyData[<| "DryBulbTemperature" -> Quantity[ncolT2[[i]],
"DegreesCelsius", "RelativeHumidity" -> Quantity[ncolH[[i]], "Per-
cent"] | >, {"MoleFractionDryAir", "MolarMass", "MoleFractionWater"}]],
{i, 1, 9} ]]; Return[{ncolT2, ncolH2}] ]

```

```

psypd3[Temp, Hum]

```

```

PsychrometricPropertyData[<| "DryBulbTemperature" -> Quantity[19.2862,
"DegreesCelsius", "RelativeHumidity" -> Quantity[45.0, "Percent"] | >,
{"MoleFractionDryAir", "MolarMass", "MoleFractionWater"}]

```

### Output 4

```

<| MoleFractionDryAir->0.982,MolarMass->28.765g/mol,
MoleFractionWater->0.0184 | > <| MoleFractionDryAir->0.974,MolarMass-
>28.681g/mol,
MoleFractionWater->0.0261 | > <| MoleFractionDryAir->0.990,MolarMass-

```

```

>28.857g/mol,
MoleFractionWater->0.00998 | > < | MoleFractionDryAir->0.974,MolarMass-
>28.676g/mol,
MoleFractionWater->0.0265 | > < | MoleFractionDryAir->0.987,MolarMass-
>28.828g/mol,
MoleFractionWater->0.0126 | > < | MoleFractionDryAir->0.982,MolarMass-
>28.77g/mol,
MoleFractionWater->0.0179 | > < | MoleFractionDryAir->0.967,MolarMass-
>28.601g/mol,
MoleFractionWater->0.0334 | > < | MoleFractionDryAir->0.987,MolarMass-
>28.82g/mol,
MoleFractionWater->0.0134 | > < | MoleFractionDryAir->0.988,MolarMass-
>28.83g/mol,
MoleFractionWater->0.0124 | >

```

#### Output 5

```

{{31.5423, 36.7128, 19.2862, 34.9893, 21.3928, 26.3718, 36.5213, 20.0523,
18.1372}, {40., 42.5, 45., 47.5, 50., 52.5, 55., 57.5, 60.}}

```

#### Output 6

```

< | "MoleFractionDryAir" -> 0.990, "MolarMass" -> Quantity[28.857,
("Grams")/("Moles)], "MoleFractionWater" -> 0.00998 | >

```



---

## CO<sub>2</sub>

---

This appendix briefly describes the evaluation of CO<sub>2</sub> given as B.C. of the inlet for the human dummy. The work references are Balocco et al. [16], and Chung et al. [28].

We consider that the average breath is 500ml c.a and 14 breaths in a minute in a relaxed situation. That implies that in a min, there is a quantity of area equal to 7000ml/min (7l/min), i.e., 420 l/h. The breath is composed of two parts: inspiration and exhalation.

We consider 210l/h, but we know that the air inspired contains 0.03% CO<sub>2</sub> and the air exhaled the 4%. In practice, the CO<sub>2</sub> exhaled is around 8l/h. The amount of CO<sub>2</sub> in Kg/s that we considered is for the medical staff  $4 * 10^{-5}$  and for patient  $6 * 10^{-6}$  considering that the CO<sub>2</sub> density between 18°C and 35°C is 1.8 kg/m<sup>3</sup> and 1.75 kg/m<sup>3</sup>.

---

## BIBLIOGRAPHY

---

- [1] UNE 100713:2005: *Instalaciones de acondicionamiento de aire en hospitales - Air conditioning in hospitals*, 2005. (pag 34(2)b ).
- [2] *Particle Image Velocimetry*. Cambridge University Press, 2011. (pag 55).
- [3] Hervé Abdi. Singular value decomposition (svd) and generalized singular value decomposition. *Encyclopedia of measurement and statistics*, 907:912, 2007. (pag 7).
- [4] Amar Aganovic, Guangyu Cao, Liv-Inger Stenstad, and Jan Gunnar Skogås. Impact of surgical lights on the velocity distribution and airborne contamination level in an operating room with laminar airflow system. *Building and Environment*, 126:42–53, 2017. (pag 9 and 14).
- [5] A Agodi, F Auxilia, M Barchitta, ML Cristina, D D’Alessandro, I Mura, M Nobile, C Pasquarella, Sergio Avondo, Patrizia Bellocchi, et al. Operating theatre ventilation systems and microbial air contamination in total joint replacement surgery: results of the gisio-ischia study. *Journal of Hospital Infection*, 90(3):213–219, 2015. (pag 3(2)b ).
- [6] Rafat Al-Waked. Effect of ventilation strategies on infection control inside operating theatres. *Engineering Applications of Computational Fluid Mechanics*, 4(1):1–16, 2010. (pag 4).
- [7] Malin Alsved, Anette Civilis, Peter Ekolind, Ann Tammelin, A Erichsen Andersson, J Jakobsson, T Svensson, M Ramstorp, Sasan Sadrizadeh, PA Larsson, et al. Temperature-controlled airflow ventilation in operating rooms compared with laminar airflow and turbulent mixed airflow. *Journal of Hospital Infection*, 98(2):181–190, 2018. (pag xi(2)b , 14, and 17(2)b ).
- [8] Inc ANSYS. *Fluent User Guide*. ANSYS, Inc, South Pointe 2600 Ansys Drive, Canonsburg, PA, USA., 2021. (pag 22 and 26).
- [9] Inc ANSYS. *Twin Builder Help risorse online*. ANSYS, Inc, South Pointe 2600 Ansys Drive, Canonsburg, PA, USA., 2021. (pag 26, 27, and 90).
- [10] Inc ANSYS. *Workbench Help risorse online*. ANSYS, Inc, South Pointe 2600 Ansys Drive, Canonsburg, PA, USA., 2021. (pag 29 and 68).

- [11] LUCIO TIZIANO ARANEO, FEDERICO PEDRANZINI, LUIGI PIETRO COLOMBO, et al. Development of a scaled model for the experimental study of air flow patterns in a conditioned indoor space. In *Proceedings of ASME-ATI-UIT 2015 Conference on Thermal Energy Systems: Production, Storage, Utilization and the Environment*, pages 1–7, 2015. (pag 8, 50, and 53).
- [12] ANSI ASHRAE. Standard 170-2013. ventilation of health care facilities. *American Society of Heating, Refrigerating and Air-Conditioning Engineers, Inc, Atlanta*, 2013. (pag 21 and 29).
- [13] Ashrae Handbook Fundamentals Ashrae and Ga Atlanta. American society of heating. *Refrigerating and Air-Conditioning Engineers*, 1, 2009. (pag 62).
- [14] A Balducci, M Grigioni, Giorgio Querzoli, GP Romano, C Daniele, G D’Avenio, and V Barbaro. Investigation of the flow field downstream of an artificial heart valve by means of piv and ptv. *Experiments in fluids*, 36:204–213, 2004. (pag 55).
- [15] Carla Balocco, Giuseppe Petrone, Giuliano Cammarata, et al. Numerical investigation of different airflow schemes in a real operating theatre. *Journal of Biomedical Science and Engineering*, 8(02):73, 2015. (pag 6, 30, and 67).
- [16] Carla Balocco, Giuseppe Petrone, Giuliano Cammarata, Pietro Vitali, Roberto Albertini, and Cesira Pasquarella. Indoor air quality in a real operating theatre under effective use conditions. *Journal of Biomedical Science and Engineering*, 2014, 2014. (pag 4, 6, 9, 29, 33(2)b , 62(2)b , 66(2)b , 67, and 105).
- [17] Malek Ben Salem, Olivier Roustant, Fabrice Gamboa, and Lionel Tomaso. Universal prediction distribution for surrogate models. *SIAM/ASA Journal on Uncertainty Quantification*, 5(1):1086–1109, 2017. (pag 27).
- [18] Malek Ben Salem and Lionel Tomaso. Automatic selection for general surrogate models. *Structural and Multidisciplinary Optimization*, 58(2):719–734, 2018. (pag 7).
- [19] Sandra I Berríos-Torres, Craig A Umscheid, Dale W Bratzler, Brian Leas, Erin C Stone, Rachel R Kelz, Caroline E Reinke, Sherry Morgan, Joseph S Solomkin, John E Mazuski, et al. Centers for disease control and prevention guideline for the prevention of surgical site infection, 2017. *JAMA surgery*, 152(8):784–791, 2017. (pag 1).
- [20] Marco Evangelos Biancolini. *Fast radial basis functions for engineering applications*. Springer, 2017. (pag 25).

- [21] M.E Biancolini. *RBF for Fluent, User guide*, 2021. (pag 66 and 84).
- [22] Gabriel Birgand, Gaëlle Toupet, Stephane Rukly, Gilles Antoniotti, Marie-Noelle Deschamps, Didier Lepelletier, Carole Pornet, Jean Baptiste Stern, Yves-Marie Vandamme, Nathalie van der Mee-Marquet, et al. Air contamination for predicting wound contamination in clean surgery: a large multicenter study. *American journal of infection control*, 43(5):516–521, 2015. (pag xi and 5).
- [23] Fernando Martín Biscione. Rates of surgical site infection as a performance measure: are we ready? *World Journal of Gastrointestinal Surgery*, 1(1):11, 2009. (pag 2).
- [24] S. L Boer. A cfd study of operation room air conditioning: Air curtain performance. Master's thesis, Grand Valley State University, 12 2020. (pag 6).
- [25] Spencer Lee Boer. A cfd study of operation room air conditioning: Air curtain performance. 2020. (pag 6).
- [26] Osama Butt, Haider Latif, K Reinartz, G Hultmark, and A Afshari. Advanced airflow distribution system for reducing airborne virus exposure in hospital rooms. In *Indoor Air 2022*. ISIAQ, 2022. (pag 67).
- [27] Guangyu Cao, Anders M Nilssen, Zhu Cheng, Liv-Inger Stenstad, Andreas Radtke, and Jan Gunnar Skogås. Laminar airflow and mixing ventilation: Which is better for operating room airflow distribution near an orthopedic surgical patient? *American journal of infection control*, 47(7):737–743, 2019. (pag 9 and 14).
- [28] Zhu Cheng, Cao Guangyu, Amar Aganovic, and Li Baizhan. Experimental study of the interaction between thermal plumes and human breathing in an undisturbed indoor environment. *Energy and Buildings*, 207:109587, 2020. (pag 67 and 105).
- [29] European Committee. *EU-GMP - Guide to Good Manufacturing Practice, Annex 1, Manufacture of Sterile Medicinal Products*, 2008. (pag 20).
- [30] Giuseppe D'Avenio, Mauro Grigioni, Carla Daniele, Umberto Morbiducci, and Kathrin Hamilton. 3d velocity field characterization of prosthetic heart valve with two different valve testers by means of stereo-piv. In *2015 37th Annual International Conference of the IEEE Engineering in Medicine and Biology Society (EMBC)*, pages 3327–3330. IEEE, 2015. (pag 55).
- [31] C Di Santis. Design and optimization of operating theater ventilation and contamination control system through an experimentally

- validated cfd model. Master's thesis, Politecnico di Milano, 2013. (pag [xi](#), [xix](#), [1](#), [4](#), [6](#), [14\(2\)b](#), [18](#), [19](#), [20](#), [31](#), [32](#), [59](#), [62](#), [65](#), and [67](#)).
- [32] Ente Nazionale Italiano di Unificazione. *UNI EN ISO 14698:1-2, Camere bianche ed ambienti associati controllati: Controllo della biocontaminazione*, 2004. (pag [3](#) and [29](#)).
- [33] Ente Nazionale Italiano di Unificazione. *UNI EN 1822:2010 - parts 1-4, Filtri per l'aria ad alta efficienza (EPA, HEPA e ULPA)*, 2010. (pag [xi](#), [3\(2\)b](#), [17\(2\)b](#), [19\(2\)b](#), and [29](#)).
- [34] Ente Nazionale Italiano di Unificazione. *UNI 11425:2011, Impianto di ventilazione e condizionamento a contaminazione controllata (VCCC) per il blocco operatorio - Progettazione, installazione, messa in marcia, qualifica, gestione e manutenzione*, 2011. (pag [xix](#), [4](#), [14](#), and [20](#)).
- [35] Ente Nazionale Italiano di Unificazione. *UNI EN ISO 14644 - parts 1-10, Cleanrooms and associated controlled environments*, 2011. (pag [20\(2\)b](#) ).
- [36] Ente Nazionale Italiano di Unificazione. *UNI EN 779:2012, Filtri d'aria antipolvere per ventilazione generale. Determinazione della prestazione di filtrazione*, 2012. (pag [17](#) and [18\(2\)b](#) ).
- [37] DDBE Du Bois. A formula to estimate the approximate surface area if height and weight be known. *Nutrition*, 5:303–313, 1989. (pag [62](#)).
- [38] PE Farhad Memarzadeh and Andrew P Manning. Comparison of operating room ventilation systems in the protection of the surgical site. (pag [1](#)).
- [39] FDA-Food. *FDA-Food and Drug Administration-Current Good Manufacturing Practice, European Draft Guidance*, 2008. (pag [20](#)).
- [40] D Ferrara. Experimental investigation of spray flow field and its interaction with uav wake. Master's thesis, Università degli Studi di Napoli Federico II, 2022. (pag [55](#)).
- [41] Elizabeth U Finlayson, Ashok J Gadgil, Tracy L Thatcher, and Richard G Sextro. Pollutant dispersion in a large indoor space: Part 2-computational fluid dynamics (cfd) predictions and comparison with a scale model experiment for isothermal flow. 2002. (pag [50](#)).
- [42] Alfonso González González, Justo García-Sanz-Calcedo, and David Rodríguez Salgado. A quantitative analysis of final energy consumption in hospitals in spain. *Sustainable Cities and Society*, 36:169–175, 2018. (pag [1](#)).

- [43] M Grigioni, A Amodeo, C Daniele, G D’Avenio, R Formigari, and RM Di Donato. Particle image velocimetry analysis of the flow field in the total cavopulmonary connection. *Artificial organs*, 24(12):946–952, 2000. (pag 55).
- [44] Shamila Haddad, PAUL Osmond, and STEVE King. Metabolic rate estimation in the calculation of the pmv for children. In *47th International Conference of the Architectural Science Association*, pages 241–250. The Architectural Science Association Australia, 2013. (pag 62).
- [45] X He, S Karra, P Pakseresht, SV Apte, and S Elghobashi. Effect of heated-air blanket on the dispersion of squames in an operating room. *International journal for numerical methods in biomedical engineering*, 34(5):e2960, 2018. (pag 22).
- [46] Eirini Kardampiki, Emanuele Vignali, Dorela Haxhiademi, Duccio Federici, Edoardo Ferrante, Stefano Porziani, Andrea Chiappa, Corrado Groth, Margherita Cioffi, Marco Evangelos Biancolini, et al. The hemodynamic effect of modified blalock–taussig shunt morphologies: A computational analysis based on reduced order modeling. *Electronics*, 11(13):1930, 2022. (pag 86).
- [47] Kishor Khankari. Hospital operating room ventilation systems. *ASHRAE Journal*, 60(6):16–26, 2018. (pag 6).
- [48] Sihwan Lee, Beungyong Park, and Takashi Kurabuchi. Numerical evaluation of influence of door opening on interzonal air exchange. *Building and environment*, 102:230–242, 2016. (pag 8).
- [49] OM Lidwell, EJ Lowbury, W Whyte, R Blowers, SJ Stanley, and D Lowe. Effect of ultraclean air in operating rooms on deep sepsis in the joint after total hip or knee replacement: a randomised study. *Br Med J (Clin Res Ed)*, 285(6334):10–14, 1982. (pag 3).
- [50] Chunhua Liu, Guang Zhou, and Hongyuan Li. Analysis of thermal environment in a hospital operating room. *Procedia Engineering*, 121:735–742, 2015. (pag 48, 66, and 86).
- [51] Taishun Liu, Zeqin Liu, Ge Li, and Zhenjun Zuo. Comparative study of numerical simulation of indoor thermal environment in the pattern of personalized ventilation and stratum ventilation. *Procedia Engineering*, 121:785–791, 2015. (pag 84).
- [52] Zhijian Liu, Haiyang Liu, Rui Rong, and Guoqing Cao. Effect of a circulating nurse walking on airflow and bacteria-carrying particles in the operating room: An experimental and numerical study. *Building and Environment*, 186:107315, 2020. (pag 9 and 90).

- [53] Zhijian Liu, Haiyang Liu, Hang Yin, Rui Rong, Guoqing Cao, and Qihong Deng. Prevention of surgical site infection under different ventilation systems in operating room environment. *Frontiers of Environmental Science & Engineering*, 15(3):1–14, 2021. (pag [xi](#), [6](#), [7](#), and [14](#)).
- [54] Gearoid P Lydon, Derek B Ingham, and Monjur M Mourshed. Ultra clean ventilation system performance relating to airborne infections in operating theatres using cfd modelling. In *Building Simulation*, volume 7, pages 277–287. Springer, 2014. (pag [3](#)).
- [55] Nicola Massarotti, Alessandro Mauro, Salahudeen Mohamed, Andrzej J Nowak, and Domenico Sainas. Fluid dynamic and thermal comfort analysis in an actual operating room with unidirectional airflow system. In *Building Simulation*, volume 14, pages 1127–1146. Springer, 2021. (pag [6](#), [29](#), and [67](#)).
- [56] Sagnik Mazumdar, Stephane B Poussou, Chao-Hsin Lin, Sastry S Isukapalli, Michael W Plesniak, and Qingyan Chen. Impact of scaling and body movement on contaminant transport in airliner cabins. *Atmospheric Environment*, 45(33):6019–6028, 2011. (pag [8](#), [50](#), and [53](#)).
- [57] James McNeill, Jean Hertzberg, and Zhiqiang John Zhai. Experimental investigation of operating room air distribution in a full-scale laboratory chamber using particle image velocimetry and flow visualization. 2013. (pag [8](#)).
- [58] James S McNeill, Zhiqiang John Zhai, and Jean Hertzberg. Field measurements of thermal conditions during surgical procedures for the development of cfd boundary conditions. *ASHRAE Transactions*, 118(2), 2012. (pag [29](#) and [67](#)).
- [59] Farhad Memarzadeh and Zheng Jiang. Effect of operation room geometry and ventilation system parameter variations on the protection of the surgical site. In *Proceeding of IAQ*, 2004. (pag [6](#)).
- [60] K Nowak, K Nowak-Dzieszko, and A Marcinowski. Analysis of ventilation air exchange rate and indoor air quality in the office room using metabolically generated co2. In *IOP Conference Series: Materials Science and Engineering*, volume 415, page 012028. IOP Publishing, 2018. (pag [67](#)).
- [61] C Pasquarella, M Barchitta, D D’Alessandro, ML Cristina, I Mura, M Nobile, F Auxilia, and A Agodi. Heating, ventilation and air conditioning (hvac) system, microbial air contamination and surgical site infection in hip and knee arthroplasties: The gisio-siti ischia study. 2018. (pag [3](#)).

- [62] C Pasquarella, GE Sansebastiano, S Ferretti, E Saccani, M Fanti, U Moscato, G Giannetti, S Fornia, P Cortellini, P Vitali, et al. A mobile laminar airflow unit to reduce air bacterial contamination at surgical area in a conventionally ventilated operating theatre. *Journal of Hospital Infection*, 66(4):313–319, 2007. (pag 3).
- [63] C Pasquarella, P Vitali, E Saccani, P Manotti, C Bocconi, M Ugolotti, C Signorelli, F Mariotti, GE Sansebastiano, and R Albertini. Microbial air monitoring in operating theatres: experience at the university hospital of parma. *Journal of Hospital Infection*, 81(1):50–57, 2012. (pag 3).
- [64] Cesira Pasquarella, Antonella Agodi, Francesco Auxilia, Birgitta Lytsy, Ida Mura, Pierre Parneix, Walter Popp, and Silvio Brusafferro. Air quality in the operating theatre: a perspective. *Aerobiologia*, 36(1):113–117, 2020. (pag 2).
- [65] Cesira Pasquarella, Carla Balocco, Maria Eugenia Colucci, Elisa Saccani, Samuel Paroni, Lara Albertini, Pietro Vitali, and Roberto Albertini. The influence of surgical staff behavior on air quality in a conventionally ventilated operating theatre during a simulated arthroplasty: a case study at the university hospital of parma. *International journal of environmental research and public health*, 17(2):452, 2020. (pag 33 and 66).
- [66] Yang Peng, Ming Zhang, Fangqiang Yu, Jinglin Xu, and Shang Gao. Digital twin hospital buildings: an exemplary case study through continuous lifecycle integration. *Advances in Civil Engineering*, 2020, 2020. (pag 3).
- [67] Istituto Superiore per la Prevenzione E la Sicurezza del Lavoro. *ISPESL - Linee guida sugli standard di sicurezza e di igiene del lavoro nel reparto operatorio*, 2009. (pag 20).
- [68] Marcelo Pereira, Arlindo Tribess, Giorgio Buonanno, Luca Stabile, Mauro Scungio, and Ilaria Baffo. Particle and carbon dioxide concentration levels in a surgical room conditioned with a window/wall air-conditioning system. *International journal of environmental research and public health*, 17(4):1180, 2020. (pag 67).
- [69] Philip, Abouelmagd Maxemos, Hatem Abdelsamie, and Sadek. Review performance analysis of the ventilation system for the hospital operating room. *American Journal of Engineering Research*, 10(02):135–139, 2021. (pag 14).
- [70] Stephane B Poussou, Sagnik Mazumdar, Michael W Plesniak, Paul E Sojka, and Qingyan Chen. Flow and contaminant transport in an airliner cabin induced by a moving body: Model exper-

- iments and cfd predictions. *Atmospheric Environment*, 44(24):2830–2839, 2010. (pag 8 and 50).
- [71] Markus Raffel, Christian J. Kähler, Christian E. Willert, Steven T. Wereley, Fulvio Scarano, and Jürgen Kompenhans. *Particle Image Velocimetry: A Practical Guide*. Springer Science+Business Media, 3rd edition, 2018. (pag 55).
- [72] Adil Rasheed, Omer San, and Trond Kvamsdal. Digital twin: Values, challenges and enablers from a modeling perspective. *Ieee Access*, 8:21980–22012, 2020. (pag 2).
- [73] Francesco Romano, Luca Marocco, Jan Gustén, and Cesare M Joppolo. Numerical and experimental analysis of airborne particles control in an operating theater. *Building and Environment*, 89:369–379, 2015. (pag xi, xiv, 6, 8, 29, 32, 60, 65, and 67).
- [74] Francesco Romano, Samanta Milani, Roberto Ricci, and Cesare Maria Joppolo. Operating theatre ventilation systems and their performance in contamination control: “at rest” and “in operation” particle and microbial measurements made in an italian large and multi-year inspection campaign. *International Journal of Environmental Research and Public Health*, 17(19):7275, 2020. (pag 6 and 14).
- [75] Parastoo Sadeghian, Cong Wang, Christophe Duwig, and Sasan Sadrizadeh. Impact of surgical lamp design on the risk of surgical site infections in operating rooms with mixing and unidirectional airflow ventilation: A numerical study. *Journal of Building Engineering*, 31:101423, 2020. (pag xi and 18).
- [76] Sasan Sadrizadeh. *Design of Hospital Operating Room Ventilation using Computational Fluid Dynamics*. PhD thesis, KTH Royal Institute of Technology, 2016. (pag 9).
- [77] Sasan Sadrizadeh, Amar Aganovic, Anna Bogdan, Cong Wang, Alireza Afshari, Anne Hartmann, Cristiana Croitoru, Amirul Khan, Martin Kriegel, Merethe Lind, et al. A systematic review of operating room ventilation. *Journal of Building Engineering*, 40:102693, 2021. (pag xi, xix(2)b, 14(2)b, 15, 16, and 18).
- [78] Sasan Sadrizadeh and Sture Holmberg. Effect of a portable ultra-clean exponential airflow unit on the particle distribution in an operating room. *Particuology*, 18:170–178, 2015. (pag xi, 14, 16, and 17).
- [79] Gonzalo Sánchez-Barroso and Justo García Sanz-Calcedo. Evaluation of hvac design parameters in high-performance hospital

- operating theatres. *Sustainability*, 11(5):1493, 2019. (pag 1, 6, 41, 44, and 46).
- [80] Eric B Smith, Ibrahim J Raphael, Mitchell G Maltenfort, Sittisak Honsawek, Kyle Dolan, and Elizabeth A Younkins. The effect of laminar air flow and door openings on operating room contamination. *The Journal of arthroplasty*, 28(9):1482–1485, 2013. (pag 14).
- [81] Julian W Tang, Andre Nicolle, Jovan Pantelic, Christian A Klettner, Ruikun Su, Petri Kalliomaki, Pekka Saarinen, Hannu Koskela, Kari Reijula, Panu Mustakallio, et al. Different types of door-opening motions as contributing factors to containment failures in hospital isolation rooms. *PloS one*, 8(6):e66663, 2013. (pag 8 and 50).
- [82] Fei Tao, Bin Xiao, Qinglin Qi, Jiangfeng Cheng, and Ping Ji. Digital twin modeling. *Journal of Manufacturing Systems*, 64:372–389, 2022. (pag 3).
- [83] TL Thatcher, DJ Wilson, EE Wood, MJ Craig, and RG Sextro. Pollutant dispersion in a large indoor space: Part 1—scaled experiments using a water-filled model with occupants and furniture. *Indoor Air*, 14(4):258–271, 2004. (pag 8 and 50).
- [84] Wei Tian, Thomas Alonso Sevilla, Wangda Zuo, and Michael D Sohn. Coupling fast fluid dynamics and multizone airflow models in modelica buildings library to simulate the dynamics of hvac systems. *Building and Environment*, 122:269–286, 2017. (pag 7).
- [85] Albertus Anuello Louis Roberto Traversari. Aerogenic contamination control in operating theatres: studies towards effective use of udf systems. 2019. (pag 14 and 16).
- [86] W Uyttenhove, M De Paepe, and A Janssens. Cfd-modelling of temperature and humidity distribution in the st. pieter’s church. *IAE-Annex 41, Subtask, 1*, 2004. (pag 6 and 84).
- [87] Eric VanDerHorn and Sankaran Mahadevan. Digital twin: Generalization, characterization and implementation. *Decision Support Systems*, 145:113524, 2021. (pag 3).
- [88] JM Villafruela, Inés Olmedo, M Ruiz De Adana, C Méndez, and Peter V Nielsen. Cfd analysis of the human exhalation flow using different boundary conditions and ventilation strategies. *Building and Environment*, 62:191–200, 2013. (pag 67).
- [89] Fujen Wang, Indra Permana, Dibakar Rakshit, and Bowo Yuli Prasetyo. Investigation of airflow distribution and contamination

- control with different schemes in an operating room. *Atmosphere*, 12(12):1639, 2021. (pag 9).
- [90] Julien Weiss. A tutorial on the proper orthogonal decomposition. In *AIAA Aviation 2019 Forum*, page 3333, 2019. (pag 7 and 27).
- [91] William Whyte, D Vesley, and R Hodgson. Bacterial dispersion in relation to operating room clothing. *Epidemiology & Infection*, 76(3):367–378, 1976. (pag 3).
- [92] Yan-Lin Wu, Yu-Lieh Wu, and Azka Hasya Hanifan. Study on ventilation performance in operating room with variation ventilation design. In *Journal of Physics: Conference Series*, volume 1500, page 012040. IOP Publishing, 2020. (pag 6).
- [93] Chao-Tung Yang, Chi-Jui Liao, Jung-Chun Liu, Walter Den, Ying-Chyi Chou, and Jaw-Ji Tsai. Construction and application of an intelligent air quality monitoring system for healthcare environment. *Journal of medical systems*, 38(2):1–10, 2014. (pag 89).
- [94] Zhiqiang John Zhai and Anna L Osborne. Simulation-based feasibility study of improved air conditioning systems for hospital operating room. *Frontiers of Architectural Research*, 2(4):468–475, 2013. (pag xi and 6(2)b ).
- [95] Bin Zhou, Lili Ding, Fei Li, Ke Xue, Peter V Nielsen, and Yang Xu. Influence of opening and closing process of sliding door on interface airflow characteristic in operating room. *Building and Environment*, 144:459–473, 2018. (pag 14).
- [96] Wangda Zuo, Michael Wetter, Wei Tian, Dan Li, Mingang Jin, and Qingyan Chen. Coupling indoor airflow, hvac, control and building envelope heat transfer in the modelica buildings library. *Journal of Building Performance Simulation*, 9(4):366–381, 2016. (pag 7 and 33).
- [97] Zhenjun Zuo. Buildings Examples Tutorial Boiler. [https://simulationresearch.lbl.gov/modelica/releases/v5.0.0/help/Buildings\\_Examples\\_Tutorial\\_Boiler.html](https://simulationresearch.lbl.gov/modelica/releases/v5.0.0/help/Buildings_Examples_Tutorial_Boiler.html), 2021. [Online; accessed June 08, 2021]. (pag xi and 8).

#### COLOPHON

This document was typeset using the typographical look-and-feel classicthesis developed by André Miede. The style was inspired by Robert Bringhurst's seminal book on typography "*The Elements of Typographic Style*". classicthesis is available for both  $\text{\LaTeX}$  and  $\text{\LyX}$ :

<http://code.google.com/p/classicthesis/>

Happy users of classicthesis usually send a real postcard to the author, a collection of postcards received so far is featured here:

<http://postcards.miede.de/>

*Final Version* as of April 19, 2023 (version 1.0).

